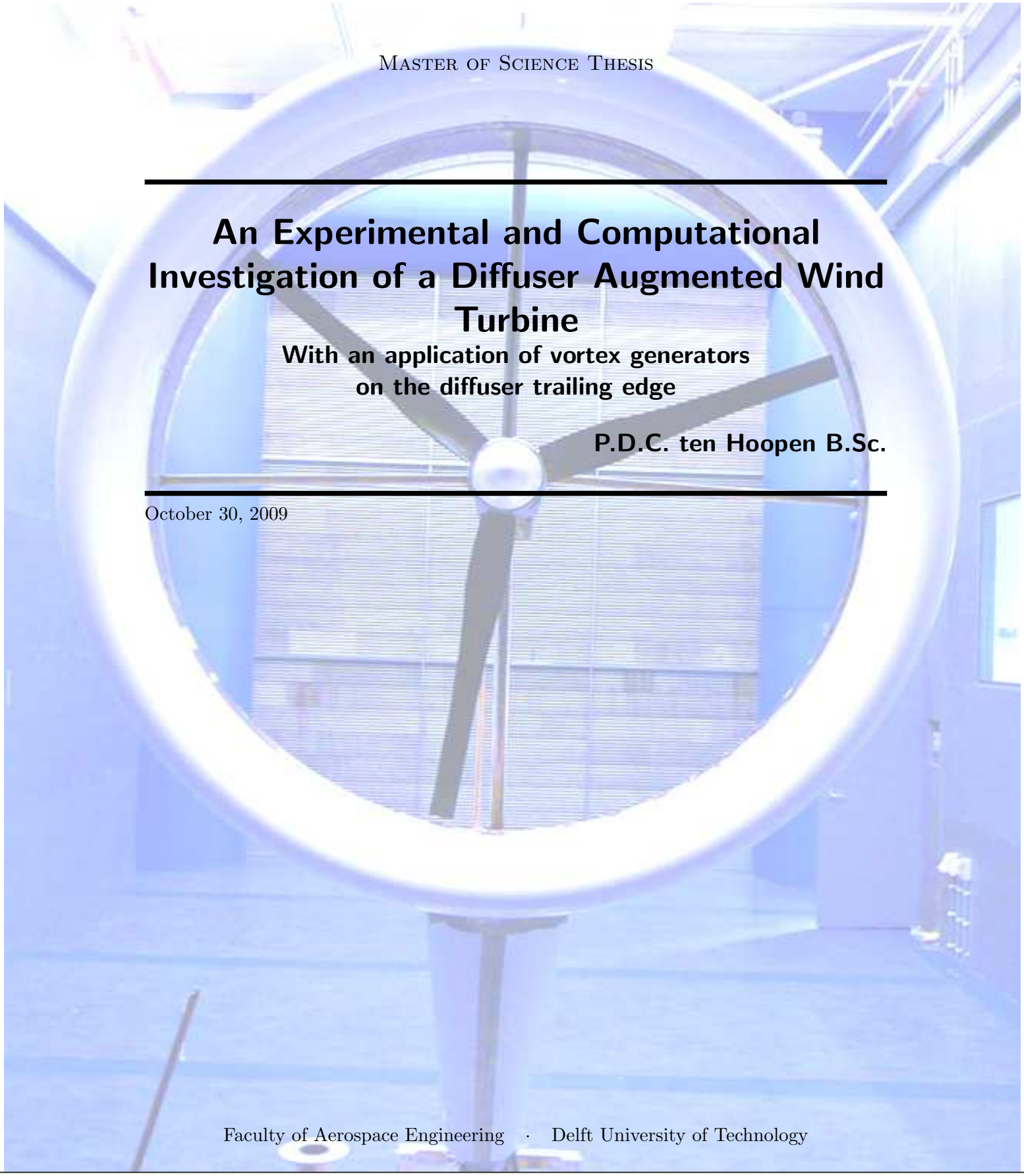

Master of Science Thesis

An Experimental and Computational Investigation of a Diffuser Augmented Wind Turbine

With an application of vortex generators on the diffuser trailing edge

P.D.C. ten Hoopen B.Sc.

October 30, 2009

Faculty of Aerospace Engineering · Delft University of Technology

TU Delft

The cover picture is taken from inside the wind tunnel nozzle of the *Open Jet Facility* at Delft University of Technology.

An Experimental and Computational Investigation of a Diffuser Augmented Wind Turbine

With an application of vortex generators on the diffuser trailing edge

Master of Science Thesis

For obtaining the degree of Master of Science in Aerospace Engineering at Delft University of Technology

P.D.C. ten Hoopen B.Sc.

October 30, 2009

Faculty of Aerospace Engineering · Delft University of Technology

Delft University of Technology

Delft University Of Technology
Department Of
Wind Energy

The undersigned hereby certify that they have read and recommend to the Faculty of Aerospace Engineering for acceptance a thesis entitled **"An Experimental and Computational Investigation of a Diffuser Augmented Wind Turbine"** by **P.D.C. ten Hoopen B.Sc.** in partial fulfillment of the requirements for the degree of **Master of Science**.

Dated: October 30, 2009

Head of department: _____
prof.dr. G.J.W. van Bussel

Supervisor: _____
ir. K. van der Heiden

Reader: _____
ir. W.A. Timmer

Reader: _____
dr.ir. C.J. Simão Ferreira

Reader: _____
ir. K.M.J. de Cock

Abstract

The Diffuser Augmented Wind Turbine (DAWT) has been studied periodically over the last five decades. It has already been established by the scientific community that the DAWT is superior to conventional bare wind turbines. In spite of this, the DAWT has not gained popularity worldwide due to high manufacturing cost of the diffuser. There are two possibilities to make a DAWT more lucrative; lowering the manufacturing cost or increasing the performance.

The present thesis is concerned with the second approach and considers the hypothesis that the generating power of a DAWT can be increased by turbulent mixing of the wake and free stream flow. This mechanism should decrease the diffuser's exit pressure and consequently increase the mass flow and power. In the present investigation this turbulent mixing is established by placing vortex generators on the diffuser trailing edge.

The hypothesis was tested through a series of full scale wind tunnel experiments. The experiments were conducted in the open jet facility of Delft University of Technology in collaboration with Donqi Urban Windmills. It was found that the application of vortex generators on the diffuser trailing edge lead to an increase in power of 9%.

Furthermore, in the pursuit of a better understanding of the flow behavior, an inviscid singularity model was formulated. The model uses a surface vorticity technique to simulate the behavior of the diffuser, supplemented with a lifting line approach to model the rotor. It was found that the inviscid model did capture the behavior of the DAWT reasonably well, although when compared to the measurement results it was observed to be overly optimistic.

Acknowledgements

Firstly, I would like to thank my supervisor, and CTO of Donqi Urban Windmills, Kasper van der Heiden. Without his support, knowledge and enthusiasm all of the presented experimental research would not have been possible. Also, I like to thank my professor, Gerard van Bussel, for his wisdom and for bringing me in contact with Donqi Urban Windmills.

Furthermore, numerous people where involved at different stages of my research work whom I like to thank. To start, Nando Timmer for his guidance during the preparation of the wind tunnel experiments; Hans Weerheim and Andries de Bue of *DEWEtron* for their assistance with the load cells; and all my colleagues at the section wind energy for their help and company.

Last, but certainly not least, I would like to thank my family and friends for their unbiased support during the years I've been studying at Delft University of Technology.

Delft, The Netherlands
October 30, 2009

P.D.C. ten Hoopen B.Sc.

Contents

List of Figures

List of Tables

Nomenclature

Latin Symbols

$A_{diff.exit}$	Surface of diffuser exit plane
$A_{proj.}$	Projected area perpendicular to the free stream flow
C_a	Axial force coefficient diffuser
$C_{a_{bare}}$	Axial force coefficient bare diffuser
c_{diff}	Chord diffuser
$C_{f,p}$	Friction coefficient on diffuser pressure side
$C_{f,s}$	Friction coefficient on diffuser suction side
C_n	Normal force coefficient diffuser
C_p	Pressure coefficient
c_{p_s}	Static pressure coefficient
$C_{p,s}$	Pressure coefficient on diffuser pressure side
$C_{p,p}$	Pressure coefficient on diffuser pressure side
c_{p_t}	Total pressure coefficient
C_T	Total thrust coefficient
D	Rotor diameter
F_A	Pressure drag on diffuser
F_r	Axial force on rotor
F_t	Total axial force on DAWT system
$F_{t_{NR}}$	Total axial force on DAWT system;No Rotor
h	Perpendicular distance between the vortex element and evaluation point
hs_n	Blade element horseshoe vortex element n

h_w	Helical pitch
K	Influence matrix
K_v	Vortex core correction coefficient
$\dot{m}_{ann.}$	Summed annular mass flow
$\dot{m}_{ave.}$	Total average mass flow
P	Static pressure
P_{gen}	Power of DAWT minus inverter and generator losses
P_∞	Freestream static pressure
r	Augmentation factor
r_{btc}	Blade tip clearance
r_c	Vortex core radius (0.0001)
$r_{diffexit}$	Diffuser exit plane raidus
r_{ld}	Local diffuser radius
r_{p_n}	Blade collocation point n
$r_{T_{tip}}$	Blade tip radius
$V_{ave.}$	Normalized total average velocity
$Va_{ave.}$	Normalized average axial velocity
V_W	Wake propagtion velocity
$Xpos$	Axial position of rotor plane

Greek Symbols

α	Angle of attack
$\alpha_{r_{p_i}}$	Angle of attack at blade collocation point$i$
β	Slip angle
Γ	Blade bound vorticity
γ	Vorticity strength
ϵ	Relaxation factor
θ_p	Pitch angle
θ_t	Twist angle
λ	Tip speed ratio
μ	Friction coefficient
ρ	Density
τ	Thrust ratio $\frac{F_r}{F_t}$
Ω	Rotor rotational speed

Subscripts

$_{C.Body.-Diff.}$	Influence of diffuser on centerbody
$_{c.body}$	Centerbody
$_{diff.R}$	Diffuser influence in rotor plane
$_{Diff.-C.Body}$	Influence of centerbody on diffuser
$_{diff.}$	Diffuser
$_{ind.wake}$	Induced wake
$_{rot.}$	Rotation blade

Abbreviations

DAWT	Diffuser Augmented Wind Turbine
NLR	Nationaal Lucht- en Ruimtevaartlaboratorium (National Aerospace Laboratory)
OJF	Open Jet Facility TUDelft
V-C	Vorticity code
VG	Vortex generator
VKI	Von Karmann Institute Brussels

Chapter 1

Introduction

Figure 1.1: The DonQi Urban Windmill

The concept of a Diffuser Augmented Wind Turbine, or DAWT for short, has been considered periodically over the past decades. Various attempts have been made to turn the DAWT concept into a commercial competitive product, but without any success. The reason for this is mostly because the breakeven point of a DAWT system, as compared to a conventional wind turbine, was not yet reached due to high manufacturing costs of the diffuser. However, a renewed incentive, due to a European treaty signed in 2007 in which it is agreed on to have reduced carbon emissions by 20[1] *% in 2020, has triggered governments to invest more in renewable energy projects and initiatives to cope with the ever increasing demand for energy. Donqi Urban Windmills is one of these 'green' initiatives stimulated by the Dutch government. The company has successfully developed a Diffuser Augmented Wind Turbine for the build environment that is also commercially competitive with various renewable energy sources like solar cells or small conventional wind turbines.*

The investigation of this thesis is concerned with the question of whether it is possible to increase the power output of a diffuser augmented wind turbine by means of promoting turbulent mixing of the wake and free stream flow. The research work presented in this

[1]The treaty was signed by the 27 European countries on februari the 21^{st} 2007. The percentage is relative to the carbon di-oxide emissions of 1990

thesis is exploratory in nature and was performed in collaboration with Donqi Urban Windmills. The work is divided into 8 chapters:

- **Chapter I :** The remainder of the present chapter in which the background and scope of the present thesis is elaborated in a bit more detail.
- **Chapter II :**A Short description of the basic DAWT physics is presented, followed by a short historical background on the DAWT development.
- **Chapter III :**A short assessment of DAWT applicable air mixing devices.
- **Chapter IV :**This chapter is concerned with an attempt to formulate a mathematical model based on potential flow theory to approximate the flow behavior in and around a DAWT.
- **Chapter V :** A detailed account of the test set up and procedures of the wind tunnel experiments
- **Chapter VI :** The presentation and analysis of the experimental results
- **Chapter VII :**Verfication and validation of the mathematical model with Xfoil, CFD and the obtained test results.
- **Chapter VIII :**Conclusions and recommendations

1.1 Background of present thesis

DonQi Quandary Innovations is a young company based in the Netherlands with the goal to become a prominent player in the supply of reliable decentralized, sustainable energy solutions and technologies. One of the energy technologies recently taken into production is the DonQi Urban Windmill. This DAWT has been developed in collaboration with the Dutch National Aerospace Laboratory (NLR) and Delft University of Technology (TUDelft). Although the design of the DAWT proves to be a commercial success, it is desirable to keep innovating to stay ahead of competition. There is no need to say that the research topic of the present thesis fits well in this line of philosophy.

1.2 Scope of present thesis

As stated earlier, the investigation presented in this thesis is to assess the augmentation effects of placing vortex generators on the DAWT's trailing edge. The hypothesis is that by turbulent mixing of wake and free stream flow, it should be possible to transfer momentum from the free stream flow to the rotor wake. This momentum transfer should decrease the diffuser's exit pressure and thus increase the mass flow and consequently the power.

The core of the present research work consists of an experimental approach and a computational approach. The motivation behind the experimental work is evident; to gain

more insight in the DAWT flow behavior, to assess the augmentation potential of a vortex generator equipped DAWT and to validate the mathematical model developed in the computational approach. Ideally, the experiments should be performed in a fully controlled environment. Taking this requirement into account, it is obvious that an open wind tunnel, like the OJF at Delft University of Technology, is the most suitable option. But that still leaves the question on what to measure. Since the flow structure behind the rotor is already a complex one, it was obvious that the influence of the vortex generators on that flow structure would be very difficult and tedious to assess. Taking into account the desire to keep things simple, it was decided to perform pressure measurements on the diffuser wall, behind the rotor and diffuser exit plane. It was furthermore desirable to measure the forces on the rotor and diffuser in order to assess how the rotor and diffuser force changed under the influence of the vortex generators. These force and pressure measurements were compared with one another and coupled to the power output. This way it was possible to investigate the implications of the vortex generators on the diffuser's trailing edge with a limited amount of data regarding the flow structure in and around the DAWT. With the help of DonQi, who also provided a full scale DonQi Urban Windmill, it was possible to build a test platform with these features.

The computational approach is meant as an aid to explain the observed measurement results. Even though the diffuser and blade geometries have been designed and optimized with the help of sophisticated Computional Fluid Dynamics (CFD) software, it was found in previous wind tunnel experiments, performed at von Karman Institute [51], that the CFD calculations performed by NLR did in fact over estimate the flow behavior inside the diffuser [42]. Apart from the fact that CFD calculations take a tremendous amount of time and computational resources, it was noted by several researchers and experts that CFD is not the tool of choice in the present investigation. It was argued, that it is highly questionable whether the present CFD turbulence models would be of any value when trying to capture the turbulent flow mixing of the wake with the vortices emanating from the vortex generators. Taking these recommendations into account, it was decided to take a more crude approach; the method of singularities as presented in chapter 4.

Chapter 2

A Short DAWT Review

The following chapter will shed some insight on the operation principles and developments of a DAWT. The first section provides some physical background on a DAWT. The second section concisely reviews the main DAWT development stages up till now.

2.1 Basic DAWT physics

Two basic power augmentation principles for wind turbines have been indicated in the past. The first principle is to increase the mass flow through the wind turbine. The second principle is to promote turbulent mixing of the wake behind the rotor [8][53][21]. Although the triggering mechanism of the second principle is different, it has to be stressed that the ultimate effect is also an enhanced mass flow. The first principle is best explained with the analogy of figure 2.1.

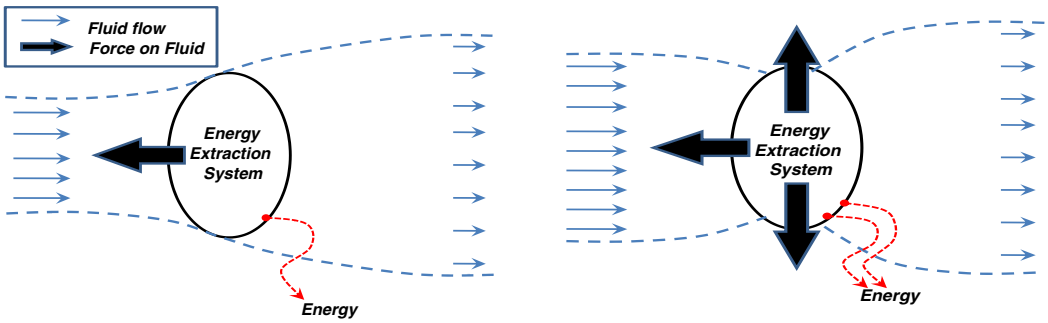

(a) Conventional wind energy extraction scheme [53]

(b) Diffuser augmentated wind energy extraction scheme [53]

Figure 2.1: Wind energy extraction schemes

Theoretically, when a bare rotor is operating at the maximum Betz limit, it is found from the momentum theory that the air flow is decelerated to $\frac{2}{3}$ of the free stream velocity

when it arrives at the rotor plane. This flow deceleration causes a pressure increase (see figure 2.2) in front of the rotor that effectively causes a fraction of the mass flow being pushed sideways around the rotor, as illustrated in figure 2.1a. A direct consequence of the flow continuity and incompressibility condition is that the rotor effectively captures the kinetic energy contained in the wind from an effective surface that is $\frac{2}{3}$ of the swept rotor surface. Figure 2.2 shows the axial pressure and velocity variation over an ideal wind turbine rotor as obtained from Betz's momentum theory.

A mechanism to increase this effective surface is by exerting a force perpendicular to the oncoming wind [53] [39]. This perpendicular force on the flow can be realized by placing an annular lifting device around the rotor with it's suction side pointing towards the center. This annular lifting device can be a shroud/duct, diffuser of annular wing. From the third law of Newton it is known that the oncoming air stream will try to exert a counteracting force, as shown in figure 2.1b, in order to establish a force equilibrium. This counter acting force can only be exerted by the flow if more air mass is *squeezed or sucked* through the annular lifting device. So in effect, this outward force will widen the stream tube, or catchment area, ahead of the rotor as depicted in figure 2.3 and 2.1b.

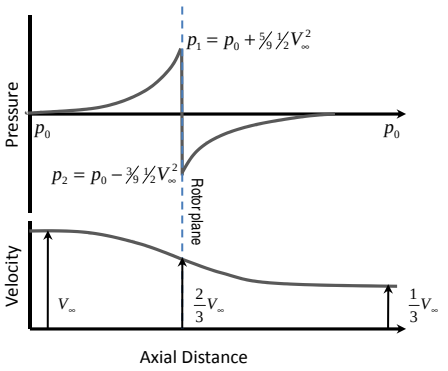

Figure 2.2: Ideal axial pressure and velocity variation over a bare wind turbine rotor

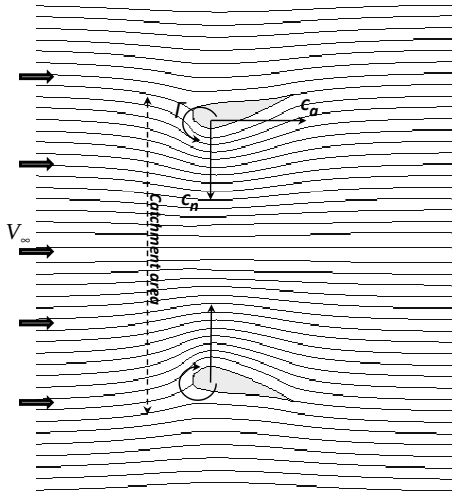

Figure 2.3: Ideal diffuser flow pattern

The DAWT under consideration employs an annular wing placed under an angle of attack which causes the annular wing to also behave as a diffuser. Figure 1.1 shows a picture of the present DAWT developed by DonQi. The DAWT of Donqi is also equipped with a 40 mm high Gurney flap on the trailing edge of the diffuser. The Gurney flap is in fact a spoiler and has it origins in the automotive industry. Various investigators have applied this concept to enhance the power output of a DAWT and experimental results indicated a better performance [22] [17]. The Gurney flap enhances the bound vorticity of the airfoil and causes the exit plane velocities close to the trailing edge to increase. The increase in diffuser exit plane velocities is in turn accompanied by a reduced static exit pressure and consequently an enhanced massflow. As noted earlier, this increased mass flow leads to a higher extractable energy potential.

The principle of bound vorticity has also been proposed to explain the physics behind a DAWT. An annular airfoil, with its suction side pointed towards the center, causes the

air flow on the inside to accelerate. The suction is related to the lift of the airfoil and this is again, according to the Kutta Joukowski theorem, related to the bound vorticity. This reasoning becomes clear if one has a look at figure 2.3. The annular airfoil, generates an inward radial lift force. This lift force is accompanied by a ring vortex which by the Biot-Savart law will induce a higher velocity on the suction side. In effect, this higher velocity increases the mass flow through the rotor plane. As noted by various scientists like Lewis [1] *et al.* and Hansen[39]; the bound vorticity increases the catchment area in front of the rotor and consequently the *"swallowing"* capacity of the complete system.

The second power enhancement principle makes use of mixing effects. As already mentioned, when a rotor extracts energy from an air flow it will cause, like every other obstacle in a flow, a wake. The wake behind the rotor has a pressure and a velocity deficit as compared to the undisturbed free stream flow. A low pressure behind the rotor is favorable but a low wake velocity is not. As noted by van Bussel [53] and Igra [26], the power augmentation of a DAWT is a direct consequence of the sub-atmopsheric pressure around the rotor and exit plane of the shroud. Thus, ideally one wants to maintain a situation behind the rotor where the pressure is low and the mass flow still high. The high mass flow can be established by wake expansion [21][18][43], which is in fact already the case with a normal operating wind turbine, or by an increase in wake velocity. The reasoning of the mixing principle is to restore this momentum deficit behind the rotor by mixing the wake flow with the undisturbed free stream flow. The undisturbed free stream flow will in turn provide the extra momentum for the "exhausted" rotor wake flow to recover from the velocity deficit caused by the energy extraction of the rotor. Another reasoning is that the mixing causes the wake to have an additional expansion and thus providing the rotor wake flow with more volume. More wake volume for the same mass flow through the diffuser will result in lower exit pressures behind the rotor and therefore more suction. For normal wind turbines this mixing effect is rather small due to the tip vortices emanating from the blade tips. As noted by van Bussel [53], these tip vortices *"effectively act like roller bearings, preventing the outer flow from mixing with the wake flow"*. But another advantage of the DAWT configuration is that the tip vortices created at the blade tips are expected to be significantly less due to the close proximity of the diffuser wall[26][18]. Therefore, the mixing potential behind the exit plane of a DAWT is expected to be higher than for a normal wind turbine.

2.2 A concise historical DAWT development review

Betz himself acknowledged the potential of a ducted/diffuser augmented wind turbine in 1929 [2]. He was also the first to formulate a DAWT theory in which he assumed the static pressure at the DAWT's exit plane to be equal to the ambient pressure. Another restriction imposed by his theory was that the exit to throat area ratio had to be small, thus leading to small disk velocity ratios. From these conclusions the idea of ducted wind turbines was abandoned till the 1950's when the Japanese researcher Sanuki [40], published some experimental results of a shrouded wind turbine indicating a gain in power output up to 88% relative to the Betz limit. This publication was followed by Iwasaki [38] in 1953 who found a 30% increase of power by placing the rotor in a cylindrical duct of constant radius. Around the same time, the British researchers Lilley and Rainbird [18]

where working on some theoretical studies on ducted windmills which they publicized in 1956. In this work Lilley and Rainbird reasoned that the increase in axial velocity and a reduction of blade tip losses would be the major contributors to additional power augmentation from a duct. In their parametric analysis they identified two critical design parameters; the diffuser exit pressure and the inlet contraction ratio. These two parameters were in turn a function of internal frictional losses, diffuser exit area ratio and the external shape of the duct. They also suggested that a flow augmentator, like a flap, at the diffuser exit plane could further raise the power augmentation due to a decreased sub atmospheric exit pressure. Finally, as reported by Phillips [45], Lilley and Rainbird considered the cost of ducted windmill energy devices and concluded that a streamlined duct with an inlet area ratio of no more than 1.5 and an exit area ratio[1] of 3.5 should be the most suitable geometry with a gain in power output of at least 65% relative to the output of a bare turbine with the same rotor diameter [45]. A few years later, at the end of the 1950^{ties},an Isreali researchers team led by Kogan *et al.* [50] [49], performed a proof of concept study for shrouded aerogenerators at the Ben Gurion university in Israel where they tested 3 different shrouded windturbine configurations as depicted in figure 2.4a [50].

Kogan *et al.* showed that the design did show huge power augmentation factors of about 3.5. However, the size of the duct made it a commercially uncompetitive design. Due to the nature of the air flow through the diffuser, the diffuser could not be shortened while maintaining the exit-area ratio and the corresponding low exit pressures. It was shown that diffuser apex angles beyond 9° caused serious flow separation inside the diffuser.

The problem of flow separation with increasing diffuser apex angles could be delayed by the employment of ring shaped flaps at the diffuser exit plane (see figure 2.4b). It was reasoned that these airfoil shaped flaps could decrease the pressure and therefore help the flow to overcome the positive pressure gradients existing in the diffuser. This concept proved to be quite fruitful and diffuser exit pressure coefficients of $-0.5 < C_{p_e} < -.035$ where reported [26]. Hence, a shorter shroud with a considerable power augmentation was demonstrated. Kogan and Seginer's research work ceased in 1967.

Igra, a former student of professor Kogan who graduated on the turbine design of a DAWT, continued the research work on diffuser augmented wind turbines at the Ben Gurion university in 1974. Igra [26] starts with the observation that the power augmentation of a shrouded rotor is a direct consequence of the sub-atmospheric pressure around the rotor and at the exit plane of the shroud. These sub-atmosperic pressures produce a "*suction*" and consequential a higher mass flow. From the theoretical and experimental work [24][23][25], Igra concludes that the exit pressure should be as low as possible and that the diffuser should have a high efficiency with an area ratio as big as possible. An interesting assumption made in Igra's analysis was that he assumed the rotor load to be independent of the pressure recovery and exit pressure of the shroud. It was also observed by Igra that the flow at the rear part of the shroud was not uniform over the entire cross section[2]. Two distinct regions where identified; an annular flow at the wall and a center core flow with a low total pressure. At the end of the 1970's Igra also constructed a pilot plant of 6 meters in diameter with a total length of 8 meters [27] (see figure 2.5a).

[1] The exit area ratio is the ratio of the diffuser exit plane area relative to the swept rotor area

[2] This non uniform flow was also found in the present investigation as shown in figure 6.10 and 6.9

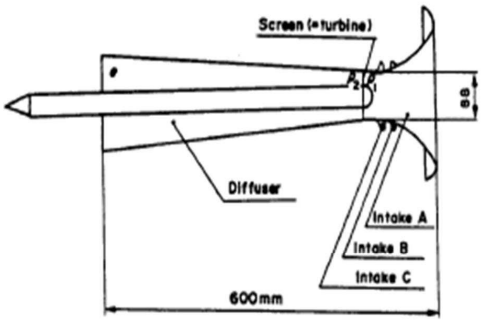

(a) Model A -geo tested by Kogan[50][26]

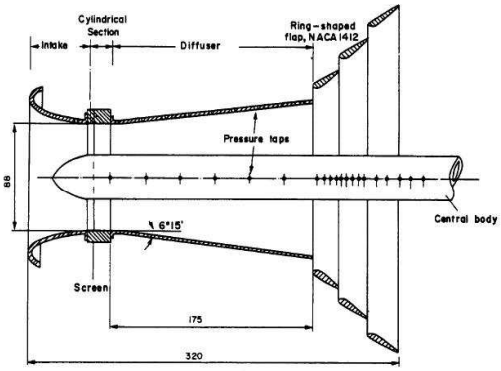

(b) Model A

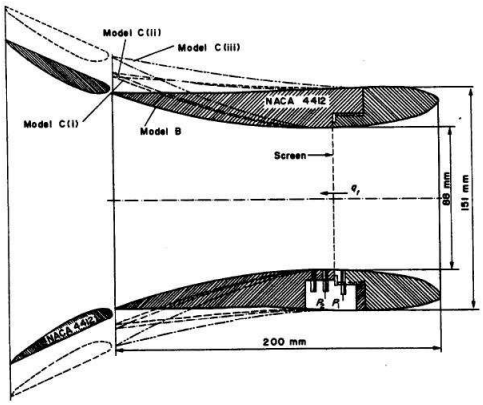

(c) Model A -short

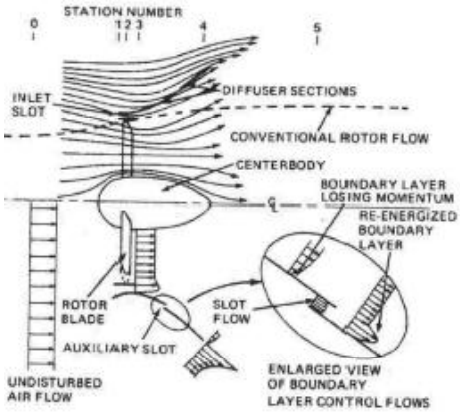

(d) A schemtic sketch of the slotted DAWT investigated at Grumman research

Figure 2.4: Some DAWT concepts tested in Israel, Ben Gurion University (figures *a*,*b* and *c*) and U.S.A, Grumman research (figure *d*)

At the same time, due to the oil crisis in 1974, Foremann *et al* at Grumman research in the United States of America [17] [16] started their own extensive research and development of DAWT's employing slots to control the boundary layer. Figure 2.4d shows a schematic sketch of the slotted diffuser operating principle. More than 100 different models where tested in the windtunnel. The models where initially, like in Igra's research equipped with a screen to simulate the pressure drop over the rotor. Later it was also confirmed by Foremann [17] that the swirling flow of an operating turbine actually delayed flow separation inside the diffuser due to a momentum transfer to the boundary layer. It was found by Foremann that augmentation factors of about 3 where possible with an area ratio of about 2.5-3 [16]. A few years later in 1977, Lewis *et al* [1] started some experimental and theoretical research in United Kingdom. Lewis *et al.* identified the

contraction ratio[3] at the entry and diffuser area ratio as the two prime geometrical design features. From a momentum formulation it was concluded that an shrouded wind turbine could extract 42.86 % more power than a conventional bare wind turbine. Like Igra and his predecessors, Lewis and Foremann addressed the importance of trying to reduce the size and cost of the diffuser.

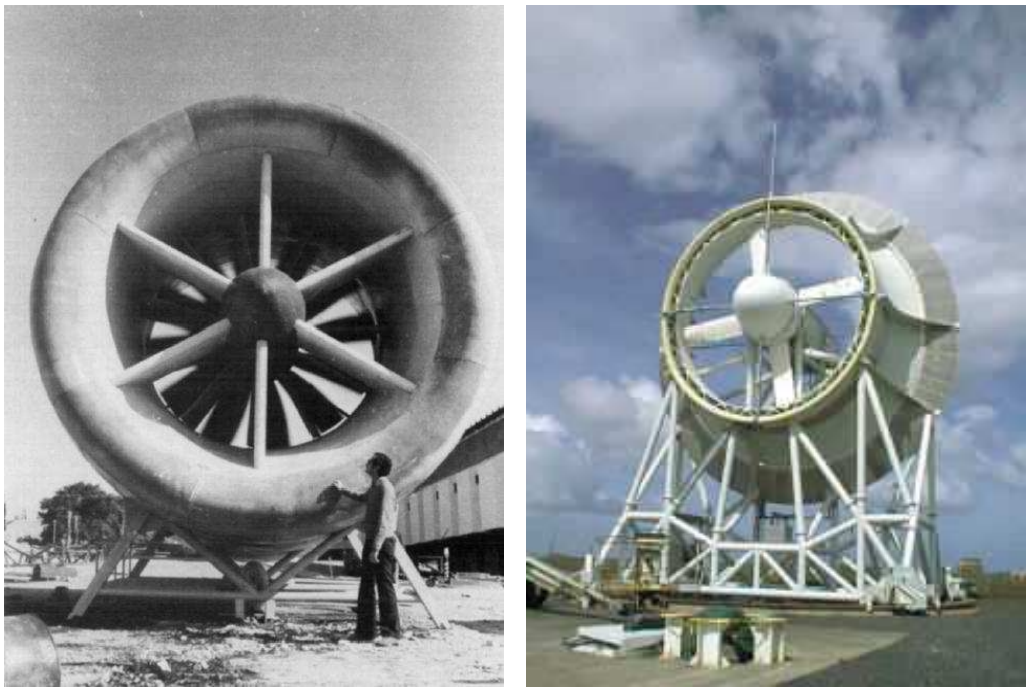

(a) The pilot plant DAWT of O.Igra ; the power generated is about 1 Kw at 5 m/s. [27]

(b) The Vortec DAWT in New Zealand [56]

Figure 2.5: Some full scale DAWT's

Due to the promising testing results of the DAWT systems presented by Igra and Foreman, renewed interest initiated at the end of the 70-ties a whole range of computional, theoretical and experimental DAWT investigations in Australia, U.S.A, Japan and Europe. Different maximum power coefficients where reported and different controlling mechanisms where proposed to explain the DAWT augmentation behavior. For example,in 1979, de Vries [5] tries to point out that the DAWT power augmentation is governed by the force the shroud exerts on the flow. From his analytical approach he finds the same relation as derived by Igra [24], albeit in a slightly different way, with a maximum power coefficient of 0.7698. Like Loeffler [32] [55][4], de Vries also proposed a model based on the method of singularities. In 1986 Dick [8] states that the DAWT mass concentration is completly governed by the radial force exerted by the shroud on the flow. He also illustrates through his analysis and experimental results of Igra and Foreman that the axial forces play an important role in the DAWT performance. He finally concludes that a maximum power coefficient of 0.83 should be attainable.

[3]The contraction ratio is defined as the ratio of catchment area,see figure 2.3 relative to the rotor swept area

[4]The theory presented in chapter 4 is loosly based on Loefler's approach

Although many researchers took the commercial considerations into account, no attempts where undertaken to turn the investigated DAWT concepts into commercial competitive products. But Finally, on May the 2^{nd} 1997 the new Zealand (Auckland) based company Vortec took it's 17 meter tall Diffuser Augmented Wind Turbine in operation. The multi million dollar prototype DAWT,as depicted in figure 2.5b, was based on Foremann's DAWT configuration and had a blade diameter of 7.3 meters with an expected power output of 1 MW. The DAWT design was optimized by Philips *et al.* [45] [6] with the use of CFD, in which the rotor was modeled as an actuator disk, and a serie of small scale experiments. Unfortunately, the data of the fullscale DAWT showed only an augmentation of 2.4 instead of the expected 9 [56]. The project turned out to be a fiasco and Vortec finally closed it's doors in 2001. Around the same time van Bussel [54][52] readdressed the DAWT theories developed so far and concluded with the help of a momentum formulation that optimal operation conditions of a DAWT are the same as for a bare wind turbine. Also, he concluded that the pressure drop over the wind turbine is independent of the diffuser area ratio. It is furthermore found that the thrust of the rotor and shroud are dependent on each other but that the thrust on the rotor unlike the diffuser is not proportional to the mass flow. Finally it is noted by van Bussel that rotor power coefficients of 2,5 could be possibly obtained with "*significant*" back pressure reductions. It can be concluded from van Bussel's work that the augmentation expectation of Vortec where unrealistically high. Never the less, the fiasco of Vortec did not discourage the DAWT research and continued in various countries. A few small companies like CITA in France, KBE and Enflo in Germany (see figure 2.6a and figure 2.6d), CATT in the U.K. and the Japanse company GH Craft (see figure2.6b) have tried to use the DAWT concept on a smaller scale without a big commercial succes sofar. But still, the research and development continues. To illustrate, a new momentum formulation has been proposed recently by Jamieson [29][30]. Like Fletcher in the 80's [12] [11], Jamieson tries to couple his momentum theory, based on a functional relations like Dick [8], directly to a DAWT BEM code which is implementated in the wind tubine design software package Bladed. Also, renewed interest in the DAWT configuration has re surfaced in the United States of America. Werle and Pretz [58][57] propose a momentum based formulation in which a duct thrust coeffient is defined that controls the behavior of a DAWT. Werle and Pretz are also affiliated to the in Massauchets-based company *Flodesign*, who claimed in 2008 to have developed a shrouded wind turbine generating 3 to 4 times more power than a conventional wind turbine (see figure 2.6c). The design is different in the sense that they employ a lobed slotted diffuser which should enhance mixing and thus the power output. In a recent publication they claimed to have exceeded the Betz limit [34][5]. In conclusion, over the last 6 decades the DAWT configuration has received its fair share of attention, but to the author's knowledge, no big commercial success has been achieved so far by any company. Also, no commercial DAWT design tools have been developed so far and it seems that the scientific community still have to agree on a thorough DAWT theory.

[5]These results where obtained in wind tunnel experiments. It has to be noted that nothing is stated about the wind tunnel type. In open wind tunnel experiments with the present DAWT performed at VKI [51], it was found that various blockage effects like solid,wake and wall blockage can significantly influence the performance.

[7]claimed rated power: 10 Kw with a diameter of 4.68 m

[8]claimed rated power: 0,5 Kw at 12,5 m/s with a rotor diameter of 0.71 m

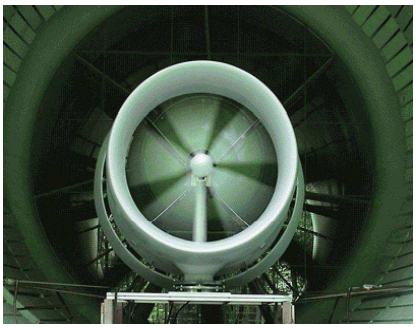

(a) A DAWT by German company KBE

(b) A DAWT by the japanese company GH Craft[7] [15]

(c) A DAWT concept by Flodesign U.S.A [13]

(d) A DAWT by German company Enflo[8] [9]

Figure 2.6: Some next generation DAWT designs

Chapter 3

Flow Mixing Principles

As discussed in the previous chapter, concept DAWT configurations like slotted or flapped diffusers have been proposed to enhance the power output of a DAWT. The reasoning behind the slotted diffuser of Foreman [17][16] and later of Vortec [45] did not so much put the emphasis on the mixing of outer and inner flow over the whole cross section of the diffuser, but more on re-energizing the boundary layer inside the diffuser. The re-energizing should prevent flow separation inside the diffuser. With this flow separation delay inside the diffuser, it is possible to increase the diffuser apex angle and thus decrease the overall static pressure behind the turbine. As explained, this low pressure causes a suction resulting in more mass flow. Igra also investigated wall suction and blowing to establish this effect [24].

Another way to promote mixing of the outer and inner flow can be established by introducing streamwise vortices. It has been recognized over the past decades that the introduction of streamwise vorticity between co-flowing streams is an efficient way to promote mixing [19]. The basic idea is to introduce a stream wise vortical structure with an associated cross-stream circulation. In the present chapter a short review is given of two possible streamwise vortical mixing configurations that can be applied on the diffuser's trailing edge.

3.1 Flow mixing with a lobed trailing edge

Stream wise vortices can be generated with a lobed mixer[1] or with vortex generators. The lobed mixing approach has recently been applied by FloDesign wind turbines where the lobed mixer geometry is applied at the trailing edge of the diffuser as depicted in figure 2.5b and 3.1a.

[1]There are two basic shapes of the lobed mixer; the "forced mixer" geometry as shown in figure 3.1a and the "convoluted plate" geometry where the lobes have a straight section towards the trailing edge instead of a diverging section as shown in figure 3.1a. The forced mixer geometry is the most efficient mixing configuration [19]

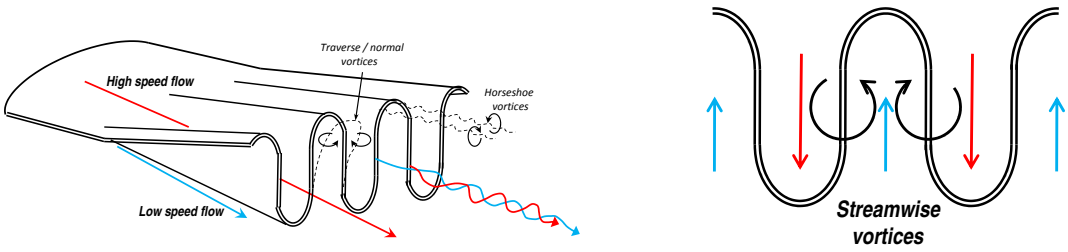

(a) Lobed mixer [19]

(b) Backview lobed mixer [19]

Figure 3.1: Vorticity creation at a lobed trailing edge

Because of the different stream wise velocities at the suction and pressureside of the diffuser, the incoming boundary layer vortex lines, initially normal to the flow, are skewed into the stream wise direction (see figure 3.1). The counter rotating pair of stream wise vortices have been identified as an important feature in the mixing enhancement of lobed mixers. Not only do they increase the interfacial surface area between the streams but also local flow property gradients which in turn promote the mixing. In the pursuit of a better understanding of the flow processes accompanying a lobed mixer, Werle [3] found that the large scale stream wise vortices undergo a three step process; formation, intensification and breakdown. Eckere also observed that the length required for the flow to reach the third step to be a function of the velocity ratio across the mixer[3]. Apart from the large scale streamwise vortices, the lobed mixer also induces small scale transverse vortices parallel to the trailing edge. Horseshoe vortices formed around the front of the lobes where found to be an order of magnitude smaller than either the streamwise or transverse vortices and have therefore little impact on the overall mixing process.

3.2 Flow mixing with vortex generators

The wind turbine under consideration however, does not apply a lobed mixer trailing edge geometry. Therefore, one has to find a different way to generate these stream wise vortices, generated preferable as in the lobed mixer case in counter rotating pairs. When these considerations are taken into account one immediately arrives at the application of vortex generators. Vortex generators are usually applied on aircraft wings, fuselages and nacelles in order to reduce the aerodynamic drag caused by flow separation, leading to a better overall operational performance. The general idea behind this application is simple; to create a vortex in a predictable manner which can re-energize the boundary layer flow.

The extra energy in the boundary layer, which is entrained from the surrounding free stream flow, manifests itself as an airflow momentum increase close to the bounding surface (see figure 3.2). This momentum increase encourages in turn the airflow to stay longer attached to the aircraft wing surface in different operating conditions, e.g. landing or take-off.

In the field of wind energy technology, the application of vortex generators are also in-

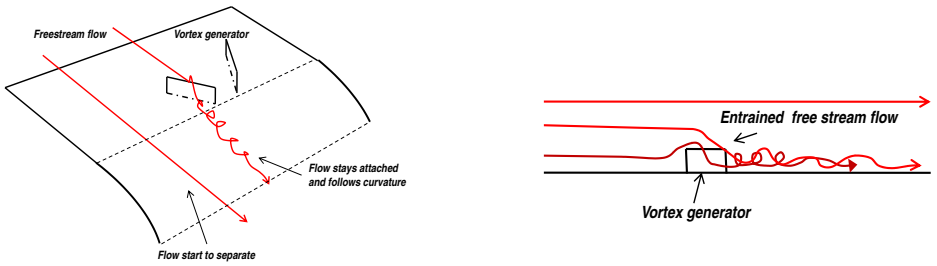

(a) Vortex generator flow over a curved surface

(b) Vortex generator flow

Figure 3.2: Schematic sketch of vortex generator flow

creasingly reconized as means to make the rotor blades more resistant to stall. Wind turbine blades are especially susceptible to stall at the root section due to the thick blade profile. By placing small vortex generator fins on the backside of the blade's root section, a thin current of turbulent air results in the flow being able to stay longer attached to the blade's surface and thus delaying stall. Another reason to apply vortex generators is to trim aeroelastic effects caused by the interaction of structural elastic deformations and fluctuating aerodynamic loads. Aeroelastic effects may have serious impact on the fatigue life of wind turbine blades and are therefore undesirable.

Although the application of vortex generators can significantly reduce the drag due to flow separation, they also cause drag themselves. So in order to assess the overall effect of a vortex generator in normal aviation and wind energy practices, one has to take the positive and negative effects into account. These positive and negative effects depend on the size and shape of the vortex generators and a whole range of vortex generators have been developed in aircraft industry, and to a lesser extent automotive and wind energy industry. The trend however, as outlined by Lin [36], is to design vortex generators which produce vortices that are just strong enough to get the job done, hence arriving at the low profile vortex generators.

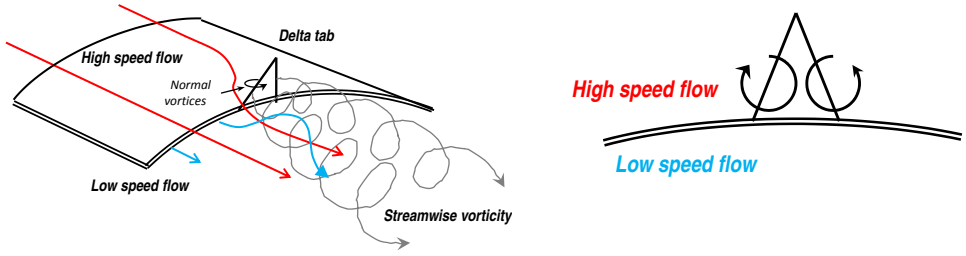

(a) Vortex generator/delta tabbed trailing egde

(b) Backview vortex generator/delta tab

Figure 3.3: Vorticity creation at a vortex generator /delta tab equipped trailing edge

For the present application however, a strong vortex is desirable and the vortex induced

drag is of no importance since the DAWT is fixed to the ground by a supporting pile[2]. A simple shape that does generate strong stream wise vortices is the delta wing shape as shown in figure 3.3. Yu *et al* [48] performed an experimental investigation in which a single inverted delta tab was attached to trailing edge, at an angle of 45 degrees pointing down stream, of a splitter plate in a two stream mixing layer. This configuration was found by Foss and Zaman in earlier research [14] to be the most effective way of promoting mixing with delta tabs. Detailed flow measurements where performed with a X-hotwire probe and various static pressure orifices in front of the delta tab. Analysis[3] showed that stream wise vortex formation and subsequent mixing effect were stronger and more intense when the tab was tilted into the high speed side. Yu *et al.*, who used a three component fiber optic laser-Doppler anemometer to investigate the flow, adopted the suggestion pioneered by earlier researchers [48][14] to explain the mechanism behind these stream wise vortices emanating from the tab. The first source is caused by the adverse pressure gradients formed upstream of the tab decelerating the stream and sub sequentially forming two counter rotating vortices as the flow tries to flow around the delta tab (see figure 3.3). A second source originates from the vorticity shed along the sides of the tab. Although an upward tilted tab forms stronger vorticity, Yu [48] noted from his experimental observations that a downward titled delta tab generates stream wise vorticity from the low speed side to high speed side. This could be a favorable effect if one tries to establish enhanced wake expansion behind the diffuser exit plane.

To conclude, it has to be stressed that the flow on top and below the splitter plate applied by Yu *et al.* where, apart from the flow velocities, uniform and identical without any swirl. The flow behind the rotor of the DAWT however does have swirl caused by the rotating blades. The flow mixing circumstances in the present investigation with those present at Yu's experiments are therefore not identical and mechanisms adopted by Yu and his predecessors to explain the flow behavior around a delta shaped vortex generator may not be completely applicable to the flow around the vortex generators on the diffuser's trailing edge. This issue is not investigated in the present thesis due to the lack of detailed flow measurements around the vortex generators. Only the ultimate effect of the vortex generators on the diffuser's trailing edge will be addressed in the present thesis.

[2]From a structural point of view the vortex induced drag could become an issue if the drag forces become a considerable percentage of the total drag force on the complete DAWT system

[3]Turbulent flow was found at the delta tab

Chapter 4

An Inviscid DAWT Flow Model

Only few researchers in the past have tried to analyze the flow field around a DAWT using the method of singularities. One of the first to tackle this problem was Loeffler [32] [55] who tried to approximate the flow around the wide angle compact slotted DAWT developed by Foreman et al. at Grumman research. The thin walled conical diffuser was represented by a series of ring vortices. In order to calculate the strength of the discrete ring vortices, Loeffler applied the Neuman boundary condition on the velocity normal to the duct's surface. In order to determine the radii and strength of the ring vortices representing the wake surface, an iterative scheme was applied in which the streamlines of the wake were traced out. Loeffler mainly used the theory to investigate observations made by Foreman [17] [16] regarding the diffuser dump flanges, inlet slots and DAWT performance. De Vries [5] proposed a similar approach although simplified by assuming a triangular vorticity distribution on the duct. In all these computional investigations the rotor was represented by ring vortices and vortex cylinders as described in the earlier work of Kuchemann and Weber [4].

The following computational scheme to calculate pressure and velocity distributions of a DAWT is a combination of methods developed for the analysis of marine and aeronautical propulsion systems, supplemented with a lifting line approach to analyze the rotor of the wind turbine. The big difference with the earlier work is that the diffuser is modeled as a lifting body with thickness instead of a flat plate. Furthermore, where Loeffler and de Vries applied a ring vortex to model the rotor, the present formulation applies a lifting line approach. In the first and second section one can find a detailed account on the mathematical formulation used to model the diffuser and rotor respectively. The last section is concerned with uniting the two seperate models in a coherent DAWT model.

4.1 The diffuser surface vorticity formulation

The foundation of the mathematical model describing the annular wing finds its origin in a publication of Martensen (1959). The method of Martensen, also reffered to as

'*the surface vorticity method*' makes use of an finite number of rectilinear vortices. The following section puts the vorticity model in a physical context as outlined by Lewis [35].

4.1.1 The physical significance of the surface vorticity formulation

When examining a real flow around an arbitrary body one can simplify matters by identifying a thin layer in the immediate vicinity of a bounding surface. In effect, this layer, also called the boundary layer, divides the fluid flow into a thin region close to the bounding surface where viscosity is dominant and a region outside this boundary layer where viscosity can be neglected. If it is assumed that the outer region flow is also irrotational, it is possible to model this flow region with potential flow theory. The dynamic behavior of this outer flow will then be the driving force for the creation of voriticity in the boundary layer flow where the creation of this vorticity on the surface is directly related to pressure gradient normal to the surface. The vorticity created in this boundary layer will in turn reduce the velocity V_s just outside the boundary layer flow to zero on the body surface.

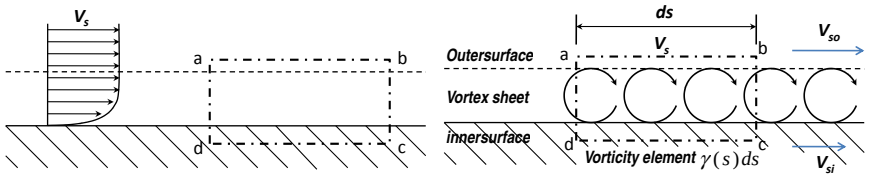

(a) Boundary Layer [35] (b) Vortex equivalent [35]

Figure 4.1: Boundary layer and surface vorticity equivalent

Also, under the action of viscosity the vorticity diffuses normal to surface resulting in a flow pattern depicted in figure 4.1a. If viscosity approaches zero and the Reynolds number approaches infinity, the viscous diffusion normal to the surface would also reduce and consequently the boundary layer would become infinitely thin. In effect, the boundary layer can thus be represented by an infinitely thin vorticity sheet with a velocity discontinuity across it. The velocity distribution on the surface can be found by enclosing a surface vorticity segment with a progressively decreasing contour. Figure 4.1b shows this contour around a vorticity segment where *ab* and *cd* are parallel to the streamlines and *da* and *bc* are normal to them. The total circulation of the vorticity segment around *abcd* can be expressed as: $(v_{so} - v_{si})ds = \gamma(s)ds$ where v_{so} and v_{si} are the fluid velocities parallel to the surface just outside and inside the vortex sheet. Under the influence of the viscous forces in the boundary layer, the necessary zero velocity on the body surface, also referred to as the *"no slip"* condition, is thus satified if: $v_{si} = 0$ whereupon $v_{si} = v_s = \gamma(s)$.If one neglects the fact that in reality for high Reynolds number flows the boundary layer becomes turbulent and flow might separate due to adverse surface pressure gradients, one can view the present theory as an irrotational potential flow where a surface vorticity sheet separates the irrotational flow of the outer region from the motionless flow on the inner region. It can be concluded that the vorticity model does indeed resembles the physical reality of a real fully attached infinite Reynolds number flow. It is also possible to introduce a model to simulate the viscous diffusion in the boundary and therefore relaxing the infinite Reynolds number condition, but this is out of scope for the present application.

4.1.2 The mathematical formulation of the diffuser

In the previous section it was shown that the vorticity model is a suitable way to numerically describe a potential flow past a solid body. In order to apply this formulation to a 3 dimensional diffuser it is nessary to subdivide the surface of the diffuser into a finite number of panels on which a certain unit vorticity distribution is assumed. By imposing the Dirichlet boundary condition on the velocity at the airfoil's inner surface, it is then possible to calculate the velocities induced by the vortices on one another. The result is a system of linear equations which can be readily solved using standard linear algebra [35]. In order to extent this analysis to circular axi-symmetric airfoil flows, the vorticity distribution of each panel is replaced by a discrete ring vortex, a process originally developed by Kuchemannn and Weber[4]for the analysis of fairings and jet engine inlets.

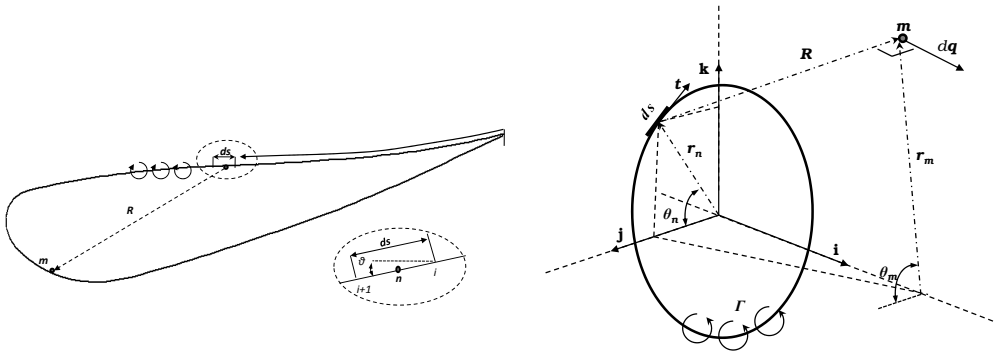

(a) Ringvortex model using Biot Savart formulation

(b) Axisymmetric surface vorticity model for body of revolution [35]

Figure 4.2: Axisymmetric flow modelling using ringvortices

Using the Biot-Savart law to calculate the velocity induced by a ring vortex, one can derive from figure 4.2a the following integral relations for the velocity component u and v induced by a ring vortex n at any point m in space.

$$u_{mn} = \frac{1}{4\pi}\int_0^{2\pi} \frac{r_n - r_m\cos(\theta_m - \theta_n)}{[(x_m - x_n)^2 + r_m^2 + r_n^2 - 2r_m r_n\cos(\theta_m - \theta_n)]^{\frac{3}{2}}} d\theta_n$$

$$v_{mn} = \frac{1}{4\pi}\int_0^{2\pi} \frac{(x_n - x_m)\cos(\theta_n)}{[(x_m - x_n)^2 + r_m^2 + r_n^2 - 2r_m r_n\cos(\theta_m - \theta_n)]^{\frac{3}{2}}} d\theta_n$$

Since these integral equations are rather inefficient from a computational point of view, Riegels (1949, 1952) proposed the use of elliptical integrals. Gibson established the unit ring vortex induced velocities using elliptical integrals in 1972 as the following simple equations [35]:

$$u_{mn} = -\frac{1}{2\pi r_n\sqrt{[x^2 + (r+1)^2]}}\left(K(k) - \left[1 + \frac{2(r-1)}{x^2 + (r-1)^2}\right]E(k)\right) \tag{4.1}$$

$$v_{mn} = \frac{\frac{x}{r}}{2\pi r_n \sqrt{[x^2 + (r+1)^2]}} \left(K(k) - \left[1 + \frac{2r}{x^2 + (r-1)^2} \right] E(k) \right) \tag{4.2}$$

with $x = \frac{x_m - x_n}{r_n}$ and $r = \frac{r_m}{r_n}$ Where K and E are the elliptic integrals of the first and second kind respectively. The modulus of these elliptic intergals is defined by: $k = \frac{4r}{x^2+(r+1)^2}$ Since the vortices described above have a singularity at their core, it is necessary to use a different expression for the self induced velocities. Ryan(1970) derived a simple alternative expression for the self induced velocity of a unit ring vortex. Since this self induced velocity model is based on a Lamb type smoke ring vortex with uniform core, there can only be an axial induced velocity component present, hence:

$$U_{mm} = -\frac{1}{2} - \frac{\Delta s_m}{4\pi r_m} \left(ln \frac{8\pi r_m}{\Delta s_m} - \frac{1}{4} \right)$$

Now that the relations have been established to calculate the unit velocities u and v induced by a ring vortex n at any point in the plane perpendicular to the ringvortex, it can be seen that the potential flow problem of a circular airfoil in a uniform stream V_∞ reduces to:

$$\sum_{n=1}^{M} K(s_m.s_n)\gamma(s_n)\Delta s_n = -V_\infty \cos\beta_m \tag{4.3}$$

with the coupling coefficient defined as:

$$K(s_m, s_n) = U_{mn} \cos\beta_m + V_{mn} \sin\beta_m \tag{4.4}$$

This summation states that the velocity parallel at panel m induced by all the n ring vortices plus the additional freestream velocity V_∞ have to equate to zero. Thus, the problem is reduced to a Dirichlet problem and one can find the vorticity strength γ_n of each panel Δs_n directly by solving the following system of linear equations:

$$\begin{pmatrix} K_{1,1} & K_{1,2} & \cdots & K_{1,n} \\ K_{2,1} & K_{2,2} & \cdots & K_{2,n} \\ \vdots & \vdots & \ddots & \vdots \\ K_{m,1} & K_{m,2} & \cdots & K_{m,n} \end{pmatrix} \begin{pmatrix} \gamma_1 \Delta s_1 \\ \gamma_2 \Delta s_2 \\ \vdots \\ \gamma_n \Delta s_n \end{pmatrix} = -V_\infty \begin{pmatrix} \cos\beta_1 \\ \cos\beta_2 \\ \vdots \\ \cos\beta_n \end{pmatrix} \tag{4.5}$$

4.1.3 Additional considerations

Kelvin's circulation theorem states that the total circulation around the inner surface of the airfoil section induced by the surface vorticity elements should be zero. In order to fulfill this requirement, Lewis [35] suggests a so called back diagonal correction where the back diagonal coupling coefficients are replaced with:

$$K(s_{M+1-m}, s_m) = -\frac{1}{\Delta s_{M+1-m}} \sum_{n=1, n\neq M+1-m}^{M} K(s_n, s_m)\Delta s_n \tag{4.6}$$

In order to find the correct surface vorticity distribution, it is necessary to enforce the Kutta condition at the trailing edge of the airfoil. This can be done by imposing the following restriction on the trailing edge ring vortices on the upper and lower surfaces: $\gamma(te)_{upside} = -\gamma(te)_{downside}$

The approach presented in this section can easily be extended with the previous equations to incorporate the centrebody. The corresponding system of linear equations is then:

$$\begin{pmatrix} K_{Diff.} & K_{Diff.-C.Body} \\ K_{C.Body-Diff.} & K_{C.Body} \end{pmatrix} \begin{pmatrix} (\gamma\Delta s)_{Diff.} \\ (\gamma\Delta s)_{C.Body} \end{pmatrix} = -V_\infty \begin{pmatrix} \cos\beta_{Diff.} \\ \cos\beta_{C.Body} \end{pmatrix}$$

In order to deal with the zero circulation condition on the inner surface of the airfoil, one can apply the back diagonal correction to K_{Diff}. The trailing edge Kutta condition can be applied by substracting row *te+1* from row *te* and column *te+1* from *te*. To obtain a square matrix, one can delete row and column *te+1* to obtain a $n \times n$ matrix again. Figure 4.3 shows the program flow diagram of the above described formulation of an annular airfoil modeling.

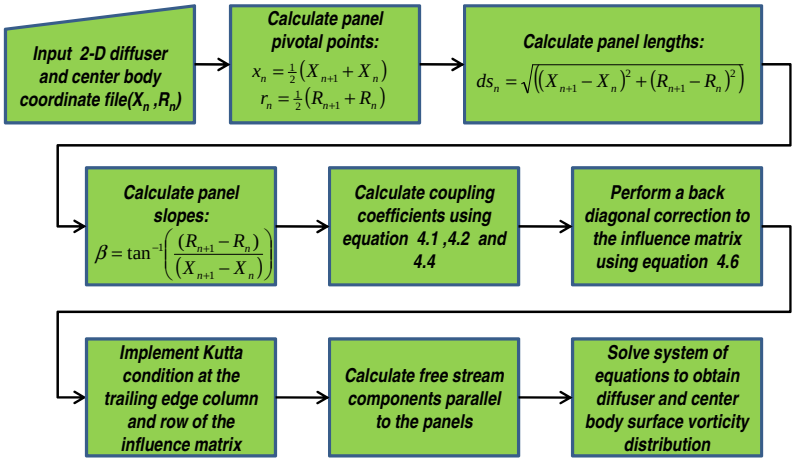

Figure 4.3: Flow diagram of surface vorticity scheme

With the vorticity distribution $\gamma(s)$ along the diffuser surface obtained from the previous calculation, one can obtain the pressure coefficients by applying the following formula:

$$C_p = \frac{P - P_\infty}{\frac{1}{2}\rho V_\infty^2} = 1 - \left(\frac{\gamma(s)}{V_\infty}\right)^2 \tag{4.7}$$

4.2 The rotor lifting line formulation

The foundation for modeling the rotor with the potential flow analysis was formulated by Prandtl [1] in 1922. The method is still being used for preliminary calculations on finite wings, ship and aircraft propeller systems and, as in the present application, wind turbine rotors.

[1] It is argued by some that Lanchester was responsible for initiating the reasoning behind the lifting line formulation

4.2.1 The physical significance of the lifting line formulation

It is well known that the generation of lift by a finite wing or rotor blade is directly related to the pressure difference between the top and bottom surface of the rotor blade or wing. This pressure difference depends on the rotor geometry and smoothly diminishes towards the blade tip. At the tip of the blade the air will flow from the high pressure region on the top surface to the low pressure region on the bottom surface as depicted in figure 4.4b. In effect, a pressure leakage at the tip is maintained when the blade or wing generates a lifting force. This air flow leakage at the tip will cause the streamlines flowing over the blade to deflect towards the tip at the pressure side and towards the center at the suction side. A direct consequence of these streamline deflections is a tangential velocity jump at the trailing edge of the rotor blade as shown in figure 4.4b and 4.4c. Bearing this physical flow behavior in mind, it is possible to represent the tangential velocity jump with a continues vorticity sheet in the wake of the rotor blade.

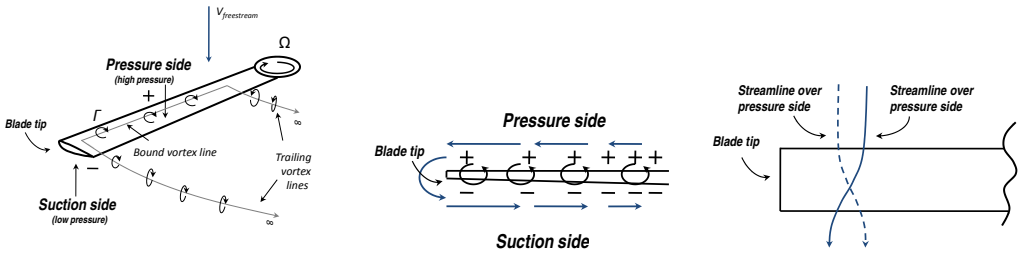

(a) Rotor perspective view

(b) Rotor back view

(c) Rotor top view

Figure 4.4: Rotor idealized flow

From the potential flow theory it is known that a vortex filament of strength Γ is a very suitable way to model the inviscid flow past an airfoil at small angles of attack. The lift generated by the airfoil in a free stream flow is then found through the Kutta-Joukowski theorem as:

$$L = \rho V_\infty \times \Gamma \tag{4.8}$$

By placing a vortex line along the span wise direction of the blade (see figure 4.4a), it is possible to model the lift of the blade. The Helmholtz theorem dictates however that the vortex lines cannot terminate in the interior of a fluid. A way to deal with this condition while taking the physical considerations into account, is to let the bound vortex line extend to infinity behind the rotor blade. The result is a so called horseshoe vortex filament and is depicted in figure 4.4a. By placing a number of these horse shoe vortex filaments next to each other, while letting the trailing vortex line extend to infinity, it is possible to model the span wise lift distribution while satisfying the 3 dimensional flow behavior of the streamlines flowing over the rotor blade (see figure 4.5a). In the real case strong tip vortices cause the wake to roll up around the trailing vortices emanating from the tips. This effect however is neglected in the present analysis. This assumption can be partly justified by the fact that the strength of the vortices emanating from the blade tips inside the diffuser, were indicted by various researchers to be suppressed by the close proximity of the diffuser wall. The induced velocities at the rotor caused by the bound

vortices and trailing vortex sheet is calculated with the Biot-Savart law. While the span wise velocities along the blades are neglected, the induced downwash effecting the angle of attack in a real 3 dimensional flow over a rotor blade is nicely captured by the trailing vorticity sheet. To conclude, as with separated boundary layer effects, the effects due to the Coriolis and centrifugal forces of the rotating blades are not captured with the present model.

4.2.2 The mathematical formulation of the rotor

The approach used in the present mathematical formulation is based on a *"prescribed wake"* or *"rigid wake"* method. As described in the previous section, the blades are replaced by lifting lines with a predefined geometry [7] [47]. The lifing line is a spanwise bound vorticity distribution with accompanying helical shaped trailing vortex lines that are shed from the blade element corners (see figure 4.5a and 4.9a). Again, through the application of the Biot Savart law in combination with the Kutta-Jouwkowski theorem and 2 dimensional airfoil data, it is possible to obtain the strength of each individual blade element horseshoe vortex.

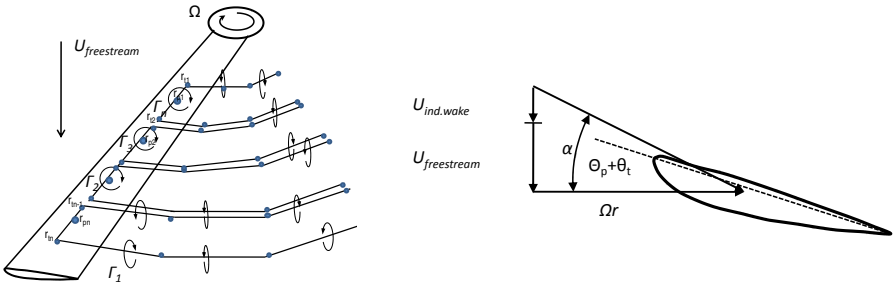

(a) Blade horseshoe Vortex Elements

(b) Velocity Diagram Blade

Figure 4.5: Schematic rotor modeling diagrams

The program routine to perform these Biot-Savart calculations is based on formulation as derived by Katz and Plotkin[28][2].

Rotor wake geometry definition

Before any wake induced velocities can be calculated, it is necessary to first prescribe the wake geometry. Each trailing line follows a helical path consisting of small straight vortex line segments as shown in figure 4.6b. With equation 4.9 one can calculate the coordinates of the corner points of each vortex line segment.

$$r_{wake} = (V_W t + Xpos, rTtip\cos(t), rTtip\sin(t)) \tag{4.9}$$

[2]See appendix B

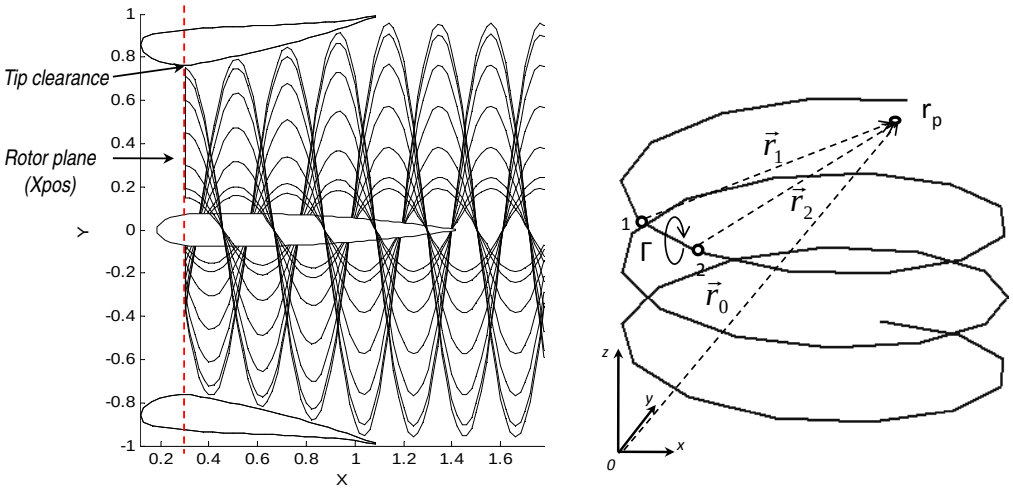

(a) Wake geometry inside the diffuser

(b) Vortex line segment convention

Figure 4.6: Schematic wake modeling

With the variable *'tip'* it is possible to prescribe a suitable wake expansion inside the diffuser such that the wake geometry follows the diffuser's inside contour. Thus, variable *'tip'* depends on the diffuser's suction side contour and is obtained by dividing the local diffuser radius r_{ld} minus the blade tip clearance r_{btc}, with the blade tip radius $r_{T_{tip}}$:

$$tip = \frac{r_{ld} - r_{btc}}{r_{T_{tip}}}$$

The maximum radius of the helical wake behind the diffuser, is chosen to be the same as the radius of the diffuser exit plane as depicted in figure 4.6. The constant V_W, referred to as the helical wake propagation velocity[3], is defined as a fraction of the freestream flow and is used to control the helical pitch of the wake. The value of V_W does not vary axially and does consequently not incorporate a correction to satisfy the mass continuity.

Wake influence matrices

With the use of the Biot Savart equation 4.10 and vortex line segment convention shown in figure 4.6b, one can calculate the induced velocity at any given point in space.

$$q_{1,2} = \frac{\Gamma}{4\pi} \frac{\vec{r_1} \times \vec{r_2}}{|\vec{r_1} \times \vec{r_2}|^2} \vec{r_0} \cdot \left(\frac{\vec{r_1}}{r_1} - \frac{\vec{r_2}}{r_2} \right) \tag{4.10}$$

The total downwash velocity $U_{ind.wake}$, induced by the wake at the blade collocation points is the summation of all these vortex line segment induced downwash velocities of each

[3]The reason for the introduction of the factor is to be able to control the wake geometry and thus the influence coefficients. The factor can be viewed as the velocity behind the rotor in the wake and in chapter 7 extensive use is made of this factor when matching the pressure curves

horseshoe vortex element hs_n multiplied by the applicable horseshoe vortex strengths:

$$\begin{pmatrix} K_{U_{(r_{p1},hs_1)}} & K_{U_{(r_{p1},hs_2)}} & \cdots & K_{U_{(r_{p1},hs_n)}} \\ K_{U_{(r_{p2},hs_1)}} & K_{U_{(r_{p2},hs_2)}} & \cdots & K_{U_{(r_{p2},hs_n)}} \\ \vdots & \vdots & \ddots & \vdots \\ K_{U_{(r_{pn},hs_1)}} & K_{U_{(r_{pn},hs_2)}} & \cdots & K_{U_{(r_{pn},hs_n)}} \end{pmatrix} \begin{pmatrix} \Gamma_1 \\ \Gamma_2 \\ \vdots \\ \Gamma_n \end{pmatrix} = U_{ind.wake} \tag{4.11}$$

Appendix B shows the routine to perform these calculations and to obtain the wake induced velocity influence matrices K_U, K_V and K_W. To avoid any singularity problems when calculating the influence coefficients, use is being made of the Lamb-Oseen vortex model which is defined as:

$$K_v = \frac{h^2}{(r_c{}^{2z} + h^{2z})^{1/z}} \tag{4.12}$$

This expression can simply be put in front of the induced velocities calculated by the Biot Savart law with r_c as the core radius[4],h the perpendicular distance between the vortex elements and evaluation points with $z = 2$[47].

Rotor iteration scheme

The total velocity vector locally at the blade collocation points (see figures 4.5a and 4.6b), in the absence of the diffuser induced velocities, is defined as:

$$\vec{V_t} = \begin{pmatrix} U_t \\ V_t \\ W_t \end{pmatrix} = \begin{pmatrix} U_\infty \\ 0 \\ 0 \end{pmatrix} + \begin{pmatrix} U_{ind.wake} \\ 0 \\ 0 \end{pmatrix} + \begin{pmatrix} 0 \\ V_{rot.} \\ W_{rot.} \end{pmatrix} \tag{4.13}$$

With $\sqrt{V_{rot.}^2 + W_{rot.}^2} = \Omega r_{p_n}$ as the velocities at the blade collocation points due to the rotating blades. The effective angle of attack locally at the blade collocation points, while taking the blade pitch and twist into account, is then determined with equation 4.14

$$\alpha_{r_{p_i}} = \arctan\left(\frac{U_t}{\sqrt{V_t^2 + W_t^2}}\right) - (\theta_p + \theta_t) \tag{4.14}$$

Using these angles of attack $\alpha_{r_{p_i}}$, it is possible to obtain the lift and drag coefficients by interpolating in the polar data[5] as given in appendix C. By applying the Kutta Jouwkowski theorem (eq. 4.8) one can obtain a new blade bound vorticity strength from the previous calculated lift with the effective velocity as given in equation 4.13. To establish a good convergence, the scheme uses a bisectional iteration with a relaxation factor of $\epsilon = 0.05$ as shown in the flow diagram of figure 4.7.

[4]The core radius applied in the present model is 0.0001

[5]The polar curve for the NACA 2207 blade profile is obtained from Xfoil with a Reynolds number of 6e5

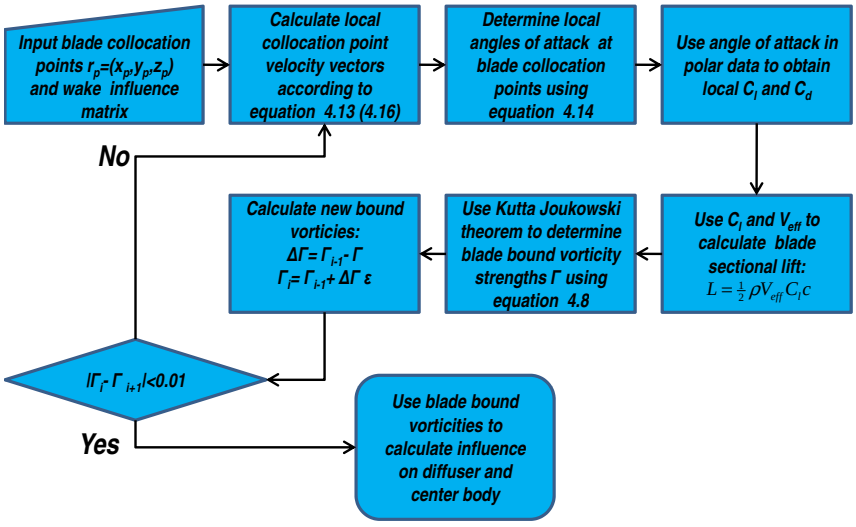

Figure 4.7: Wake - rotor influence coefficient calculation scheme

4.3 The implementation of the diffuser and rotor codes

In the present section the previous described models for the diffuser and rotor are combined in a coherent iteration scheme. The key adaptation in the iteration scheme is to incorporate the mutual induced velocities of the rotor and diffuser. Ryan and Glover [44] formulated a ducted propeller design model for ship propulsion systems with some resemblance with the theory presented so far. Although the rotor model is based on different design approaches, use is made of their iterative scheme to compute the vorticity strength distribution of the duct, center body, rotor and their mutual influence. In each iteration step a new wake geometry is calculated with corresponding wake influence coefficients. The scheme shown in appendix B is also applicable to calculate the wake induced velocities on the diffuser's collocations points. Flow diagram 4.8 illustrates the approach.

4.3.1 Diffuser-rotor iteration scheme

First, the bare rotor is analyzed and the bound vorticity strengths are obtained, as outlined in section 4.2.2, while assuming a wake geometry with a helical pitch distribution equal to the blade twist distribution. With the calculated vorticity strengths of the wake, it is possible to calculate the velocities induced at the collocation points on the diffuser and center body due to the wake. As noted earlier, the iteration scheme shown in appendix B can be used to perform these calculations. Since the schemes and equations presented in section 4.1.2 make use of rotational symmetry, one needs to calculate the rotational average wake induced velocity components $\vec{V}_{\overline{ind.wake}}$ in the X-Y plane of the diffuser and centerbody as shown in figure 4.6b. The total velocity vectors at the diffuser

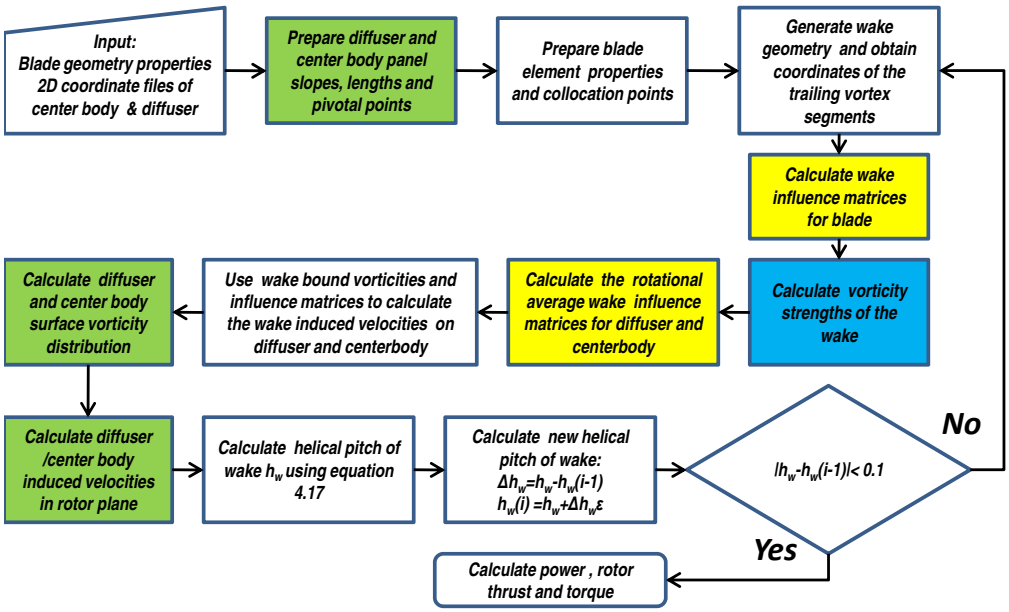

Figure 4.8: Top flow of DAWT computational scheme

and center body collocation points $\vec{V}d_t$ are defined as:

$$\vec{V}d_t = \begin{pmatrix} U_\infty \\ 0 \\ 0 \end{pmatrix} + \begin{pmatrix} U \\ V \\ 0 \end{pmatrix}_{C.Body} + \begin{pmatrix} U \\ V \\ 0 \end{pmatrix}_{diff.} + \begin{pmatrix} U \\ V \\ 0 \end{pmatrix}_{\overline{ind.wake}} \tag{4.15}$$

The rotational average wake induced velocities ($\vec{V}_{\overline{ind.wake}}$) are obtained by rotating the wake over 360°.Again, satisfying the Dirichlet condition on the diffuser and centerbody inside contour leads then to the following system of equations:

$$\begin{pmatrix} K_{Diff.} & K_{Diff.-C.Body} \\ K_{C.Body-Diff.} & K_{C.Body} \end{pmatrix} \begin{pmatrix} (\gamma\Delta s)_{Diff.} \\ (\gamma\Delta s)_{C.Body} \end{pmatrix} = -Ud_t \begin{pmatrix} \cos\beta_{Diff.} \\ \cos\beta_{C.Body} \end{pmatrix} - Vd_t \begin{pmatrix} \sin\beta_{Diff.} \\ \sin\beta_{C.Body} \end{pmatrix}$$

From this system of equations, one can calculate the proper vorticity distribution $\gamma(s)$ on the duct and hub under the influence of the wake. This surface vorticity distribution can then be used to calculate the induced velocities of the duct and centre body in the rotor plane according to equations 4.1 and 4.2. The new velocity vectors at the blade collocation points have now an extra term accounting for the diffuser induced velocity as shown in figure 4.9b and equation 4.16

$$\vec{V}_t = \begin{pmatrix} U_t \\ V_t \\ W_t \end{pmatrix} = \begin{pmatrix} U_\infty \\ 0 \\ 0 \end{pmatrix} + \begin{pmatrix} U_{ind.wake} \\ 0 \\ 0 \end{pmatrix} + \begin{pmatrix} 0 \\ V_{rot.} \\ W_{rot.} \end{pmatrix} + \begin{pmatrix} U \\ V \\ 0 \end{pmatrix}_{diff.R} \tag{4.16}$$

The helical pitch is then recalculated and leads thus to a new wake geometry. The new wake geometry will lead to new wake influence matrices for diffuser/centerbody and rotor plane. Evidently, from these new influence matrices one can calculate new velocity vectors, diffuser/centerbody vorticity distributions and rotor bound vorticity distributions. From the velocity vectors at the blade collocation points one can calculate a new pitch, and the whole sequence is repeated. The new helical pitch distribution of the wake is calculated by adapting a variant of Meakawa's [37] formulation:

$$h_w = \frac{U_\infty + U_{C.Body} + U_{ind.Wake} + U_{ind.diff}}{\left(\Omega r + \sqrt{(V_{wake}^2 + W_{wake}^2)}\right)} \tag{4.17}$$

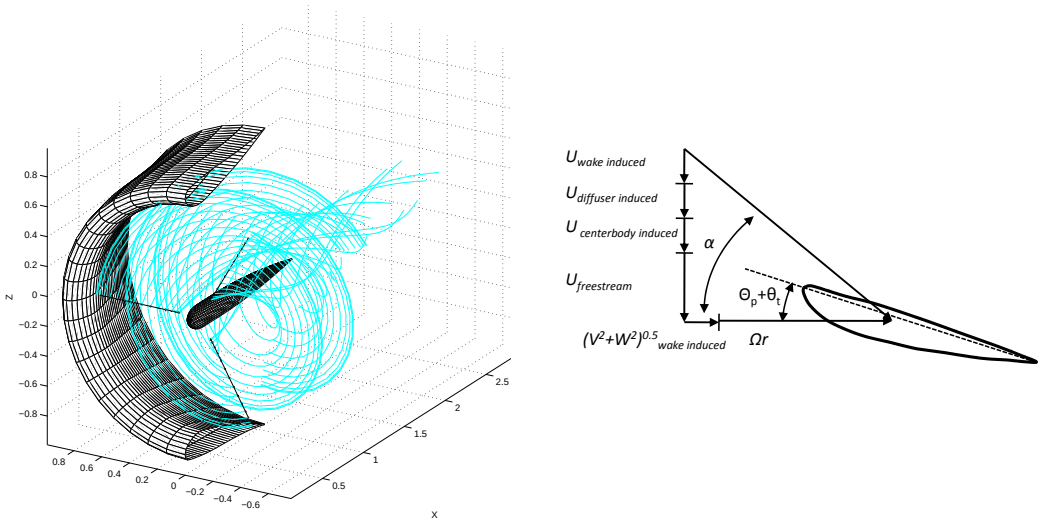

(a) Diffuser wake

(b) Rotor blade velocity diagram with diffuser influence modeling

Figure 4.9: diffuser wake modelling

Figure 4.9b shows the various velocity components at the blade section. Figure 4.9a shows a picture of the complete DAWT with an adapted wake helical pitch distribution. Like the rotor iteration, in order to let the scheme converge properly use is being made of a bi-sectional iteration with a relaxation factor of ϵ=0.01. The helical pitch given in equation 4.17 is multiplied by the wake propagation velocity V_W . The new wake coordinate function is thus defined as:

$$r_{wake} = ((1 + L/i)h_w V_W t + Xpos, rTtip\cos(t), rTtip\sin(t)) \tag{4.18}$$

The $(1+\frac{L}{i})$ term is used to control the axial variation of the helical pitch distribution with 'i' as the i^{th} vortex line segment from the rotor plane. It has been been found that the variable L heavily depends on the V_W and h_W. For the analysis in chapter 7, it has been found that the behavior is reasonably captured when L=6. The routine of the DAWT potential flow calculations as implemented in MATLAB is shown in figure 4.8

Chapter 5

Experimental Apparatus and Procedures

The full scale DAWT under consideration has been tested in 2 different open wind tunnels in 4 separate testing campaigns. The first 2 tests campaigns where performed in the low speed open wind tunnel at Von Karmann Institute(VKI) in Brussels, Belgium. The second set of testing campaigns where performed in the Open Jet Facility(OJF) of Delft University of Technology. The OJF of the TUDelft has an octagonal nozzle of 285×285 cm and has a maximum wind speed of 35 m/s. The following sections give a detailed account of the test set up and procedures used in second 2 test campaigns in the OJF, from now reffered to as phase 1 and 2 respectively. For a detailed account of the tests performed at VKI one is referred to the literature study including the VKI test report #2 [51].

5.1 The DAWT of Donqi Urban Windmills

The Diffuser Augmented Wind Turbine under investigation is provided by Donqi Urban Windmills and will be the test platform throughout this investigation. The 3 bladed rotor has a diameter of 1500 mm and a nominal power output of 1750 W. The diffuser itself is a circular airfoil with the suction side pointing inwards with an area ratio of 1.7286. Blades and diffuser have been designed with *CFD* by *NLR* [42]. The exit plane of the diffuser has a diameter of 2000 mm and is equipped with a Gurney flap of 40 mm. Table 5.1 shows some performance characteristics. One can find more detail on the geometry of the diffuser and blade in appendix C.

5.2 Vortex generator specification

As described in chapter 3, the application of delta shaped vortex generators on the diffuser's trailing edge seems to be the best way to promote mixing. In the earlier test

Table 5.1: DAWT performance characteristics

Nominal power	1750 W
Maximum power	2250 W
Output Windspeed	12.5 m/s
Output RPM	1500
Cut-in windspeed	2.5 m/s
Cut-out Windspeed	30 m/s

campaigns performed at VKI, the application of small delta tabs with an height of approximately 5 cm lead to a power increase of about 10 % [51]. Thus, it seems only natural to test this observation again but with bigger delta shaped vortex generators. The aim of the present investigation was originally to test 3 different delta shaped vortex generator geometries. But due to the limited wind tunnel time it was decided to proceed with delta vortex generator model 3 as depicted in figure 5.1b.

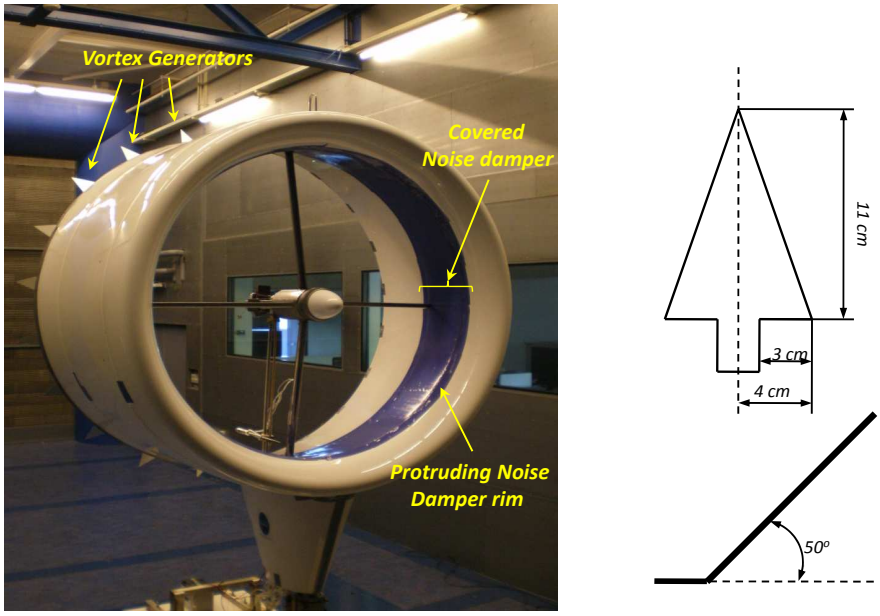

(a) DAWT equipped with vortex generators

(b) Vortex generator dimensions

Figure 5.1: The VG equipped DAWT

5.3 Test phase 1

Test phase 1 consisted of 3 days of which the first day was used to get the test set-up completely operational. The second and third day where mostly devoted to the acquisition of power augmentation data that is presented in section 6.1. Also, some force measurements on rotor and balance were performed, and a few pressure profile scans of the diffuser perimeter and behind the rotor were obtained.

A lot of extra features have been added since the last wind tunnel tests at VKI; The diffuser has been equipped with 88 static pressure orifices with a diameter of 0.5 mm distributed around the perimeter of the diffuser cross section. Around the leading edge and the rotor region the consecutive distance between the orifices is 2 cm. For the remaining orifices the consecutive distance is 3 cm. Figure 5.2a shows a picture taken of the installation of the tubing and orifices during the DAWT manufacturing[1].

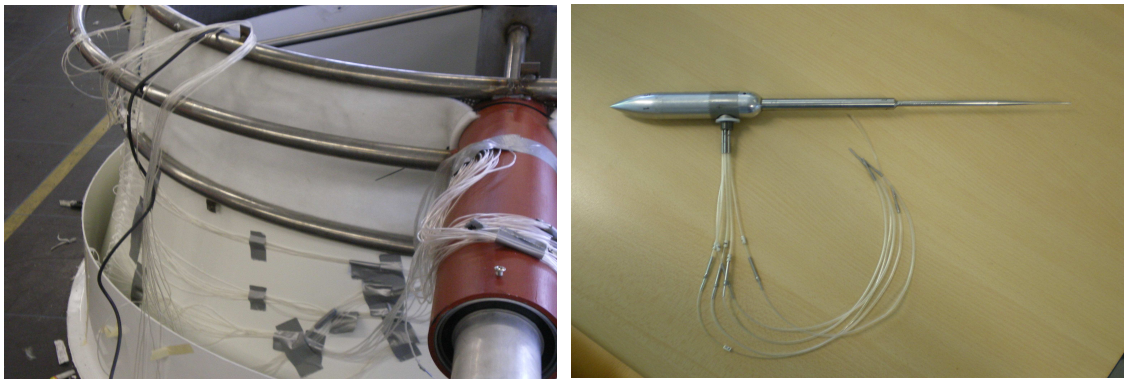

(a) Construction of DAWT (b) 5 hole pressure probe

Figure 5.2: Pressure instruments

With the use of a low pressure sensor and a scanning mensor with a delay time of 3 seconds, it was possible, with the help of a dedicated *Labview* program, to assess the pressures around the diffuser reasonably quickly. Figure 5.3b shows a picture of the scanning valve. A semi automatic radial traversing system was employed to facilitate a 5 hole pressure probe as shown in figure 5.2b. With this 5 hole pressure probe it was possible to measure the slip angle, angle of attack (-45° to 45°) and velocity of the swirling flow behind the rotor. These quantities where deduced from the 5 pressure readings and then matched through a bilinear interpolation scheme with the calibration data[2]. The tip of the pressure probe was positioned 37 cm behind the leading edge or 7 cm behind the rotor plane. In order to have enough clearance from the wake emanating from the support trusses, the tip of the probe was placed 10 cm next to vertical centerline of the rotor axis. Figure 5.3a shows an illustration of the set up.

Furthermore, the whole test set up was placed on a custom build force scale as shown in figure 5.4 The force balance consisted of a frame suspended by thin stainless steel blades of about 2 mm. The balance effectively worked like a couch hammock, thus able to swing nearly frictionless back and forth. The force scale was equipped with 4 weighing scales which were obtained from a personal weighing scale with an accuracy of 100 grams. Also, the generator of the rotor was placed on an axial traversing sledge with the same weighing scale sensors installed behind the rotor in order to assess the rotor thrust. The software and inverter where improved to reduce losses and to optimize the generator control.

Unfortunately, the weighing scale sensors proved to be tedious to operate, especially the ones behind the rotor. After a few runs the rotor sensors failed, probably due to the vibrations and electric interference induced by the generator. At the end of test phase

[1]The tubes are glued to the diffuser with a dedicated power glue that can adhere to PolyEthylene
[2]See appendix A for a detailed description

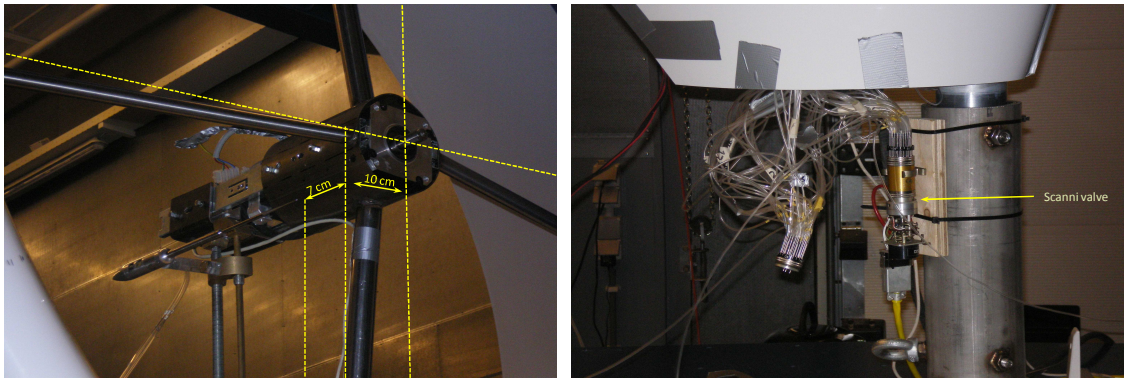

(a) Axial and radial rotor measurement systems

(b) Scanni Valve arrangement

Figure 5.3: Force and pressure instruments

1 it was decided to remove the Gurney flap so that the impact of the vortex generators on the trailing edge could be properly assessed and referenced to the bare trailing edge DAWT configuration.

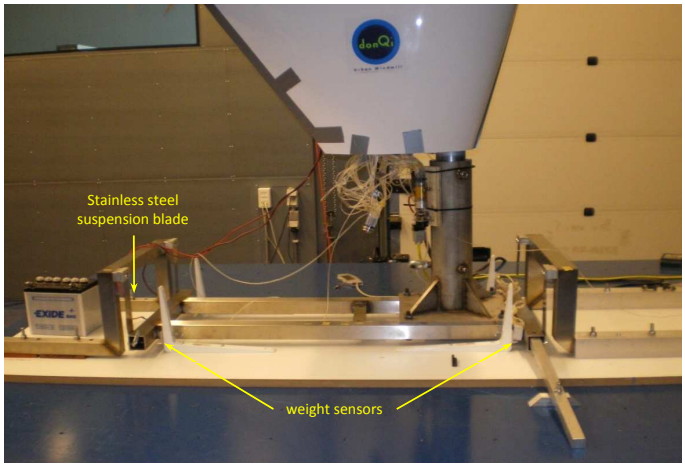

Figure 5.4: Axial force measurement balance

5.4 Test phase 2

From the first phase it became clear that more resolution in the pressure distribution over the leading edge would be desirable. Also, due to a small manufacturing fault in the vacuum forming of the leading edge, the noise damper was not entirely aligned with the diffuser's leading edge. Hence it was decided to replace a small leading edge section with a slightly bigger section to ensure a continues surface between the connecting section of the leading edge and noisedamper. This new section was also equipped with 46 additional static pressure orifices as shown in figure 5.5b.

As already mentioned, the load sensors used in phase 1 turned out to be not suitable for measuring the thrust on the rotor. Therefore, all load sensors were replaced by a set of

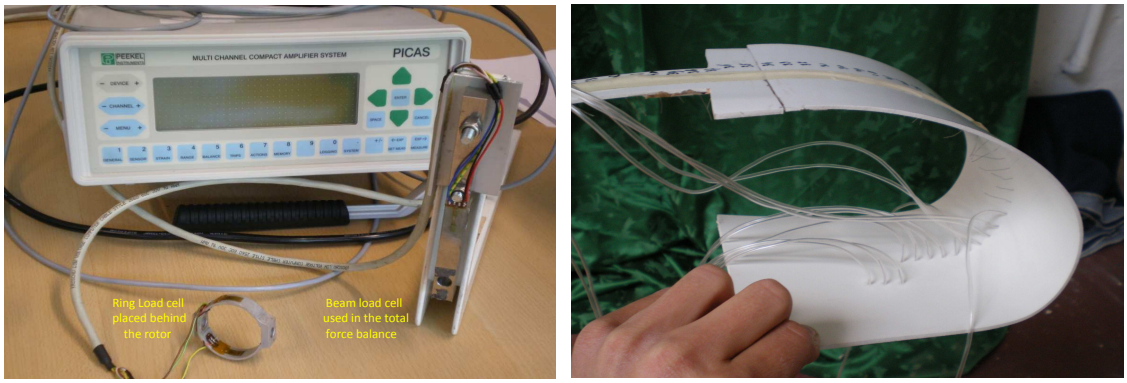

(a) Picas Signal Amplifier and load cells (b) Faired section installment

Figure 5.5: Test set up adaptations

calibrated load cells as depicted in figure 5.5a. The ring shaped load cell was capable of handling loads up to 40 kg. The beam shaped one was capable of handling a maximum load of 200 kg. Both sensors had an accuracy of about 50 to 100 grams. A DEWE 43 and Picas amplifier where used to amplify the signal outputs of these load cells [3]. Also, it was desirable to make some pressure measurements at the exit plane and further behind the diffuser. The same 5 hole pressure probe was therefore mounted on a manually traversing unipod. Figure 5.6a shows the placement of this unipod traversing mechanism behind the diffuser exit plane. The unipod was placed such that the pressure probe tip was 10 cm behind the diffuser exit plane. Furthermore, the vertical traversing was performed parallel to the vertical centerline of the rotor at a distance of 37 cm to the right.

5.5 Test accuracy considerations

Although great care has been taken in making sure that the experiments were performed in a consistent and repeatable manner, it was found that there were contradictions in the measurements. The flow angle profiles obtained with the 5 hole pressure probe showed to be the most inconsistent ones but it was also found that there where inconsistencies in the other measurements as well(see appendix D). Since the aim of the present experiments was to asses the augmentation potential governed by flow phenomena which were found to be not very pronounced, it is hard to say whether all of the presented results are either the real situation or measurement inaccuracies. Unfortunately due to limited time, most of measurement runs have only been performed twice and in some cases even once. The measurement results indicate that the conditions in test phase 1 and test phase 2 were not identical. This might have been caused by the fact that DAWT was not positioned at exactly the same position in both test phases. Another possible factor for the discrepancies between test phases is that the DAWT itself was slightly damaged during transport. Even though these damages were fixed with great care, it is possible that the diffuser shape did not had an 100 % identical shape in both test phases. Another factor closely related to the position of the DAWT relative to the windtunnel nozzle is the uncertainty due to the solid blockage and nozzle blockage effects of the DAWT on the wind tunnel flow

[3] Load cell voltages where in the order of 0.1 mV

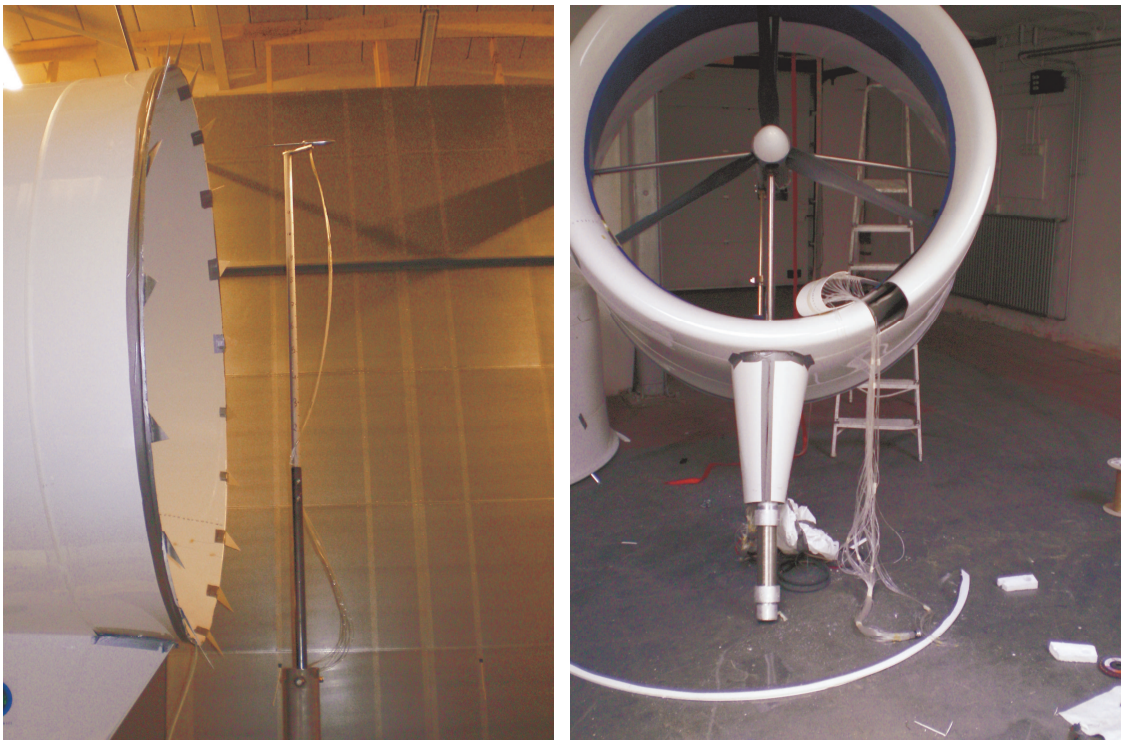

(a) Unipod velocity measurement behind 10 cm diffuser exit plane

(b) Faired section installment

Figure 5.6: Test set up adaptations

[10]. Measurements performed in front of the DAWT showed that there was a velocity discrepancy of about 10% with the indicated wind tunnel velocity. It is impossible at this point to say what the individual contributions are of these blockage effects let alone to correct for them. To conclude, it has been reported from field measurements by Donqi Urban Windmill that the DAWT performs considerably better in the open environment than the result presented in the following chapter indicate.

Chapter 6

Test Result Analysis

As described in the previous chapter, a variety of different test set up configurations were applied throughout the four measurement campaigns. It would therefore be inappropriate to directly compare all the results obtained with one another. Also, only the last two measurement campaigns in the *OJF* where strictly devoted to the investigation of DAWT vortex generator's. Therefore the emphasis of the present data analysis is laid on the results obtained in the *OJF*. Furthermore, one has to bear in mind that measurement inaccuracies, as explained in section 5.5, could be the perpetrator of the various observations presented in this chapter. Especially the rotor force and 5 hole pressure probe measurements where found to be subjected to inaccuracies of upto 10%.

6.1 DAWT performance characteristics

The big difference between the VG application described earlier (chapter 3) with the present application is that the flow is swirling due to the rotating blades. Thus, in order to confirm that the 50 degree titled backward configuration is the most suitable one, a number of different configurations were applied as shown in table 6.1. Figure 6.1 shows the P-V curve of these different configurations in terms of augmentation factor as defined by equation 6.1. A value of r=1 corresponds to the Betz limit referenced to the diffuser exit plane.

$$r = \frac{P_{gen.}}{\frac{16}{27}\frac{1}{2}\rho V_{\infty}^{3} A_{diff.exit}} \tag{6.1}$$

All values presented are obtained at the highest attained power for each corresponding windspeed. If the tipspeed ratio λ is defined with the freestream velocity, as in equation 6.2 [31], corresponding tipspeed ratios ranging from approximatly 6 to 6,5 are found. Config. 2 turns out to be the best performing configuration of the vortex generators. A quick comparison of config. 8 and 9 shows that, also in the absence of a Gurney flap, the power augmentation factor increases with about 3 to 9 %. Also, by covering

the noisedamper with adhesive plastic an power augmentation gain of upto 9 % can be established. Especially in the lower velocity regions of upto 7 m/s this increase seems to be most pronounced. This augmentation increase is probably caused by a smoother surface and transition of leading edge to noisedamper.

$$\lambda = \frac{r\Omega}{V_\infty} \tag{6.2}$$

config	Diffuser trailing edge configuration
config. 1	15 VG's straight up - on top of Gruney flap pointing outside
config. 2	15 VG's titled 50° down stream - on top of Gurney flap pointing outside
config. 3	15 VG's titled 50° down stream - on top of Gurney flap pointing inside
config. 4	15 VG's titled 50° up stream - on top of Gurney flap pointing outside
config. 5	15 VG's titled 50° up / down stream - on top of Gurney flap pointing ouside
config. 6	No VG's -with Gurney flap
config. 7	No VG's -with Gurney flap - noisedamper covered
config. 8	No VG's - No Gurney flap-noisedamper covered
config. 9	31 VG's pointing outside 50° downstream-No Gurney flap-noisedamper covered

Table 6.1: DAWT configuration phase 1

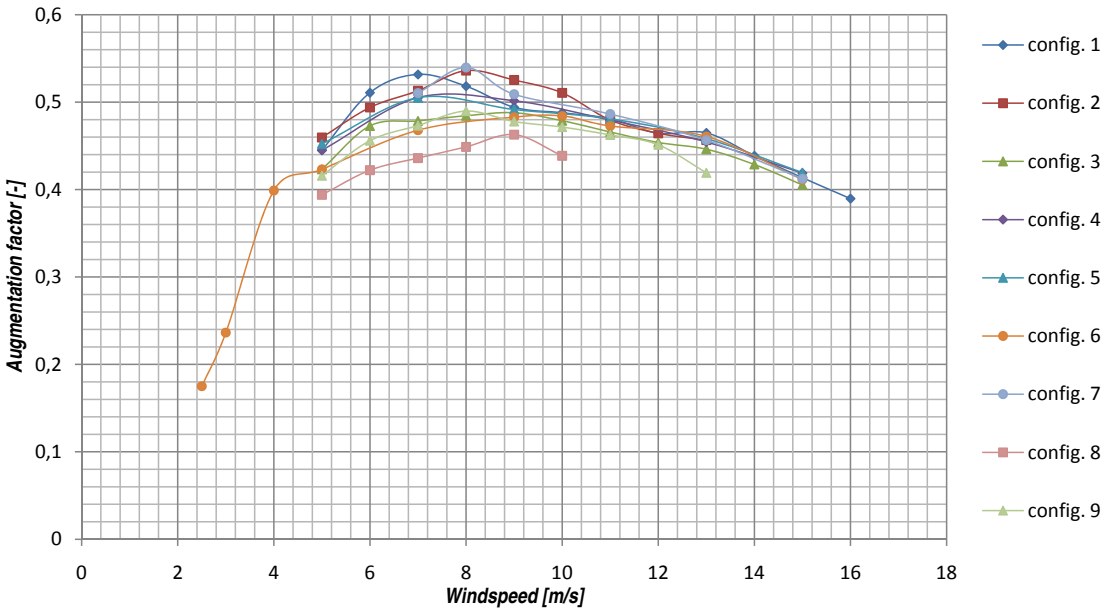

Figure 6.1: Augmentation factor v.s. windspeed (phase 1)

$$C_T = \frac{F_t}{\frac{1}{2}\rho V_\infty^2 \frac{\pi}{4} D^2} \tag{6.3}$$

Using equation 6.3 and the total axial force F_t obtained from the force balance system, figures 6.2 and 6.3 can be produced. From figure 6.2 it is evident that config. 8 and 9 are the ones without a Gurney flap because of a lower total thrust and corresponding drag value as compared to the other configurations. Config 1,4 and 5 have the highest thrust coefficients while the configuration with the highest power augmentation factor, config 2, tends to stay in the lower margin of the thrust coefficients. Furthermore, the thrust of all the configurations levels off at increasing windspeeds. An interesting plot is presented in figure 6.3 in which it can be seen that the best performance is obtained at a total thrust coefficient between 1 and 1.05. A thrust increase beyond this value seems to have a decrimental influence on the power augmentation. Figure 6.3 also illustrates the effect of the VG's on the bare configuration. Config. 8 (no Gurney , no VG's) does not only have lower augmentation factors, but also the peak augmentation has a different thrust coefficient. To conclude this section, it can be observed that by applying progessively more augmentation devices such as the Gurney flap and/or VG's on the bare diffuser, higher DAWT performances and thrust coefficients can be obtained.

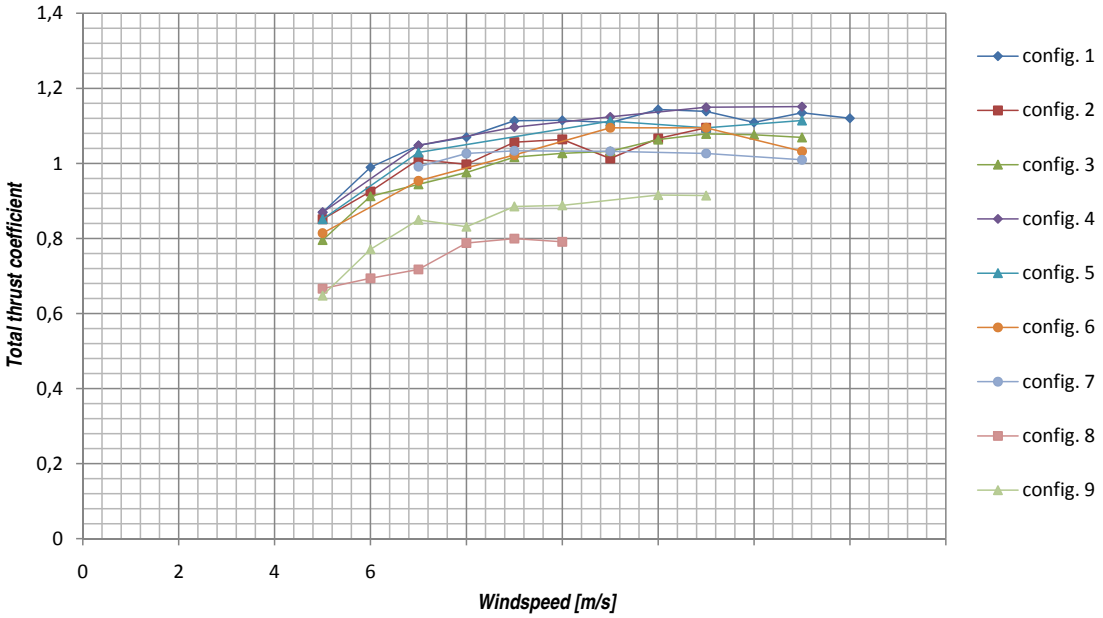

Figure 6.2: Total thrust coefficient v.s. windspeed (phase 1)

6.2 Diffuser wall pressure measurements

All static pressure results presented in this section were obtained from the static pressure orifices on the diffuser wall and are referenced to the atmospheric pressure as measured in the open section of the wind tunnel. It has to be noted that this atmospheric pressure is approximatly the same as the static pressure measured at the exit plane of the windtunnel nozzle. If equation 4.7 is applied, while taking the highest measured pressure on the shroud as the stagnation pressure, and using the indicated wind speed as input for the dynamic pressure, one ends up with the pressure coefficient plots as depicted in figure 6.4a and 6.4b.

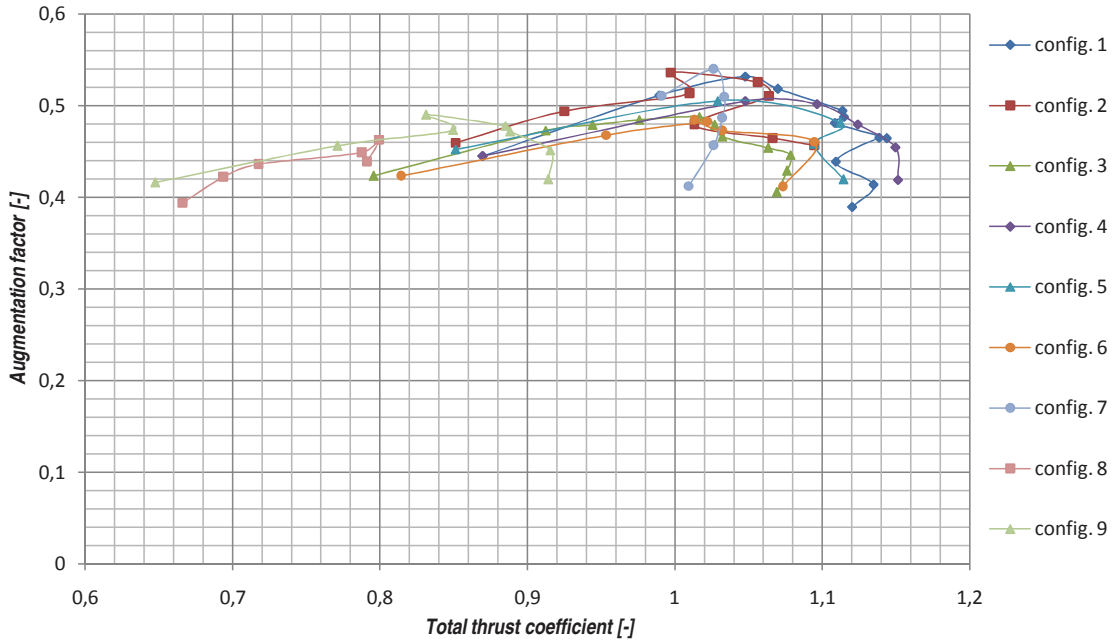

Figure 6.3: Augmentation factor v.s. total thrust coefficient (phase 1)

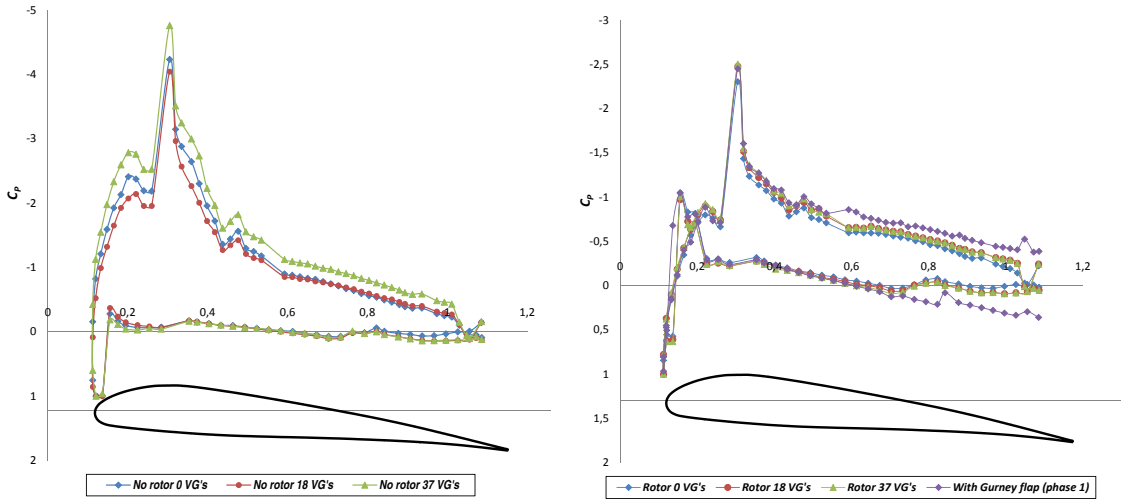

(a) Pressure coefficient distribution without Rotor (phase 2)

(b) Pressure coefficient distribution with Rotor (phase 2)

Figure 6.4: Diffuser wall pressure distributions

As a start, a few remarks have to be made regarding these plots. First of all, the spike observed on the suction side at about 0,25 chord position in the rotor and non rotor case is due to the noise damper rim that is slightly sticking out of the diffuser profile (see figure 5.1a and 5.6b). As the flow approaches the noise damper it has to negotiate itself over the protruding rim of the noise damper. This causes the flow to separate close in front of the protruding rim to reattach again behind it. In the fairing case this behavior is

also observed , albeit in a less severe fashion. The fairing section has a nearly continuous transition of leading edge onto the noise damper but never the less it can be expected that the flow over the fairing still experiences the influence of the noise damper rim of the none faired surrounding. This is clearly illustrated in figure 6.6a which shows the pressure coefficients deduced from the pressure readings measured on the fairing without an operating rotor. At about 0,42 chord position another small spike in the pressure curve can be observed. This spike is caused by a small separation bubble present right behind the noise damper. Figure 6.5 shows an schematic drawing of the flow just infront and behind the noise damper. The behavior of the flow around the noise damper will be demonstrated in chapter 7. Unfortunatly this protruding noisedamper rim is positioned close to the rotor plane and it is likely that the rim will influence the static wall pressure measurements at the postion of the rotor.

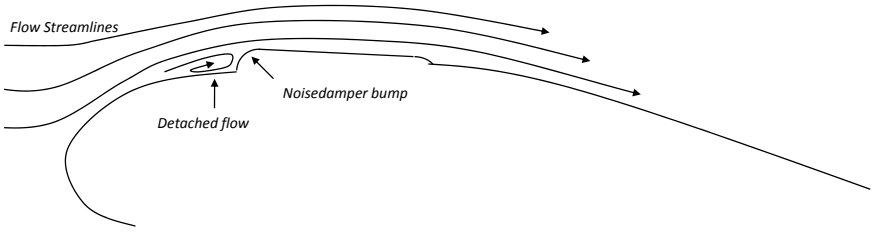

Figure 6.5: flow detachement infront of the noisedamper bump inside the diffuser

If figure 6.4a and 6.4b are compared with one another it seems that the effective angle of attack is decreased when an operating rotor is installed. Although the position of the stagnation point has not shifted significantly, there does seem to be a higher velocity present at the pressure side of the leading edge when an operating rotor is present inside the diffuser, thus suggesting a flow blockage by the operating rotor that starts to manifests itself some distance infront of the rotor. So in effect, the flow is more or less pushed around the diffuser by the rotor. This behavior is also illustrated in figures 6.6a and 6.6b where a higher velocity on the pressure side can be observed when a operating rotor is present. A quick comparison between the pressure distributions over the faired and non faired section reveals that the peak and slope of the pressure spike at 0.3 chord postion is nearly identical. The pressure side of the fairing section does however seems to reach higher velocities. This is probably due to the changed leading edge shape which has a blunter nose section.

When the diffuser's trailing edge is equipped with progressively more delta shaped vortex generators (see figure 5.1 for a description) it is observed that the diffuser is in fact operating at higher apparent angles of attack. The pressure coefficient on the pressure side increases slightly while on the suction side a small decrease can be observed. This observation is especially noticeable near the trailing and leading edge of the diffuser. Thus, in terms of static pressure distribution, it does indeed seems that the delta shaped vortex generators do increase the velocity close to the diffuser inside wall and consequently the mass flow.

A quick comparison with the original Gurney flap configuration shows that this effect is even more pronounced when a gurney flap is in place. From this observation one could therefore question whether the velocity increase at the trailing edge in the VG

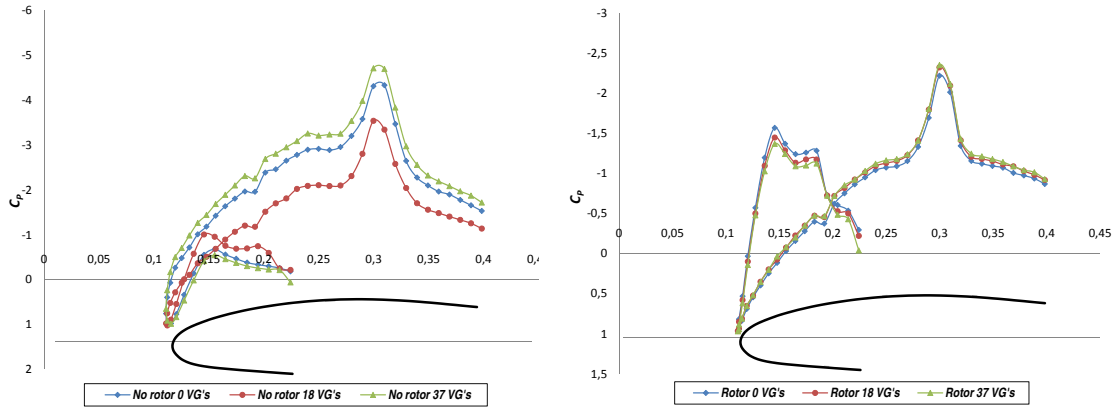

(a) Pressure coefficient distribution without Rotor (fairing case) (phase 2)

(b) Pressure coefficient distribution with Rotor (fairing case)(phase 2)

Figure 6.6: Diffuser fairing pressure distributions

configuration is due to the streamwise vorticity mixing or that the vortex generators are in fact functioning effectively as a small Gurney flap. So in order to prove that the increase in surface velocity on the suction side is caused by enhanced mixing behind the diffuser exit plane and not due to Gurney flap enhanced circulation, it is necessary to quantify the behavior of the C_p distribution.

Extending the reasoning as explained in chapter 2 regarding the force exerted by the diffuser on the flow, one can integrate the pressure distributions over the diffuser wall according to equation 6.4 and 6.5 to obtain an axial and radial total force coefficient.

$$C_n = \frac{1}{c}\left[\int_0^c (C_{p,p} - C_{p,s})\,dx + \int_0^c \left(C_{f,p}\frac{dy}{dx} + C_{f,s}\frac{dy}{dx}\right)dx\right] \tag{6.4}$$

$$C_a = \frac{1}{c}\left[\int_0^c \left(C_{p,s}\frac{dy}{dx} - C_{p,p}\frac{dy}{dx}\right)dx + \int_0^c (C_{f,p} - C_{f,s})\,dx\right] \tag{6.5}$$

Unfortunately due to unknown nature of the windtunnel flow, no conclusive assumption can be made regarding the boundary layer present on the diffuser's surface. If *" the worst case scenario"* of a turbulent flow over the diffuser's surface is assumed with an Reynolds number[1] of 6×10^5, then it can be shown through equation 6.6 [33] that the total friction coefficient would atleast be an order of magnitude smaller than the total pressure coefficient. A 2 dimensional viscous analysis with Xfoil shows a total friction coeffient of even 3 orders of magnitude smaller. It therefore seems reasonable to neglect the friction component and to set $c_{f,p} = c_{f,s} = 0$.

$$C_f = \frac{0.074}{Re_c^{1/5}} \tag{6.6}$$

[1]The Reynolds number is obtained according to $\frac{\rho_\infty V_\infty c_{diff.}}{\mu_\infty} = \frac{1.19 \cdot 10 \cdot 0.9}{1.79 \times 10^{-5}}$

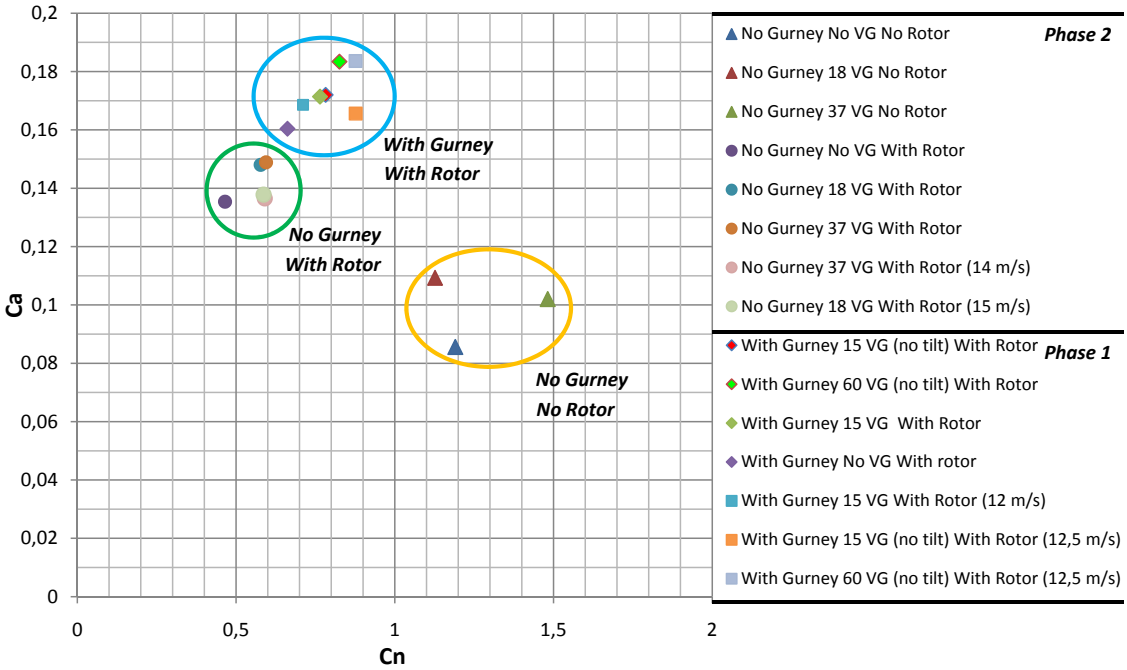

Figure 6.7: Cn v.s Ca (phase 1 and 2) Unless stated otherwise, wind speed =10m/s with the VG's tilted 50° downstream

Figure 6.7 shows the results of the surface pressure integration obtained for various configurations. As expected, the axial force components are significantly higher when a Gurney flap is applied. Furthermore, it becomes apparent that in terms of the radial force component the gurney flap configuration out performs the VG configuration. Table 6.2 shows the axial and radial force coefficients relative to the bare configuration. It can be seen that the Gurney flap configuration, in terms of radial force component as compared to the bare configuration, outperforms the 37 VG configuration by about 18%. The axial force component of the Gurney flap configuration however is nearly 9% higher. Thus, if the radial force component is compared to the projected area perpendicular to free stream, then it is found that the 37 VG configuration out performs the Gurney flap configuration with about 8.5%[2]. Apparently, in terms of the radial force component versus projected area, the vortex generators are the more efficient augmentation device. Thus, suggesting that enhanced flow mixing behind the exit plane of the diffuser does indeed take place. Table 6.3 supports this finding in terms of power augmentation. It can be seen that the Gurney flap configuration only out performs the 37 Vg configuration by about 4% relative to the bare configuration. When this percentage is related to the projected area, then it can be found that the 37 VG configuration outperforms the Gurney flap by about 3%.

[2]This precentage is obtained by multiplying the percental increase of the 37 VG configuration with the projected surface quotient

[2]The projected area is defined as the total area of the augmentation device perpendicular to the freestreamflow

Table 6.2: Test results integrated wall pressures at 10 m/s and r_{max}

Configuration	C_n	C_a	$C_n/C_{n_{bare}}$	$C_a/C_{a_{bare}}$	$A_{proj.}{}^2$
No rotor (bare)	1.1906	0.0856	-	-	-
0 Vg's (bare)	0.4653	0.1354	1.000	1.000	0 m^2
18 Vg's	0.5775	0.1480	1.241	1.093	0.0607 m^2
37 Vg's	0.5945	0.1489	1.278	1.100	0.1247 m^2
Gurney Flap	0.6620	0.1604	1.423	1.185	0.2564 m^2

6.3 Axial force measurements

Table 6.3 shows some force measurements on the DAWT obtained at 10 m/s where $F_{t_{NR}}$ is the total force on the DAWT without rotor. The variables F_t , F_r and F_A are the total axial force, rotor axial force and integrated axial pressure force of the DAWT operating at maximum performance respectively. Furthermore, the ratio τ is the thrust ratio and is defined as $\tau = \frac{F_r}{F_t}$ [1]. From table 6.3 it becomes clear that there is a discrepancy between the axial diffuser force as deduced from the force balance system and surface pressure distribution. The discrepancy, ranging from 10 to 20 N, can be partially explained by the wake emanating from the supporting trusses. From visual inspections with wool tufts, it was shown that a significant expanding wake behind the trusses was present with an operating rotor. This expanding wake suggests a super critical Reynolds number and consequently a high drag coefficient. It was found from experimental data on cylinders that a C_d of 1.2 is a reasonable approximation [33]. If it is assumed that the velocity right behind the rotor does not dramatically decrease, then the total drag of the trusses can be approximated[3] at about 10 N. It can however be expected that this value could be slightly higher due to interaction effects close to the diffuser wall and rotor center body. Of course, the rotor centerbody causes drag as well and this is found to be about C_d=0.6 [20]. However, it is suspected that due to the diffusive and swirling flow inside the diffuser, the actual C_d value for the centerbody may be considerably higher than 0.6.

Table 6.3: Absolute force test results at 10 m/s and r_{max} (phase 2)

Configuration	$F_{t_{NR}}$ [N]	F_t [N]	F_r [N]	F_t- F_r [N]	F_A [N]	r [-]	τ
0 Vg's (bare)	32.2	91.9	38	53.9	44.85	0.45	0.414
18 Vg's	40.5	99	32	67	48.79	0.46	0.323
37 Vg's	44	101	32	69	49.17	0.48	0.316
Gurney Flap	-	-	-	-	53.07	0.50	-

The values in table 6.3 also indicate an increasing drag force on the diffuser with an increasing amount of VG installed at the trailing edge. If the total force measurements with and without an operating rotor are compared, it can be observed that the axial forces increase with about 57 to 59.7 Newtons when an operating rotor is present. The ratio

[3]The diameter of the support trusses are 5 cm and length is set to 0.75m. Thus, the projected surface is A=4·0.75·0.05=0.15m^2. Using $D = \frac{1}{2}\rho V^2 C_d A$ with $V \approx V_\infty$

$\frac{Ft}{Ft_{NR}}$ decreases with progresively more VG's from 2.85 for the bare configuration to 2.30 for the 37 VG's configuration, thus confirming the decreasing rotor loading as indicated by the rotor force measurements.

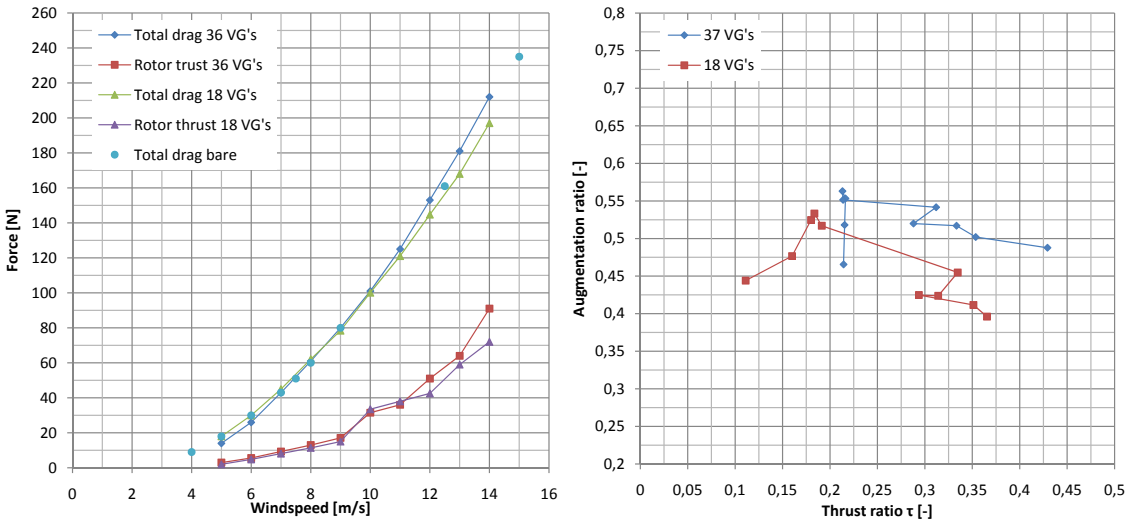

(a) Absolute forces on rotor and the complete DAWT system

(b) Thrust ratio versus augmentation factor

Figure 6.8: Some force measurements of thest phase 2

Figure 6.8a shows the absolute forces on diffuser and rotor over a velocity range of 5 to 14 m/s . Figure 6.8b shows the ratio τ versus the corresponding augmentation factor r as given by equation 6.1. From figure 6.8 it is observed that a high rotor thrust does not necessarily lead to higher augmentation factors. This behavior is supported by table 6.3 and figure D.1 where a similar result can be found for the various VG configurations. However, it has to be noted that the lower value of τ corresponds to the lower velocity region (see figure D.1) where the accuracy of thrust measurements on the rotor is questionable due to the static friction effects of the roller bearing in the traversing sledge. From figure 6.8 and table 6.3 it can be concluded that the axial rotor thrust is around $\frac{1}{3}$ of F_t and that axial force on the diffuser with augmentation devices is about $\frac{2}{3}$ of F_t. It can also be observed that the maximum augmentation factor r_{max} is obtained for relatively low thrust ratio's of around τ=0.2, suggesting a non-optimal rotor geometry and/or considerable parasitic drag inside the diffuser.

6.4 Pressure probe measurements

From the 5 hole pressure probe readings it was possible to deduce[4] the slip angles, angles of attack and total velocities. The angle measurements were unfortunately not very accurate as can be seen in figures D.2, D.3 and D.4.The total velocity measurements deduced from the 5 pressure readings have slightly more accuracy, although it has to be noted that most measurements that have been performed under the same circumstances in a consecutive

[4]Appendix A gives a concise description of the procedures involved

order still show rather large velocity differences of about 10%. Another uncertainty caused in the measurements is the fact that the 5 hole pressure probe was slightly closer to the rotor in some cases. Because of these uncertanties one has to bear in mind that these results can only be used as an indication. Figure 6.9 shows the normalized total velocity profiles between the diffuser wall and center body obtained in the same measurement run as the data in figure 6.4a to 6.4a. A consistent trend between the rotor and non rotor cases is that the average total velocity reduces by approximately 26-27% when an operating rotor is present. Another trend which is clearly seen in figure 6.9, is that the highest velocities are measured in close vicinity of the diffuser wall. Measurements at 10 cm behind the diffuser exit plane indicate an average decrease in total velocity of about 32-37% [5] as can be seen in figure 6.10. Within a radius of about 0.35 meters from the rotor centerline no velocities could be derived since the pressure readings fell outside the calibration data suggesting a rather large wake. This result corresponds with a tuft visualization which indicated significant backflow. Also, in figure 6.10 the influence of the diffuser is clearly visible as a velocity deficit. A close inspection in this area does suggest that there is a slight velocity increase near the trailing edge suction side accompanied with a small decrease on the pressure side when vortex generators are applied. With some caution, this could indicate some momentum transfer from the free stream to the rotor wake.

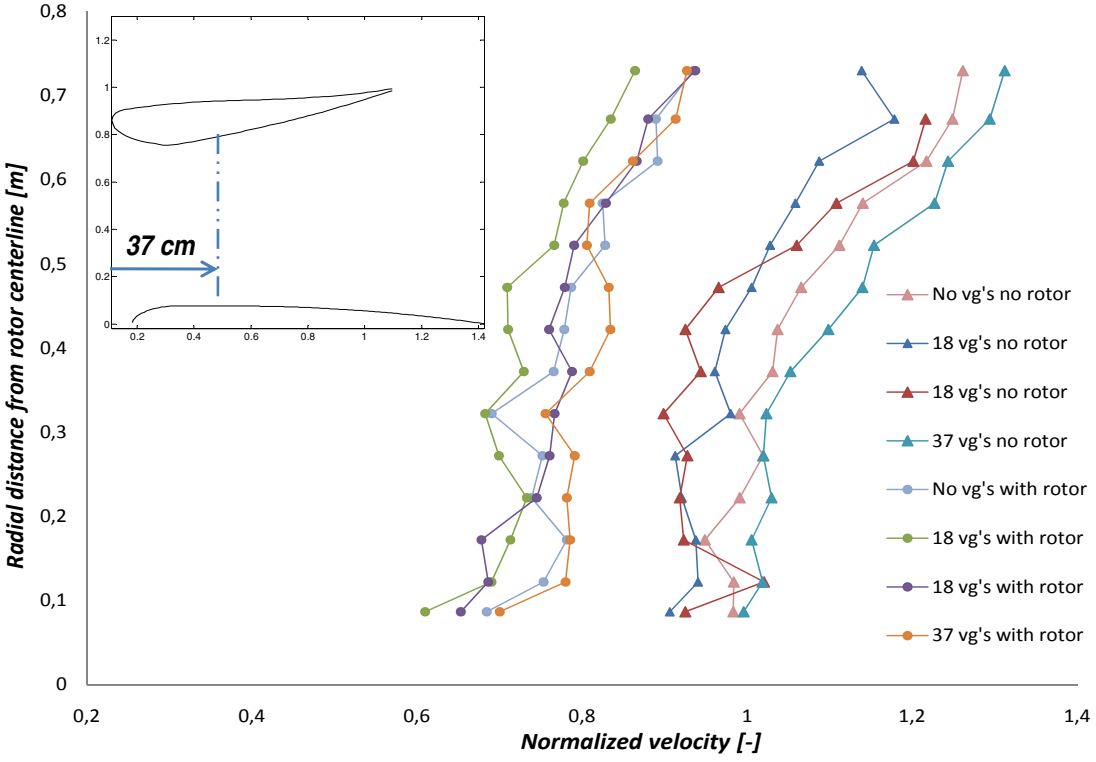

Figure 6.9: Dimensionless velocity profile vs radius from centerline (phase 2)

Table 6.4[6] summarizes some more results in terms of mass flow, average velocities and

[5] With respect to the no rotor case measured velocities in the throat, 7 cm behind the rotor plane
[6] The values in table 6.4 corresponds to the figure 6.4a to 6.6b

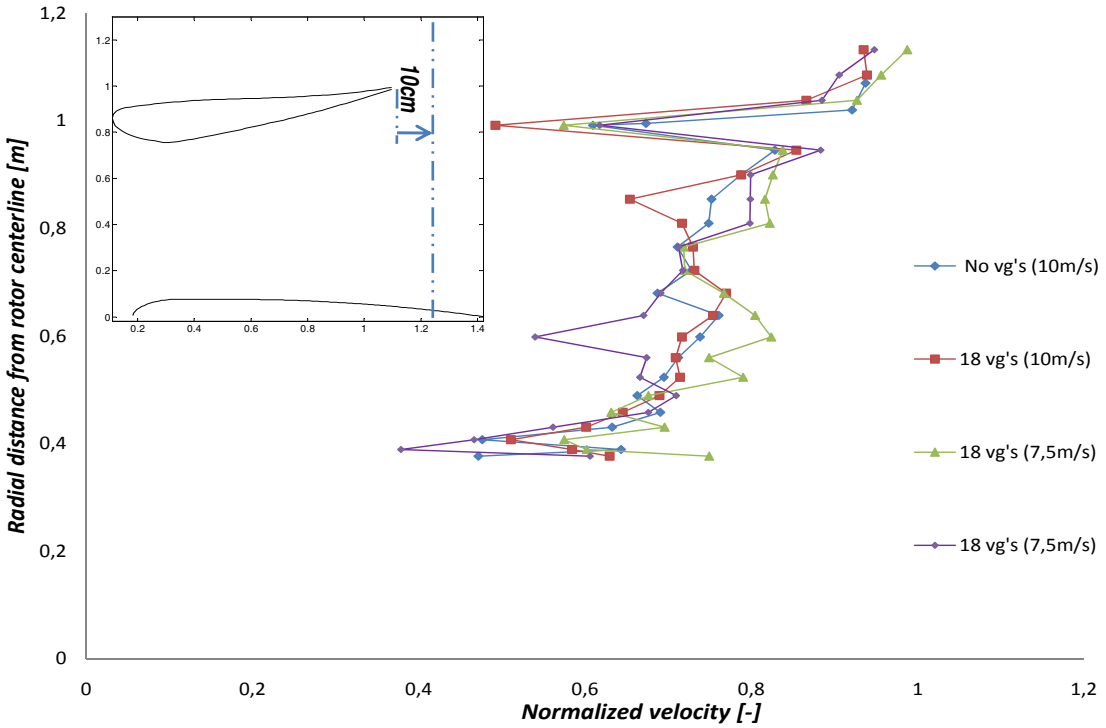

Figure 6.10: Dimensionless velocity profile vs radius from centerline (phase 2 with rotor)

average total pressures behind the rotor and diffuser exit plane. If the 18 VG configuration is discarded, it can be seen that the general trend behind the rotor is an increasing average velocity and mass flux with increasing augmentation devices. The static pressures, as expected , decrease with more augmentation devices. From the table 6.4 it also becomes clear that the differences are small and that there are some inconsistencies. Especially between the mass flow quantities behind the rotor and diffuser exit plane as indicted in table 6.4. It seems more mass is flowing out from the diffuser exit plane then is flowing in right behind the rotor plane. If the out flow plane at the diffuser exit is corrected for the wake emanating from the center body ($r_{diffexit}$ = 1- 0.4), then it is found that the average mass flow values corresponds better with the mass flow values right behind the rotor.

6.4.1 Some pressure probe considerations

The total average pressure coefficient differences between the exit plane and behind the rotor, as shown in table 6.4, are harder to understand. They should approximately be the same according to Bernoulli's equation[7] [8]. In figure D.2a and D.3a one can find some radial pressure graphs behind the rotor and diffuser exit plane respectively. The c_{p_t}

[7]The total pressure coefficients are calculated with equations A.6 and 4.7

[8]Like mentioned before, it was again found that the static pressure at the exit plane of the windtunnel nozzle was approximately the same as the ambient reference pressure in the open test section

Table 6.4: DAWT mass flow results for different VG configurations at 10 m/s and $\rho = 1.2$ (phase 2)

Configuration	$V_{ave.}$ [−]	$Va_{ave.}$ [11] [−]	$\dot{m}_{ave.}$ [12] $[\frac{kg}{sec}]$	$\dot{m}_{ann.}$ $[\frac{kg}{sec}]$	c_{p_t} [13] [-]	c_{p_s} [-]
No rotor		A=1.81 m^2				
Bare	1.073	1.067	23.15	24.20	0.626	-0.537
18 Vg's[14]	1.002	0.994	21.57	22.44	0.566	-0.44517
37 Vg's	1.115	1.107	24.03	25.17	0.594	-0.6638
With rotor	7 cm	behind	rotor	plane		
Bare	0.793	0.763	16.55	17.45	0.267	-0.368
18 Vg's	0.737	0.704	15.27	16.19	0.2515	-0.296
37 Vg's	0.8133	0.783	17.00	17.76	0.228	-0.436
With rotor	10 cm	behind A=3.14	diffuser	exit plane		
Bare	0.681	0.663	24.98	19.77	0.324	-0.146
18 Vg's	0.684	0.668	25.08	20.53	0.324	-0.148

values in the cases without a rotor are also too low. The average total pressure coefficient derived from velocity measurements done at 2 meter in front of the wind tunnel exit plane give a better result of $c_{p_t} = 0.92$ (see figure D.4a). The stagnation pressure measured on the diffuser's leading edge also seems to capture the proper value of $c_{p_t} \approx 1$ as shown in figures 6.4 and 6.6. Close inspection of the c_p curves shown in figures 6.4 and 6.6 do suggest a larger velocity near the wall than is deduced form the probe measurements presented in figure 6.9. On the other hand, the normalized velocities, as shown figure 6.10 (and the total pressure profile in figure D.3a), nearly attains unity as the probe passes the trailing edge. Thus, the logical origins for these c_{p_t} discrepancies is either a significant static pressure decrease inside the diffuser due to nozzle blockage or a mispositioning of the pressure probe. Although great care has been taken to avoid wake interferences from the support trusses and center body with positioning the probe, it would explain the discrepancies in the total pressure distributions. Furthermore, it was found through trial and error that the reference pressure, in this case the atmopsheric pressure in the tunnel as explained in appendix A, also has it's impact on the total pressure and velocities in absolute sense. However, changing the reference pressure does not influence the radial pressure distributions and therefore does not explain the radial differences for the case no rotor is present inside the diffuser[9].

[12]The annular massflux is obtained by multiplying the locally measured velocity with the corresponding sectional annular

[13]The total pressure coefficient is the total pressure measured with the 5 hole pressure probe devided by the dynamic free stream pressure

[14]The vortex generators are tilted 50° downstream pointing outside as depicted in figure 5.1a

[9]Changing the reference pressure does not change the absolute value of the velocities and angles as can be observed from the equations presented in appendix A

Chapter 7

Model Validation and Verification

The present chapter is concerned with the verification and validation of the vorticity code, as implemented in MATLAB according to the mathematical model as described in chapter 4. A verification is done in the first section by comparing the vorticity code to verified and validated codes. The validation will proceed in the second section where the model results are compared to the wind tunnel test results as presented in chapter 6. The third section considers the CFD code of NLR with respect to the measurement results of chapter 6.

7.1 Verification

The present section seeks to verify the vorticity code by comparing the results with *X*Foil and the CFD code of NLR. Section 7.1.1 compares the code in 2D with *X*Foil. A 3D verification of the diffuser without and with a rotor is made in sections 7.1.3 and 7.1.4 respectively. In both comparisons use is being made of selected CFD results as presented by NLR [42][41]. Also, some effort is made in assessing the behavior of the code by introducing small adaptations.

7.1.1 A 2D comparison with *X*Foil

In order to determine the accuracy of the vorticity code, it is necessary to investigate how it behaves in only two dimensions. The scheme given in chapter 4 is equally well applicable to the 2 dimensional case as the 3 dimensional case. The only difference is that the ring vortices are replaced by point vortices. Figure 7.1 shows a picture of the present code with the well established *X*foil [1] code. Both codes are based on a simple linear vorticity stream function panel method with an explicit Kutta trailing edge condition. The difference between the two is that *X*foil models the trailing edge base thickness

[1] *X*foil has been written by Mark Drela and is recognized throughout aviation industry as a reliable code for the predictions of airfoil performance characteristics. The code is open source and the first version dates back to 1986. The present version used is *X*foil 6.9 which is last updated on the 30^{th} nov. 2001

with a source panel. Also, the panel method of *X*foil is a high order panel method where the present code is not. Furthermore, *X*foil also incorporates the Karman-Tsien compressibility correction. Although the present code does not have these features, it can be seen in figure 7.1a that there is a slight under approximation, but never the less a reasonable match between the two codes. A comparison with the viscous case, as depicted in figure 7.1b, shows that there is a slight over approximation. It can be concluded from figures 7.1a and 7.1b that for the inviscid case the code seems to be reasonably reliable. However, for the inviscid case, especially at higher angles of attack, the code does not perform so well. This can be explained by the fact that *X*foil predicts a separated region at the trailing edge where the present code does not.

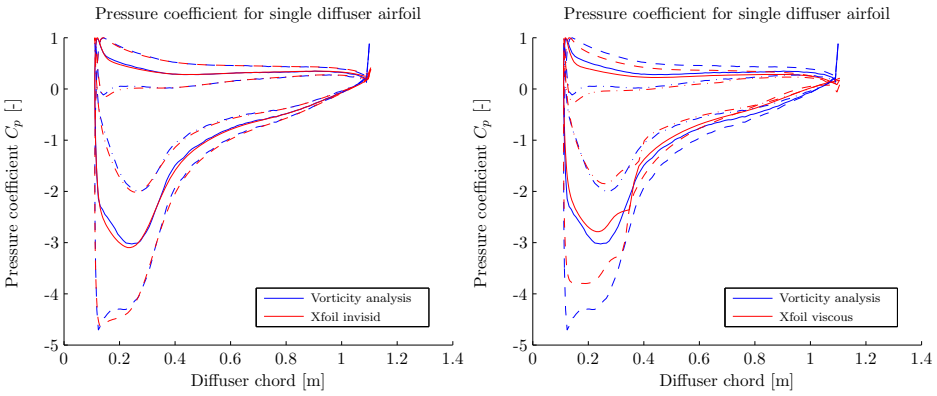

(a) inviscid case (b) viscous case

Figure 7.1: *X*Foil (140 panels) - vorticity code (120 panels) comparison: Pressure curves at various angles of attack; $(-)\alpha = 0°(--)\alpha = -5°(-.)\alpha = 5°$

*X*Foil results presented in figure 7.1 are obtained with 140 panels where the vorticity code employs 120 panels. Figure 7.2 shows 2 figures where the amount of panels is increased from 40 upto 1000 panels. As can be seen, the vorticity code nicely converges to a smooth line. However, beyond 200 panels the code starts to show some roughness in the pressure distributions as can be observed in figure 7.2b.

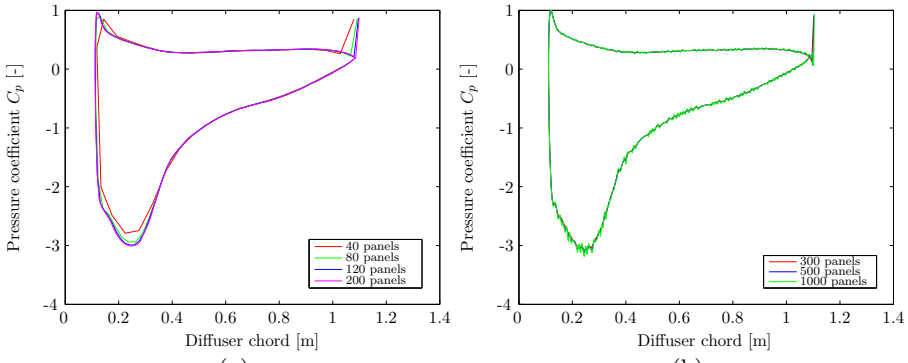

(a) (b)

Figure 7.2: numerical stability with decreasing panel size

7.1.2 A 3D modeling of the diffuser

It was found that the 3D vorticity code behaves in a similar fashion to an increasing amount of panels as shown in figure 7.2 of the previous section for the 2D case. The pressure distribution over the diffuser wall however, is quite sensitive to the radius of the throat and apex angle of the diffuser. Figure 7.3 demonstrates the behavior. Increasing the apex angle leads to higher pressure coefficients and corresponding velocities in the throat. Decreasing the apex angle has the opposite effect. The same general behaviour is found if the diffuser throat radius is increased or decreased as can be observed in figure 7.3a and 7.3b.

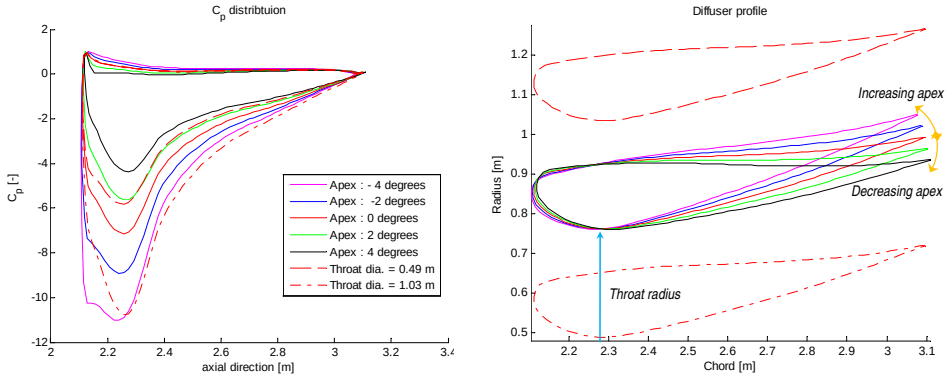

(a) Pressure profiles (b) Diffuser profiles

Figure 7.3: Vorticity code behavior with varying apex angles and throat diameter

A diffuser geometry adaptation

The diffuser employed during the experiments in the *OJF* did not have a smooth leading edge to noise damper transition as explained in section 6.2. It was suspected that the protruding noise damper rim did have a significant influence on the diffuser wall pressure distribution. If the empty diffuser geometry is adapted to meet the diffuser shape used in the experiments, then it is found that the voriticty code is more sensitive to amount of panels used to model the diffuser. The diffuser profile presented in figure 7.4a is changed by introducing a small bump of 0.7 cm close to leading edge. As can be found in figure 7.4b, increasing the number of panels beyond 120 results in a higher pressure spike at 0.3 chord length.

7.1.3 A 3D comparison with CFD (empty diffuser)

Figure 7.5 shows a velocity comparison in the throat of the empty diffuser between the 3D vorticity code and CFD results of NLR [42]. The CFD code makes use of a $\kappa - \epsilon$ turbulence model to capture viscous effects. The diffuser profiles shown in figure 7.5a and 7.5c are not exactly identical. The CFD calculation performed by NLR used diffuser profile 'design 2' of phase 1 [42]. The computational result shown in figure 7.5c uses the final diffuser airfoil shape as given in appendix C, where the throat is decreased in order

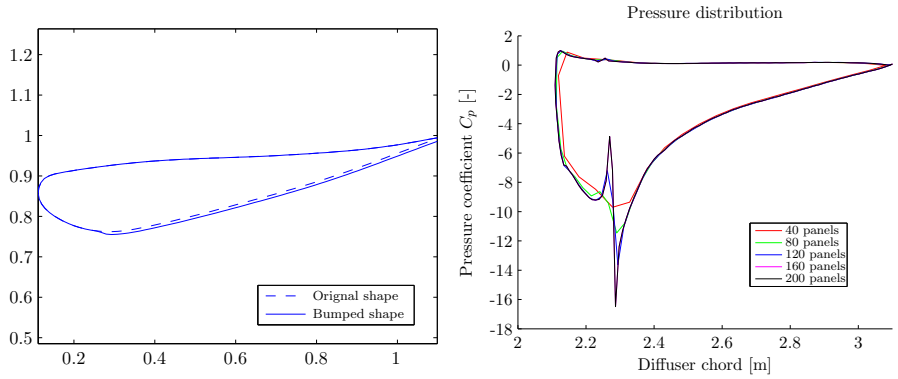

(a) Diffuser cross sectional shape (b) Pressure distribution

Figure 7.4: Diffuser adaptation

to match the throat diameter of the profile of figure 7.5a. One obvious difference between the two is that the viscous CFD result predicts a separated area on the suction side towards the trailing edge where the inviscid vorticity code does not. Figure 7.5b shows the local velocity in the diffuser throat. The vorticity code predicts up to 20% higher velocities in the rotor plane than the CFD result indicate. A better match is obtained if the diffuser profile thickness is reduced by 15% as shown in figure 7.5b. A same result can be obtained if the apex angle is reduced by 2°.

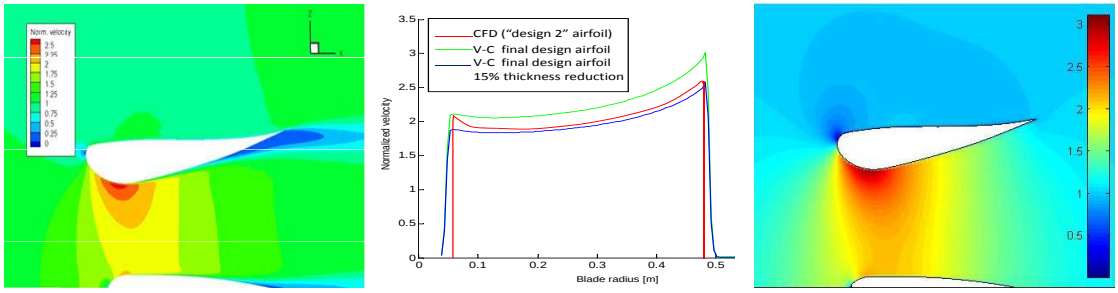

(a) Normalized velocity field, CFD result NLR [41]

(b) Velocity distribution in rotor plane at 0.3 m from the leading edge

(c) Normalized velocity field, vorticity code (V-C) MATLAB

Figure 7.5: CFD - Vorticity code comparison with a throat radius of 0.48 m

7.1.4 A 3D comparison with CFD (DAWT)

The numerical modeling of the rotor is described in section 4.2 and in appendix C one can find the airfoil polar curve used to model the blade. The blade chord and twist distributions can also be found in appendix C. The controlling mechanism in the code, apart from the operational condition V_∞, Ω and θ, is the wake helical propagation velocity V_W as introduced in section 4.2. The helical pitch is not the same for every blade section and is obtained by calculating a new helical pitch and corresponding wake geometry for every iteration. The helical pitch is then multiplied by the wake propagation velocity V_W.

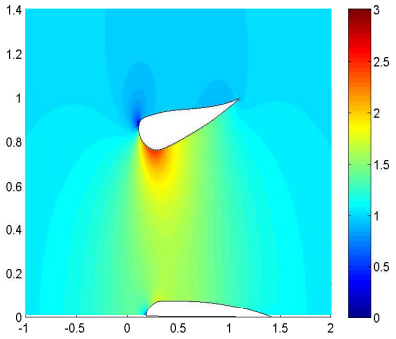

(a) $V_W = 0.7V_\infty$

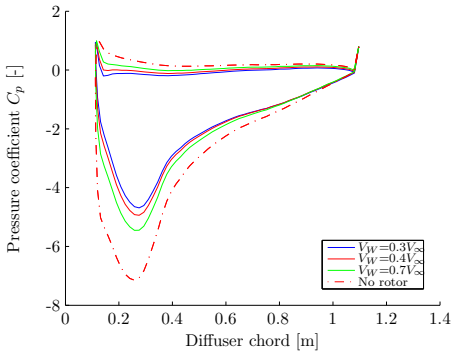

(b) Pressure distributions

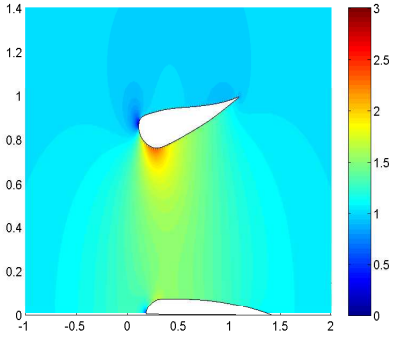

(c) $V_W = 0.3V_\infty$

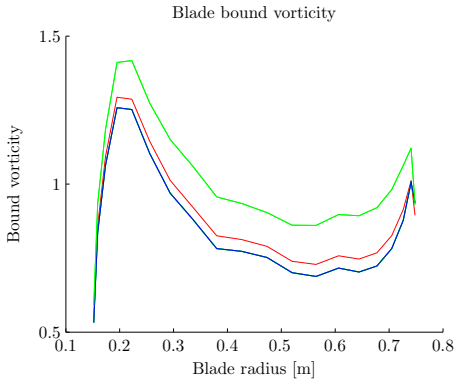

(d) Blade bound vorticity

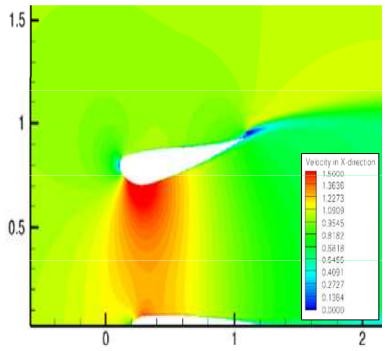

(e) CFD result with actuator disk [42]

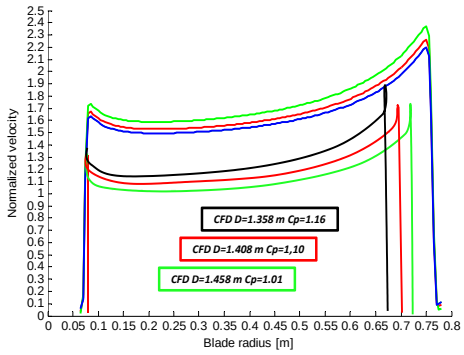

(f) Velocity profile comparison in rotor plane at 0.3 m behind leading edge

Figure 7.6: Diffuser *with* operating rotor at 10 m/s and 70 rad/sec ,No bump in diffuser profile, pitch=17° and $\alpha = 0°$,20 blade sections, 240 panels diffuser and centerbody

Obviously, the question whether the code converges depends on whether the interpolation scheme in the polar data stays within its range. This fully depends on the velocities induced by the wake and shroud in the rotor plane and consequently on the wake geometry and thus the wake propagation velocity V_W.
The behavior of the vorticity code with an operating rotor is investigated at V_∞=10 m/s.

Furthermore, the amount of panels on the center body and diffuser are 120 each. The blade is divided by means of a cosine distribution into 20 blade sections . It was found that the code did converge as long as the wake propagation velocity stayed above V_W=0.3 V_∞. The code becomes unstable for values below V_W=0.3V_∞. This instability manifests itself at the blade root section as a diverging helical pitch.

Config.	Power [W]	T_{rotor} [N]	C_n [-]	C_a [-]	Torque [Nm]
CFD (Cp=1.16 D=1.358)[42]	1080	-	-	-	-
$V_W = 0.7V_\infty$	1266.50	34.541	2.3100	0.0812	18.092
$V_W = 0.4V_\infty$	1050.90	29.742	2.0419	0.1119	15.013
$V_W = 0.3V_\infty$	994.31	28.474	1.8939	0.1422	14.204

Table 7.1: All computation corresponding to figure 7.6 and are performed with 20 blade sections at a pitch of 17°, $\alpha = 0$, no bump at V_∞=10m/s and Ω=70 rad/sec

Figure 7.6 shows a computation in which the wake velocity is set at 0.7 V_∞ ,0.4 V_∞ and 0.3 V_∞ respectively. The influence of the rotor causes the pressure curve to shift to higher pressure values with decreasing V_W as can be seen in figure 7.6b. The bound vorticity distribution decreases with a decreasing V_W (see figure 7.6d). Another corresponding observation from figure 7.6a and 7.6c, is that the overall velocity distribution in and around the DAWT decreases as V_W is decreased.

Table 7.1 summarizes some DAWT performance characteristics corresponding to figure 7.6. The general observed trend in table 7.1 is, apart from the axial force coefficient, a decrease in power, torque, rotor thrust and normal force coefficient with a decreasing V_W. A comparison with the CFD results of NLR, where the rotor is modeled as an actuator disk (see figure 7.6e), shows that the vorticity code over estimates the velocity distribution in the throat of the diffuser by about 50%. The total power does have a reasonable match with the CFD code, although it has to be noted that the throat diameters in both codes do not exactly match. Furthermore, the diffuser in the CFD code employs a Gurney flap where the vorticity code does not. To conclude, it was found that the vorticity code converges quicker when the pitch angle and rotor rotation speed is adapted to lower values. Furthermore, the introduction of the bump has a negative effect in terms of convergence. This is not surprising because the bump adds a discontinuity in the diffuser profile.

7.2 Validation

The validation of the vorticity code proceeds by comparing the code to the measurement results presented in chapter 6. The emphasis during the comparison is put on the wall pressure distributions and flow velocities 7 cm behind the rotor plane.

7.2.1 A comparison with experimental results (empty diffuser)

As already noted in section 6.2, the spike in the pressure distribution near 0.27 chord position is caused by the protruding noise damper rim. If the cross sectional diffuser

shape is adapted with a little bump of 0.7 cm on the suction side at 0.27 chord position (see figure 7.4a), it is found that shape of the pressure distribution has slightly more resemblance with the measured case (figure 7.7a), although still heavily over estimated. If a local flow angle of $\alpha = 7.2$ is adapted[2], a better estimate can be obtained as shown in figure 7.7b. A comparison with table 6.2 and the obtained values of $C_n = 1.1834$ and $C_a = 0.1421$[3], shows that the normal force coefficient has a reasonably accurate approximation where the axial force coefficient shows an over approximation of 66 %. Figure 7.7d confirms the radial velocity measurement 7 cm behind the rotor plane, where the tendency of the velocity to speed up towards the diffuser wall is reasonably well captured. The magnitude however, is more than 30% to high.

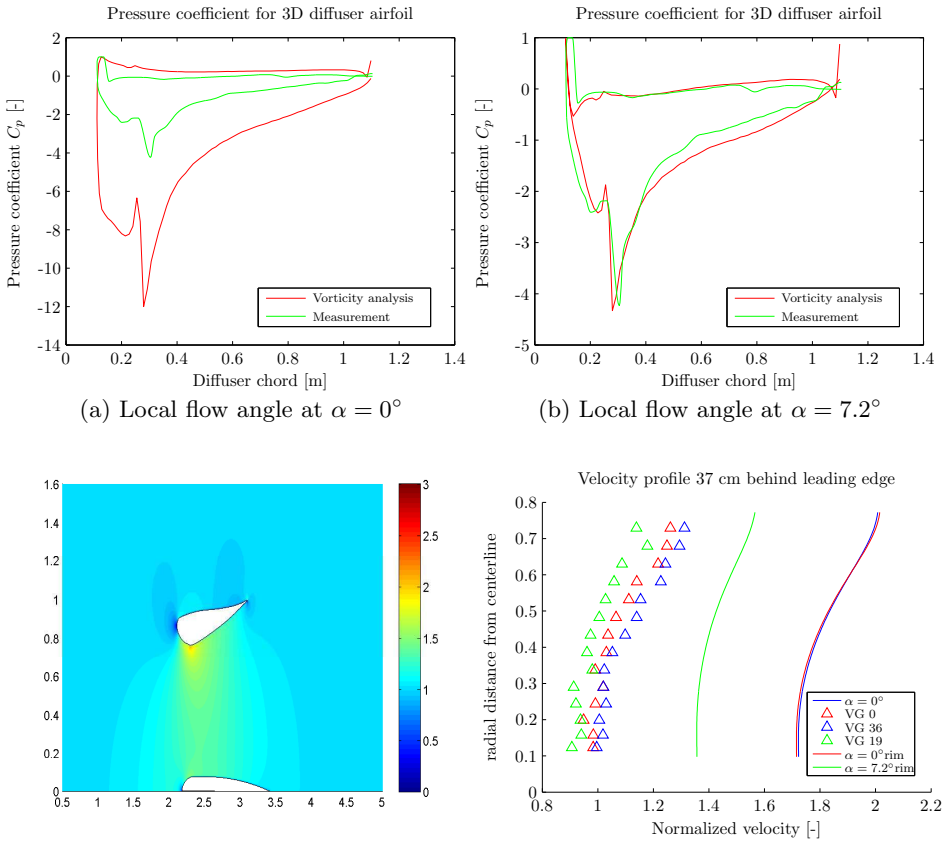

(a) Local flow angle at $\alpha = 0°$

(b) Local flow angle at $\alpha = 7.2°$

(c) Velocity field at $\alpha = 7.2°$ with bump

(d) Velocity profile 37 cm behind leading edge

Figure 7.7: 3d code comparison with measurement 10 m/s without rotor

[2]The angle of attack is introduced by multiplying the U_t and V_t components in equation 4.3.1 with $\cos\alpha$ and $\sin\alpha$ respectively

[3]These results where obtained by integrating the pressure coefficients plotted in figure 7.7b according to equation 6.4 and 6.5

7.2.2 A comparison with experimental results (DAWT)

Figure 7.8a compares the pressure distributions of figure 7.6b to the experimental results. The first observation in figure 7.8a is that the solution of the vorticity code also over estimates the rotor case. However, the influence of the rotor is reasonably well captured.

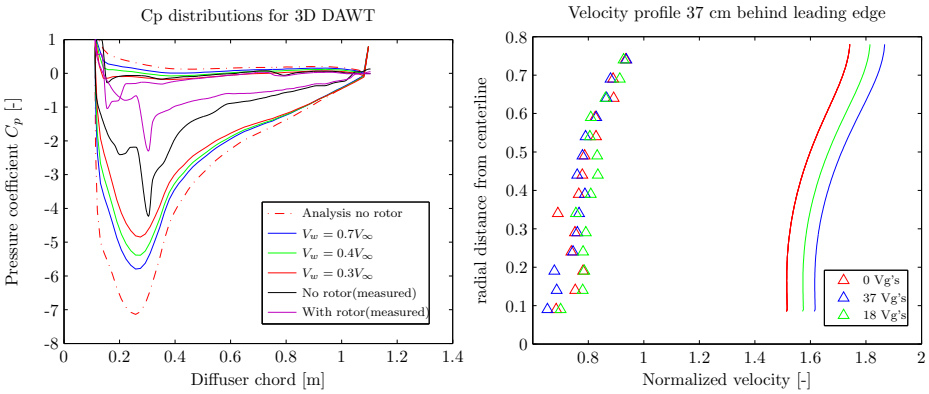

(a) Pressure distributions

(b) Velocity profile 37cm behind leading edge

Figure 7.8: 3D vorticity code comparison (α=0°; 30 blade section; 240 diffuser and center-body panels) with experimental result at 10 m/s with rotor operating at Ω=80 rpm at 17°

It can be seen in figure 7.8a that the introduction of a rotor causes the pressure curve to shift to higher pressures values like the measurements also indicate. The ratio of the peak pressures of the rotor and non rotor cases are however not the same. The measurements indicate 46 % decrease in peak pressure when a rotor is installed where the computation indicates only a 33 % decrease with $V_W = 0.3V_\infty$. The velocities at 37 cm behind the leading edge, as can be seen in figure 7.8b, are also heavily over estimated. The behavior of an increasing velocity towards the diffuser wall does seem to correspond reasonably well with the measurement results. In terms of power, it can be found from tables 7.1 and 7.2 that the model also heavily over estimates the power. If the calculated power is corrected for generator and inverter losses[4] it is found that the power is still nearly twice as high as the measured power. It is also observed in tables 7.1 and 7.2 that the torque is more than a factor two too high while the rotor thrust is under estimated.

If the effect of the noise damper rim is incorporated and the effective angle of attack is set at $\alpha = 7.2$, as done in the previous section, it is found that the pressure and velocity distributions shown in figures 7.9a and 7.9c respectively do become better as compared to the measurement results. A quick comparison between the pressure distributions shown in figure 7.9c, reveals that the solution is quite sensitive to the wake propagation velocity V_W. If the wake propagation velocity is decreased, it is observed that the absolute pressure peak on the pressure side increases while on the suction side decreases. Table 7.2 summerizes the results corresponding to figure 7.9. The values of the normal and axial force coefficients are in the right order of magnitude, but still too high. The power, torque and rotor thrust are in this case under estimated. Solutions with wake velocities lower than $0.4V_\infty$ do not

[4]The inverter and generator losses are in this comparison is set at 20%.

converge. This is probably caused by the introduction of the bump near the rotor plane. The bound vorticity jumps at 0.2 and 0.4 chord length are caused by the snags in the blade twist distributions at 0.2 and 0.4 chord length respectively (see figure C.1a).

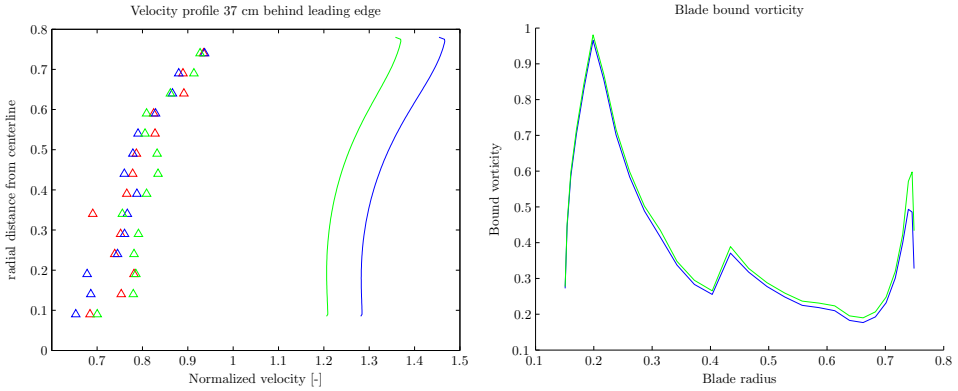

(a) Velocity comparison (b) Blade bound vorticity

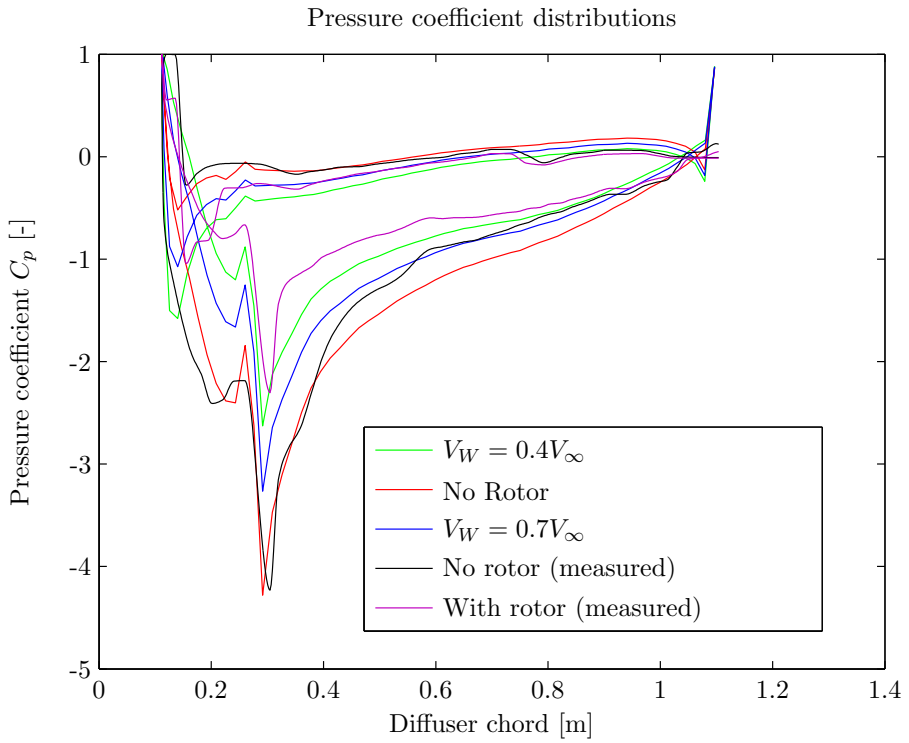

(c) Pressure distributions

Figure 7.9: 3d code comparison with measurement at V_∞ 10 m/s ,with rotor at α=7.2° and bump, Ω=80rpm,30 blade sections

To conclude, the behavior of the DAWT seems to be captured reasonably well, although heavily over estimated. It is expected that by introducing a proper wake geometry better results could be obtained. The application of the angle of attack α is perhaps necessary because the used coordinates file in the vorticity code does not exactly resemble the actual DAWT shape tested in the wind tunnel.

Config.	Power [W]	T_{rotor} [N]	C_n [-]	C_a [-]	Torque [-]
measurement (bare)	490	37.6	0.4186	0.0837	6.12
$V_W = 0.4V_\infty$	439	12.12	0.7835	0.1213	5.49
$V_W = 0.7V_\infty$	467	12.95	0.4644	0.0910	5.85

Table 7.2: Values corresponding to figure 7.9 at Ω=80rad/sec

7.3 A CFD-experimental result comparison

A comparison with the measurement results depicted in figure 7.9a and CFD velocity fields as shown in figure 7.6e and 7.6f, reveals that the CFD calculations over estimate the local velocity at the actuator disk by an average of 50%. However, *NLR* also performed a full 3D DAWT computation with a grid of 16 million points. The 3 rotating blades of the DAWT were simulated as shown in appendix C. Figure 7.10a and 7.10b shows the computed velocity fields. If these figures are compared to the measured velocity distributions inside the diffuser, as depicted in figure 6.9, it is observed that the velocity field calculated by CFD is heavily over estimated by about 100 %. If the calculated power is matched to the measured power at 10 m/s, it is observed in table 7.3 that the order of magnitude of the power is considerably better and only deviates with about 4%. The RPM and torque however, does not match the reality. To conclude, it has to be noted that the CFD calculations where performed with a Gurney flap while the measurements correspond to the case without a Gurney flap. It can therefore be expected that the resemblance between the CFD velocity calculations and velocity measurements are in reality better due to a better performance of the DAWT.

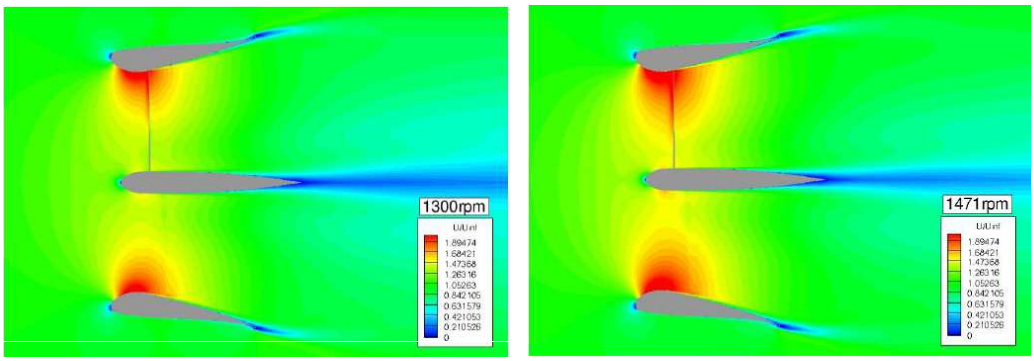

(a) Normalized velocity field at 10 m/s and 137 rad/sec [42]

(b) Normalized velocity field at 10 m/s and 155 rad/sec [42]

Figure 7.10: CFD calculations by *NLR* at 10 m/s with full rotor at 0.3 m.

RPM $[rad/sec]$	Power $[W]$	Torque $[Nm]$
Measurement with Gurney		
75	531	7.1
CFD		
137	545	4
155	246	1.6

Table 7.3: Values corresponding to figure 7.10a and 7.10a [42] at 10 m/s with Gurney flap

Chapter 8

Conclusions and Recommendations

The power augmentation potential of placing delta shaped vortex generators on the trailing edge of a diffuser augmented wind turbine has been investigated in the present thesis. The hypothesis that the vortex generators on the diffuser trailing edge cause a momentum transfer into the rotor wake and thus decrease the diffuser exit pressure and consequently increase the power output has been demonstrated, although the associated power increase is marginal. The first section summarizes the conclusions regarding the wind tunnel results and vorticity code, as implemented according to the mathematical model as discussed in 4. The second section is concerned with the recommendations for further development of the diffuser augmented wind turbine of Donqi Urban Windmill.

8.1 Conclusions

8.1.1 Power measurements

In terms of power, it was found that the VG's do increase the output although not as much as the Gurney flap. If the power increase of the VG and Gurney flap configuration are compared relative to the projected area of the respective augmentation device however, it is found that the VG configuration outperforms the Gurney flap configuration with about 4 %. A similar trend was found if the two configurations are compared in terms of the radial force component on the diffuser. The VG configuration outperforms the Gurney flap configuration with about 10% relative to the projected area. Compared to the bare configuration, the absolute power increase with 37 installed VG's is about 3-9%. Thus, the results do suggest that the vortex generator is a more effective augmentation device than, in this case a Gurney flap. From flow visualizations with tuffs, it was also seen that the vortex generator did induce stream wise vortices where the Gurney flap induced mostly normal vortices.

8.1.2 Pressure measurements

The pressure measurements around the diffuser perimeter did not show very pronounced changes with the VG configuration as compared to the bare configuration. The small differences in the pressure curves with progressively more VG's showed a trend of increasing absolute pressures coefficients on the suction side accompanied by decreasing absolute pressure coefficients on the pressure side. This suggests an enhanced swallowing capacity of the DAWT. However, caution is necessary if any conclusions from these observations are made. It might well be possible that measurement inaccuracies could be the perpetrator of these observations. Close inspection of the pressure distributions when a Gurney flap is present, reveals a more pronounced change in the pressure distributions. It can therefore be concluded that the static pressure measurements on the diffuser wall is probably not the most suitable approach to capture the influence and flow behavior of a VG equipped DAWT. Perhaps the stream wise vortices manifest themselves further downstream and thus effecting a larger area than the small region close to the diffuser wall. However, the static wall pressure measurements did show to be quite valuable in validating the mathematical model.

8.1.3 Force measurements

The force measurements performed on the rotor itself were not very accurate. The main reason for this, is that the generator suspended by sledge had to overcome a rather large static friction force. Concerning the measurements done on the total force balance, it has been found that the introduction of the VG's did increase the axial force by about 7-9 N on top of the 92 N for the bare case. When no rotor is present, it was found that the axial force is about 57 to 60 N smaller and amounts to about 32.2 to 44 N with progressively more VG's installed respectively. The force measurements are obtained at an indicted wind tunnel velocity of 10 m/s. It can also be deduced from these results that the rotor seems to operate under a lower rotor thrust when VG's are present at the trailing edge. The DAWT augmentation ratio r, seems to attain higher values when τ is kept around 0.2 to 0.25.

8.1.4 Velocity measurements

The velocity measurements performed with the pressure probe showed quite some inconsistencies, and are not very suitable to make any detailed conclusive remarks regarding the influence of the vortex generators on the flow field in and around the diffuser. A consistent trend found from the velocity measurements however, is that the presence of rotor decreases the flow through the diffuser in all considered cases with 26-27%. The flow decreases another 7-10 percent when it arrives at the exit plane with a operating rotor in place. In the case no rotor is present, the diffuser shows to speed up the flow close to the diffuser wall with about 30% starting about halfway from the center and progressively increasing towards the diffuser suction side wall.

8.1.5 Vorticity code

Although the vorticity code, as constructed from the mathematical model in chapter 4, was not accurate enough to make any conclusions regarding the flow behavior of the DAWT, let alone describe the influence of the vortex generators, it did show some resemblance with the real situation. A reasonably accurate diffuser pressure distribution was obtained with only minor adaptations. The general behavior of the rotor on the pressure distribution, an decreasing effective angle of attack, seems to be captured reasonably well although over approximated. Unfortunately the calculated velocity fields in and around the diffuser showed a rather poor resemblance with the real situation. Again, the velocity calculations over estimated the real case by about 100%. For the case without a rotor the velocity field in around the diffuser calculated by the model showed to have a better estimate although still with 30% overly optimistic. The radial velocity profiles did show a proper radial distribution; an increasing velocity as the diffuser wall is approached from the center. The power also proved to over estimate the real power with a factor of two. The CFD computations performed by *NLR* over approximated the flow velocities aswell. The power however only deviated with about 4%.

8.2 Recommendations

The following few sections give some recommendations for further DAWT development, future experiments and model development

8.2.1 DAWT improvement

It was found that rather large wakes emanated from the support trusses and center body. It can be expected that this causes a considerable blockage and thus a reduction in mass flow through the diffuser. It is therefore expected that a considerable improvement in performance can be obtained by streamlining these components of the DAWT. The pressure variation at the exit indicates also a sub-optimal energy extraction by the rotor from the flow. Ideally one would like to have an uniform velocity distribution at the diffuser's exit plane. The shape of the total velocity curve shown in figure 6.9 suggests a suboptimal twist distribution at the root section of the blade.

8.2.2 Experimental test setup

For future experiments it is recommended to measure flow field properties simultaneously as much as possible. If a pressure probe is used, like in the present investigation, it is important to ensure a very rigid support and to make the pressure tubes as short as possible (both issues could be considerably improved in the present set up) . Regarding the rotor axial force system, it is better to have the rotor suspended on thin blades equipped with strain gauges, like the total force balance, to eliminate any friction effects. Furthermore, properly calibrated load cells are the force measurement devices of choice.

8.2.3 Mathematical model

The singularity model proposed in chapter 4 could be improved by introducing a proper boundary layer on the diffuser wall to account for viscous effect. Perhaps a different wake geometry definitions, that also explicitly takes mass continuity into acount, could also lead to a better result.

References

[1] R.I. Lewis J.E. Williams M.A. Abdelghaffar. A Theory and Experimental Investigation of Ducted Wind Turbines. *Wind Engineering*, 1(2): 104 – 125, 1977.

[2] A. Von Betz. Energieumsetzungen in Venturidusen. *Die Naturwissenschaften*, 10: 160–164, 1929.

[3] L.Y. Jiang J. Yimer S. Manipurath I. Cmampbell W.E. Carscallen. Flow-field of an axisymmetric lobed mixer. *Journal of Thermal Science*, 13, 2003.

[4] J. Weber D. Kuchemann. *Aerodynamics of Propulsion*. McGraw-Hill New York, 1953.

[5] O. de Vries. *Fluid Dynamic Aspects of Wind Energy Conversion*. Number 243. AGARDograph, 1979.

[6] P.J. Richards D.G. Phillips and R.G.J. Flay. Cfd modelling and the development of the diffuser augmented wind turbine. *Wind and Structures*, 5(2$\tilde{4}$): 267–276, 2002.

[7] Horia Dumitrescu and Vladimir Cardos. Wind turbine aerodynamic performance by lifting line method. *International Journal of Rotating Machinery*, 4(3): 141 – 149, 1998.

[8] E.Dick. Power Limits of Wind Energy Concentrator Systems. *Wind Engineering*, 10(2), 1986.

[9] Enflo. `http://www.enflo-windtec.ch`.

[10] B.F.R. Ewald. *Wind Tunnel Wall Corrections*. Number 336. AGARDograph, 1998.

[11] C.A.J. Fletcher. Diffuser Augmented Wind Turbine Analysis. 7^{th} *Australasian Hydraulics and Fluid Mechanics Conference, Brisbane*, August 18-22 1980.

[12] C.A.J. Fletcher. Computional Analysis of Diffuser Augmented Wind Turbines. *Energy Con. & Mgmt*, 21: 175–183, 1981.

[13] FloDesign. `http://www.Flodesign.org`.

[14] J.K. Foss and K.B.M.Q Zaman. Large- and small scale vortical motions in a shear layer perturbed by tabs. *Journal of Fluid Mechanics*, 382: 307–329, 1999.

[15] GHCraft. `http://www.GHCraft.com`.

[16] B.L. Gilbert and K. M. Foreman. Fluid Dynamics of Diffuser-Augmented Wind Turbines. *Journal of Energy*, 2(6): 368 – 374, nov.-dec. 1978.

[17] B.L. Gilbert and K. M. Foreman. Experimental Demonstration of the Diffuser-Augmented Wind Turbine Concept. *Journal of Energy*, 3(4): 235 – 240, july-august 1979.

[18] W.J. Rainbird G.M. Lilley. A Preliminary Report on the Design and Performance of a Ducted Windmill. (Report 102), 1956.

[19] S.I. Green. *Fluid Vortices: Fluid meachanics and its applications– Chapter 11: Vortices in Aeropropulsion Systems*. Kluwer Academic Publishers, 1995.

[20] S.F. Hoerner. *Fluid Dynamic Drag*. Hoerner Fluid Dynamics, june 1965.

[21] U. Hutter. Optimum Wind-Energy Conversion Systems. *Ann. Rev. Fluid Mech.*, 9: 399–419, 1977.

[22] Yuji Ohya Takashi Karasudani Akira Sakurai Ken ichi Abe Masahiro Inoue. Development of a shrouded wind turbine with a flanged diffuser. *Journal of Wind Engineering and Industrial Aerodynamics*, 96: 524–539, 2008.

[23] O. Igra. Shrouds for Aerogenerators. *AIAA JOURNAL*, 14(10): 1481–1483, october 1976.

[24] O. Igra. Compact Shrouds for Wind Turbines. *Energy Conv.*, 16: 149–157, 1977.

[25] O. Igra. The Shrouded Aerogenerator. *Energy*, 2: 429 – 439, 1977.

[26] O. Igra. Research and Development for Shrouded Wind Turbines. *Energy Conv. & Mgmt*, 21: 13–48, 1981.

[27] O. Igra and K. Schulgasser. Design and Construction of a Pilot Plant for a Shrouded Wind Turbine. *Second Iinternational Symposium on Wind Energy Systems*, october 3rd-6th 1978.

[28] A. Plotkin J. Katz. *Low Speed Aerodynamcis*. Cambridge University Press, 2001.

[29] P. Jamieson. Beating Betz - Energy Extraction Limits in a Uniform Flow Field. *Garrad Hassan and Partners*, 2008.

[30] P. Jamieson. Generalized limits for energy extraction in a linear constant velocity flow field. *Wind Energ.*, 11: 445 – 457, 2008.

[31] A.L. Rogers J.F. Manwell, J.G. McGowan. *Wind Energy Explained; Theory, Design and Application*. Wiley, 2002.

[32] A.L. Loeffler Jr. Flow Field Analysis and Performance of Wind Turbines Employing Slotted Diffusers. *Transactions of the ASME: Journal of Solar Energy Engineering*, 103: 17 – 22, 1981.

[33] J.D. Anderson Jr. *Fundamentals of Aerodynamics*. McGraw-Hill third edition, 2001.

[34] H. Klomp. Turbine breekt door Betz-limiet. *Technisch Weekblad*, 10 dec. 2008.

[35] R.I. Lewis. *Vortex Element Methods for Fluid Dynamic Analysis of Engineering Systems*. Cambridge Engine Technology Series. Cambridge University Press, 1991.

[36] J.C. Lin. Review of research on low-profile vortex generators to control boundary-layer separation. *Progress in Aerospace Sciences*, 38: 389–420, 2002.

[37] Hiroshi Maekawa. Application of the vortex theory to highspeed horizontal-axis wind turbines. *Bulletin of JSME*, 27(229): 1460 – 1466, 1984.

[38] M.Iwasaki. The experimental and theoretical investigation of windmills. *Reports of Research Institute for Applied Mechanics*, 2(8): 181 – 229, dec. 1953.

[39] M.O.L.Hansen. *Aerodynamics of Wind Turbines*. James & James (Science Publishers), 2003.

[40] M.Sanuki. Studies on biplane windvanes ventilator-tubes and cup anemometers. *Papers in meteorology and geophysics*, 1(2): 279 – 290, dec. 1950.

[41] National Aerospace Laboratory (NLR). Evaluatie en verbetering van de prestaties van een kleinschalige diffusor augmented wind turbine (dawt);1e fase. 2008.

[42] National Aerospace Laboratory (NLR). Ontwerp van een kleinschalige diffusor augmented wind turbine (dawt); 2e fase. 2008.

[43] R.E.Wilson P.B.S.Lissaman. *Applied Aerodynamics of Wind Power Machines*. Prepared for NSF RANN under Grant N0.GI-41840, 1974.

[44] E.J. Glover P.G. Ryan. A New Approach Using Surface Vorticty Distribution Techniques and Lifting Line Theory. In *Transactions of the Royal Iinsitute of Naval Architects*, volume 114, 1972.

[45] D.G. Phillips. *An Investigation on Diffuser Augmented Wind Turbine Design*. Ph.D. Thesis, University of Auckland, 2003.

[46] I. Samuelsson. Low speed windtunnel investigation of propeller slipstream aerodynamic effects on different nacelle wing combinations. Technical report, 1990.

[47] T. Sant. *Improving BEM-Based Aerodynamic Models in Windturbine Design Codes*. Ph.D. Thesis, Delft University of Technology, 2008.

[48] L.P. Chua S.C.M. Yu, P.K. Koh. An experimental investigation of two stream mixing flow with a single delta tab. *International Journal of Heat and Fluid Flow*, 22: 62–71, 2001.

[49] A. Kogan A. Seginer. Final report on shroud design. (T. A. E. Rept. 32A), 1963.

[50] A. Kogan A. Seginer. Shrouded aerogenerator design study ii, axisymmetric shroud performance. (T. A. E. Rept. 32), 1963.

[51] P.D.C. ten Hoopen. A Literature Study and Experimental Investigation of a Diffuser Augmented Wind turbine ; In the preparation of the final Msc. thesis work. 21 feb., 2009.

[52] G.J.W. van Bussel. Development of a momentum theory for DAWT. *Mie University Japan*, 1998.

[53] G.J.W. van Bussel. Power Augmentation Principles for Windturbines. *The World Directory of Renewable Energy*, 1998.

[54] G.J.W. van Bussel. The science of making more torque from wind: diffuser experiments and theory revisited. *Journal of Physics:Conference Series*, 75, 2007.

[55] A.L.Loeffler Jr. D. Vanderbilt. Inviscid Flow Through Wide Angle Diffuser with Actuator Disk. *AIAA JOURNAL*, 16(10): 17 – 22, Oct. 1978.

[56] Vortec. `http://www.wind/-works.org/articles/vort/_closure/_end.html`.

[57] M.J. Werle. Shroud andEjector Agmenters for Subsonic Propulsion and Power Systems. *FLODESIGN INC*, 2008.

[58] M.J. Werle and W.M. Presz Jr. Ducted Wind/Water Turbines and Propellers Revisted. *FLODESIGN INC*, 2008.

Appendix A

Low speed 5 hole Pitot probe

This appendix contains a description of the mathematical scheme used to derive the various angles and velocities from the measured 5 hole pressure probe readings. The 5 hole pressure probe is calibrated according to Samuelsson's calibration scheme [46] used in the investigation of propeller slipstream nacelle/wing interactions. The 5 hole pressure probe used is depicted in figure 5.2b and is calibrated in the low speed wind tunnel at Delft University of Technology.

Through the use of a labview measurement application it was possible to obtain the pressure measurements from the 5 hole pressure probe. The pressure readings where referenced to the atmospheric pressure p_{ref} in the Open Jet Facility. From the 5 pressure readings it was possible, with the use of the calibration data, to derive the flow angles and velocities.

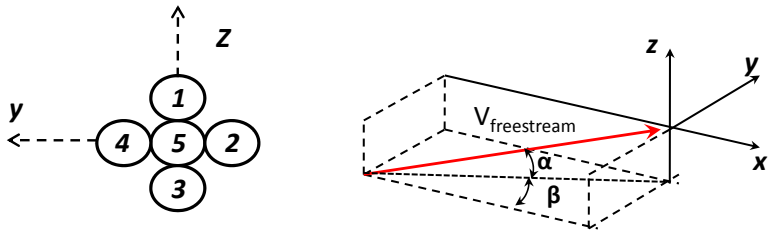

(a) Front view

(b) Velocity angle relative to pressure probe

Figure A.1: 5 hole pressure probe positioning

1. Calulate the minimum and average pressures:

$$p_{min} = min(\Delta p_1, \Delta p_2, \Delta p_3, \Delta p_4) \tag{A.1}$$

$$p_{average} = \frac{\Delta p_1 + \Delta p_2 + \Delta p_3 + \Delta p_4}{4} \tag{A.2}$$

2. Calculate various coefficients:

$$F_A = \frac{\Delta p_3 - \Delta p_1}{\Delta p_5 - p_{min}} \tag{A.3}$$

$$F_P = \frac{\Delta p_2 - \Delta p_4}{\Delta p_5 - p_{min}} \tag{A.4}$$

3. Perform a bi-linear interpolation with F_A and F_P in calibration graph A.2a to obtain α and β.

4. Perform a bi-linear interpolation with α and β in calibration graph A.2b and A.2c to obtain the values of F_Q and F_H.

5. Calculate the dynamic and total pressure present at the tip of the probe with equation A.5 and A.6 respectively.

$$q_{tip} = \frac{\Delta p_5 - p_{average}}{F_Q} \tag{A.5}$$

$$P_{tot_{tip}} = F_H(\Delta p_5 - p_{min}) + \Delta p_5 + p_{ref} \tag{A.6}$$

6. From the values calulated in equation A.5 the total velocity present at the tip of the probe can be calculated with equation A.7.

$$V = \sqrt{\frac{2}{\rho} q_{tip}} \tag{A.7}$$

7. The last step constists of converting the velocities in the proper reference plane.

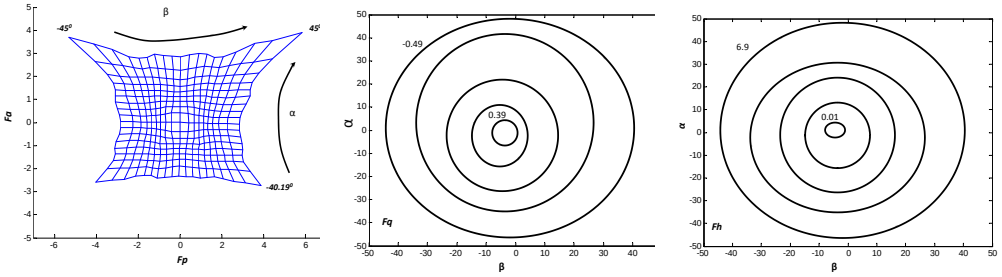

(a) (b) (c)

Figure A.2: 5 hole pressure probe calibration graphs

Appendix B

Wake influence matrix

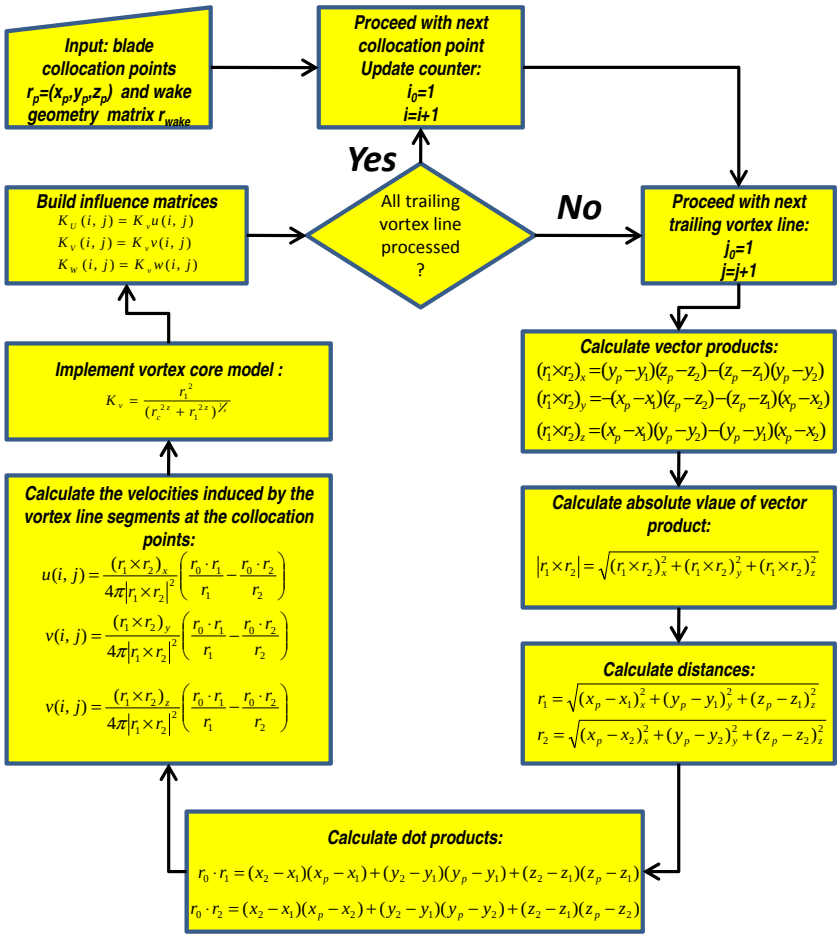

Figure B.1: Computational scheme for wake influence matrices using the sign convention as illustrated in figures 4.5a and 4.6b

Appendix C

Diffuser and blade geometry

Figure C.2 shows the geometry of the the diffuser with out the Gurney flap of 40 mm. The geometric diffuser and centerbody coordinates where derived from a IGES file as supplied by *NLR* and fitted with a spline interpolation scheme such that a continuous smooth surface was obtained. The splined diffuser geometry is used in the vorticity code and *X*foil[1]. Figure C.1 shows the blade properties as used in the mathematical model as designed by *NLR* [42]

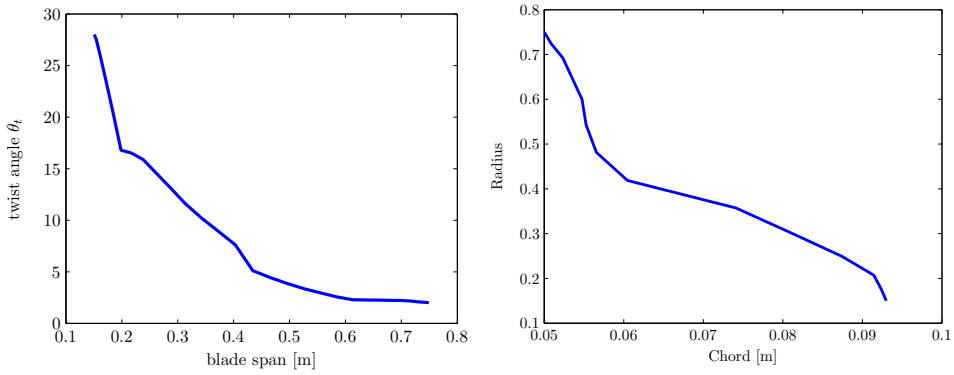

(a) Blade twist distribution

(b) Blade chord distribution

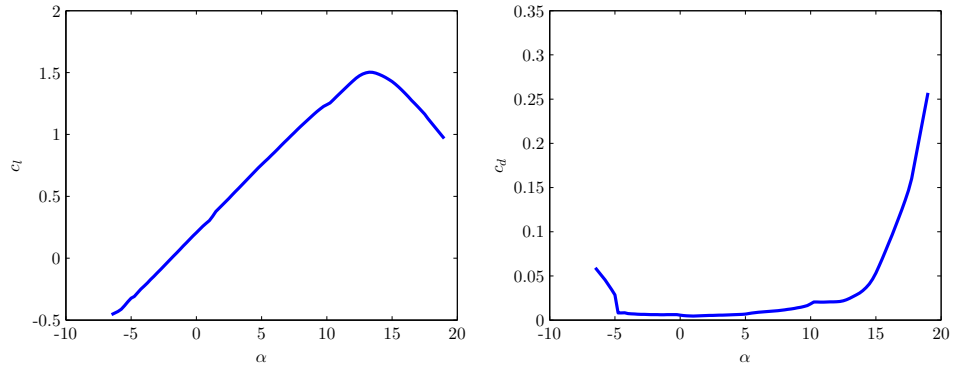

(c) $c_l - \alpha$ NACA 2207

(d) $c_d - \alpha$ NACA 2207

Figure C.1: Blade properties (NACA 2207 at Re=6e5)

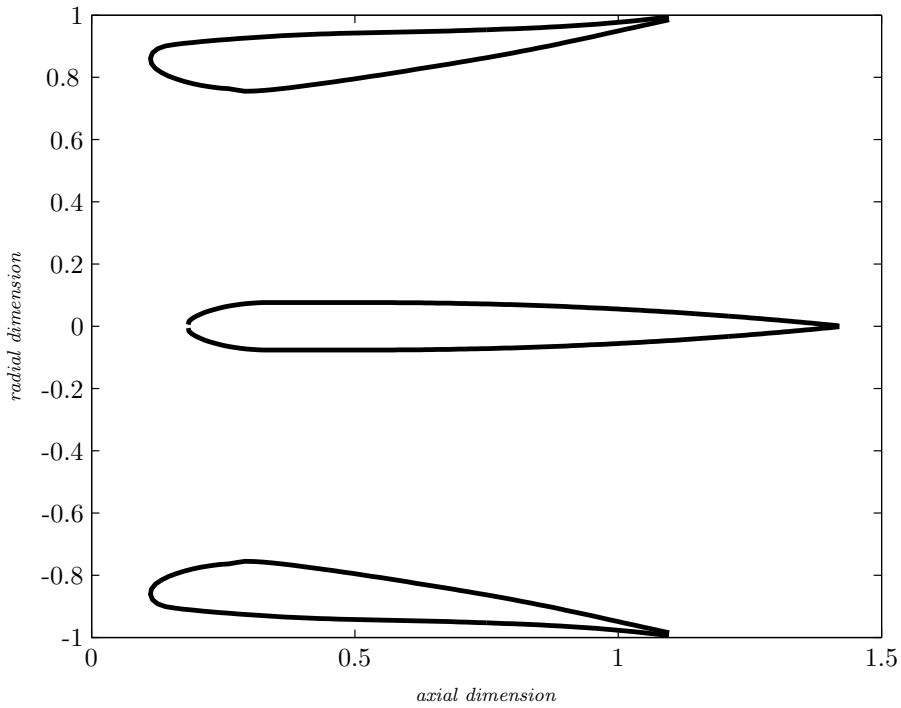

Figure C.2: Diffuser geometry

[1]In order to obtain smooth pressure distributions, the 'mdes' and 'filt' commands were used.

Appendix D

Measurement results

Figure D.1 shows the DAWT operational conditions corresponding to figure 6.8.

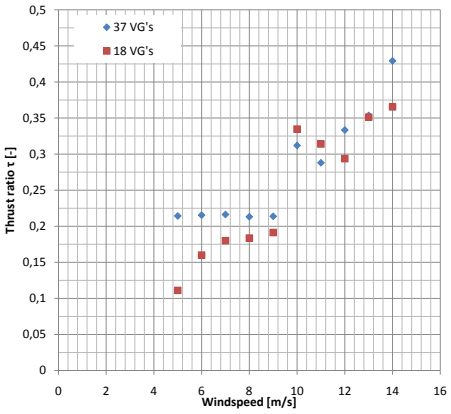

(a) Wind speed versus Thrust ratio τ

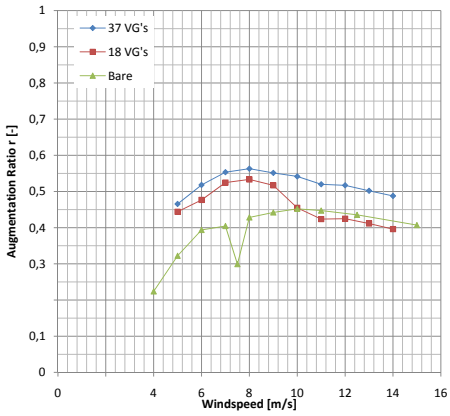

(b) Wind speed versus Augmentation ratio r

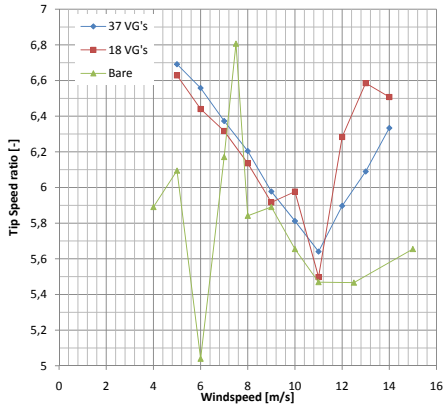

(c) Wind speed versus tipspeed ratio λ

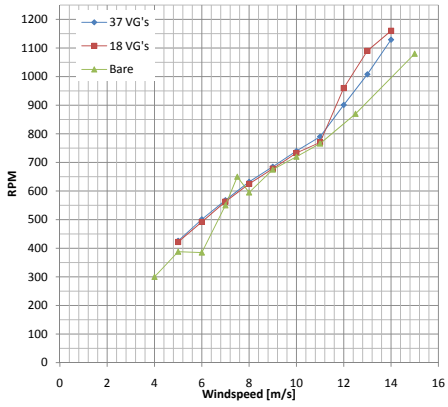

(d) Wind speed versus RPM

Figure D.1: Force measurements of thest phase 2 corresponding to figure 6.8; Rotor pitch angle: 17° ;

Figure D.2a to D.2f shows the flow angles, pressures and velocities 7 cm behind the rotor plane. The results of figure D.2 correspond to figure 6.9 and are obtained at a indicated windtunnel velocity of 10 m/s with and without an operating rotor. Furthermore, the Gurney flap has been removed during the measurements.

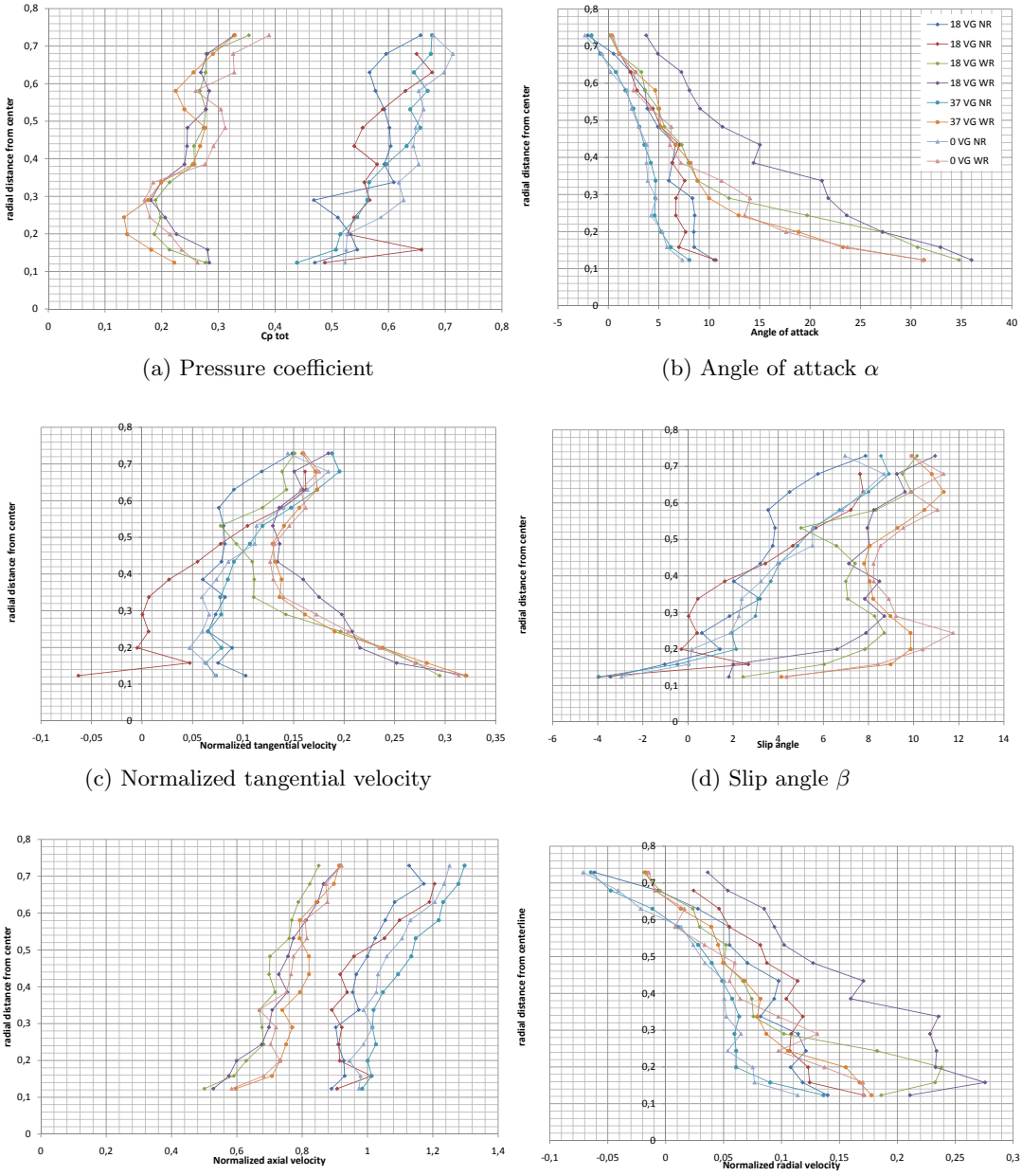

(a) Pressure coefficient

(b) Angle of attack α

(c) Normalized tangential velocity

(d) Slip angle β

(e) Normalized axial velocity

(f) Normalized radial velocity

Figure D.2: Measurement results of the pressure probe corresponding to figure 6.9 at 10 m/s 7 cm behind rotor plane (WR=With operating rotor at approximatly 720-750 RPM and 510-560 Watts see figure D.1b;NR=No rotor

Figure D.3a to D.3f shows the flow angles, pressures and velocities 10 cm behind the diffuser exit plane. The results of figure D.3 correspond to figure 6.10 and are obtained at various indicated windtunnel (see legend figure D.3b) velocities in the absence of a Gurney flap.

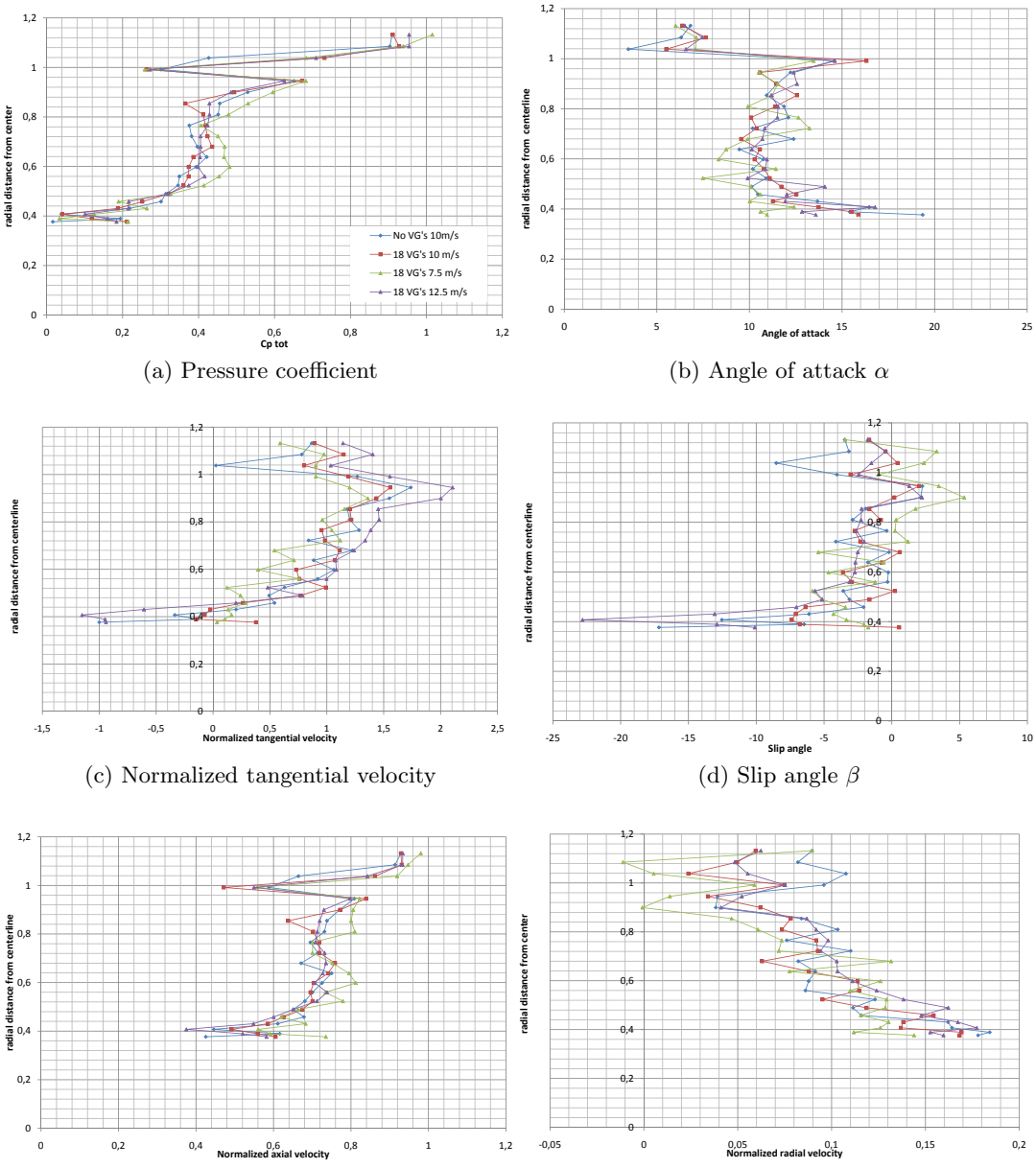

(a) Pressure coefficient

(b) Angle of attack α

(c) Normalized tangential velocity

(d) Slip angle β

(e) Normalized axial velocity

(f) Normalized radial velocity

Figure D.3: Measurement results of the pressure probe corresponding to figure 6.10 at 10 cm behind diffuser exit plane plane with operating rotor with corresponding operational conditions as shown in figure D.1

Figure D.4a to D.4d shows the flow angles, pressures and velocities 2 m infront of the wind tunnel exit plane and 1 meter infront of the DAWT leading edge. The results are obtained at an indicated windtunnel velocity of 12,5 m/s in the absence of a Gurney flap.

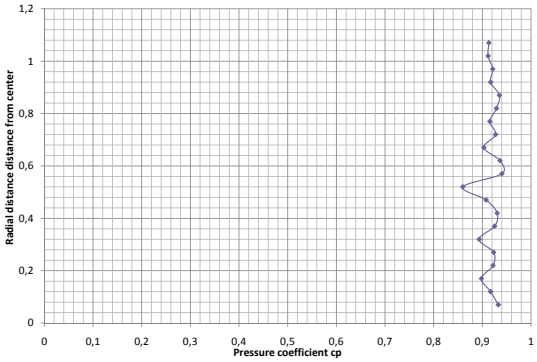

(a) Pressure coefficient

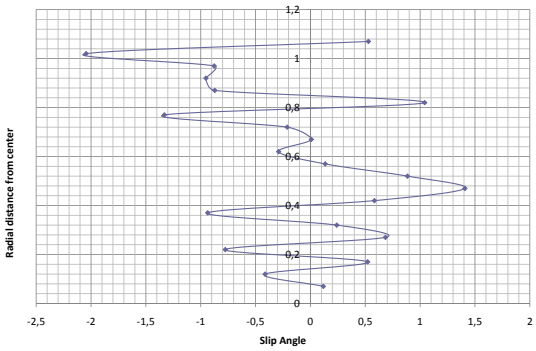

(b) Slip angle β

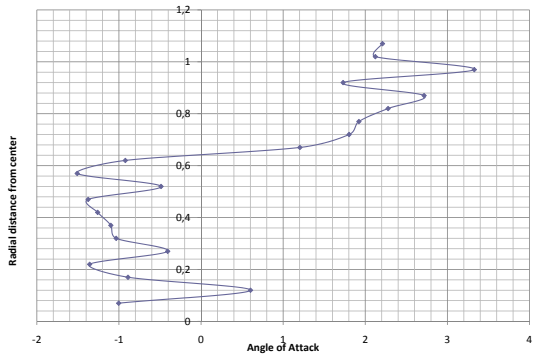

(c) Angle of attack α

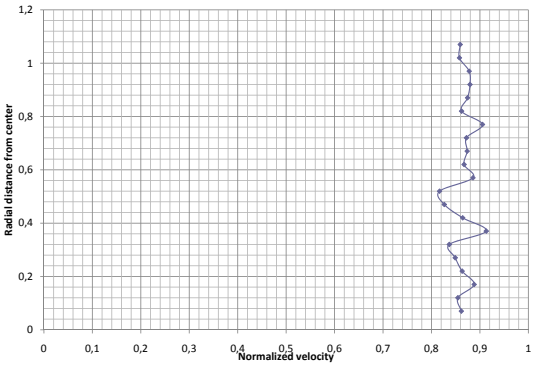

(d) Normalized tangential velocity

Figure D.4: Measurement results of the pressure probe performed 2 m infront of the wind tunnel exit plane at 12.5 m/s with operating rotor (Power= 950 Watts, RPM=870)